Title
Seismic anisotropy below Mexico and its implications for mantle dynamics

Author
Stubailo, Igor

Publication Date
2015

Peer reviewed|Thesis/dissertation

University of California
Los Angeles

Seismic anisotropy below Mexico and its implications for mantle dynamics

A dissertation submitted in partial satisfaction
of the requirements for the degree
Doctor of Philosophy in Geophysics and Space Physics

by

Igor Stubailo

2015

Abstract of the Dissertation

Seismic anisotropy below Mexico and its implications for mantle dynamics

by

Igor Stubailo

Doctor of Philosophy in Geophysics and Space Physics

University of California, Los Angeles, 2015

Professor Paul M. Davis, Chair

We use data from seismic networks with unprecedented dense coverage to study the Earths structure under Mexico.

First, we develop a three-dimensional (3-D) model of shear-wave velocity and anisotropy for the Mexico subduction zone using fundamental mode Rayleigh wave phase velocity dispersion measurements. The 3-D nature of our surface-wave-based results allows for better understanding of the interaction between the subducting slab, mantle lithosphere, and asthenosphere in the top 200 km. Our phase velocity maps reveal lateral variations at all periods consistent with the presence of flat and steep subduction. We also find that the data are consistent with two layers of anisotropy beneath Mexico: a crustal layer and a deeper layer that includes the lithosphere and asthenosphere, with the fast direction interpreted as aligned with the toroidal mantle flow around the slab edges. Our combined azimuthal anisotropy and velocity model enables us to analyze the transition from flat to steep subduction and to determine whether the transition involves a tear resulting in a gap between segments or is a continuous deformation caused by a lithospheric flexure. Our anisotropy results favor a tear, which is also consistent with the geometry of the volcanic belt.

Next, we conduct a shear wave splitting analysis that results in delay times of 1-2 s and

the fast direction that coincides with the absolute plate motion for the Mesoamerican Seismic Experiment (MASE) stations as well as stations east of the MASE array. The significant difference of the anisotropy in the upper 200 km, as detected by the surface wave analysis, and the average anisotropy between the CMB and the surface, as resolved by the shear wave splitting, implies that the shear wave splitting results are dominated by a structure deeper than 200 km. Since the time delays are significantly longer for the shear wave splitting results, the deeper structure is either much larger than 200 km, or has stronger anisotropy than the top 200 km, or a combination of both. At the same time, several relatively subtle features in the shear wave splitting results reveal potential influences of the shallow structure and its deeper extensions. This includes a small change in the fast direction around the southern edge of the Trans-Mexican Volcanic Belt (TMVB), which is located above the transition from the flat to steep subduction, as well as a different pattern of fast directions west of the MASE array, the region on top of two smaller subducting slabs.

Finally, we determine phase velocities of higher modes of Rayleigh waves, in order to constrain the depth of the anisotropy revealed by the shear wave splitting. Our analysis shows that the phase velocities for a number of overtones and periods are fastest in the direction predicted by shear wave splitting, suggesting that they are affected by the same deeper structure. Remarkably, the results for different directions are consistent with the presence of azimuthal anisotropy. Inspection of obtained phase velocities together with the sensitivity kernels tentatively indicates that a layer at the 200-400 km depth is a likely candidate for the source of the anisotropy. We find that such a layer can reproduce the observed shear wave splitting delays for reasonable values of anisotropy. The 200-400 km depth likely corresponds to the bottom of the asthenosphere, and it may be affected by the plate motion, explaining why the fast shear wave splitting direction is aligned with the plate motion. This tentative estimate of the anisotropy depth is consistent with findings in Northern Australia.

The dissertation of Igor Stubailo is approved.

Caroline Beghein

Jian Zhang

Lingsen Meng

Paul M. Davis, Committee Chair

University of California, Los Angeles

2015

To Nadia, Sashko, and Maksymko

(2015)

Table of Contents

List of Figures

List of Tables

Acknowledgments

First and foremost, my sincere gratitude goes to my research advisor and mentor, Paul Davis. Paul has introduced me to the exciting world of seismology and infinite fun of field trips. Without his keen insight, creative ideas, patient guidance, and contagious enthusiasm, this thesis would not have been possible.

I would like to thank Caroline Beghein, Jian Zhang, and Lingsen Meng for being on my thesis committee and providing me with valuable advice over the years. I am especially grateful to Caroline for our collaboration on the anisotropy and structure of the top 200 km under Mexico.

My thesis has also significantly benefitted from research collaborations with other creative and knowledgeable scientists. I thank Rob Clayton for his efforts on the the Middle American Subduction Experiment (MASE) and geophysical insights. I am also grateful to Allen Husker and Martin Lukac for our joint work on wireless network design and MASE data collection.

The unique MASE project that provided data for my research and my participation in it were enabled by the Center for Embedded Networked Sensing (CENS) at UCLA. My special thanks go to Deborah Estrin for making CENS into a major research enterprise focused on developing wireless sensing systems and applying them to critical scientific and societal pursuits, including the structure of the Earth.

My work would not be possible without an excellent group of researchers who made our network deployments in Mexico, Peru, and California a success. I have also been fortunate to join many of them for field trips as well as other fun explorations such as design of geophysical teaching tools. I thank Richard Guy, Victor Aguilar, Paul Cox, William Grear, Gary Glesener, and Steven Skinner for their dedication and hard work.

My geophysical knowledge and intuition have been significantly developed by several excellent courses. I would like to thank Jon Aurnou for his Physics of Earth course that

motivated us to build the Seismic Ring model. My thanks also go to David Jackson, for his Inversion Theory and Data Interpretation course, helping me become a better TA, as well as racquetball lessons. I am also grateful to Gill Peltzer, Fred Schwab, Per Jogi, and Yan Kagan for numerous scientific discussions.

I have been fortunate to have a chance to engage in a number of satellite activities that have expanded my view of seismology and its applications. I am grateful to Sharon Kedar for sharing with me his knowledge of planetary science and inviting me to collaborate on the seismic instrument testing for an upcoming Mars mission. I also thank Monica Koehler and Arnie Acosta for sharing their insight into earthquake engineering during a joint project on the UCLA Factor building.

My time at UCLA have been not only productive scientifically but also enjoyable on a personal level. I have been surrounded by wonderful human beings who are not only excellent scientists but also kind and fun-loving people. In addition to those already mentioned, I am grateful to many other comrades in arms for their friendship and support, including Antonio Dominguez, Joseph Ramsay, Deborah Weiser, Zagid Abatchev, Kaiqing Yuan, Zheng Xing, Anne Strader, Emily Foote, and Minoo Kosarian.

Finally, I would like to express my love and gratitude to my family. Since early childhood, my parents encouraged my curiosity and independence, two key qualities for a scientist. I am eternally grateful for their unconditional love and care over the years. I thank my sons Sashko and Maksymko for being the brightest colors in my life, always bringing joy and accomplishments that any parent would be proud of. My thanks also go to my parents-in-law for their love and support. I would like to give a special thank you to my wife Nadia for her true love and for being my best friend. I made all the right choices in life because I had the right person to help me make them. Thank you, Nadia, for being there with me.

Vita

1993	Diploma in Applied Math and Mechanics, Taras Shevchenko Kyiv State University
2000	M.A. in Computer Science, Boston University
2000–2002	Software Engineer, Carrier R&D Group, 3Com Corporation
2003–2008	Development Engineer, Center for Embedded Networked Sensing (CENS), University of California, Los Angeles (UCLA)
2014	M.S. in Geophysics and Space Physics, UCLA
2008–present	Graduate Student Researcher and Teaching Assistant, Earth, Planetary and Space Sciences, UCLA

CHAPTER 1

Introduction

The evolution, origin, and structure of the Mexican subduction zone have been studied using a variety of techniques over the years (e.g., Truchan and Larson, 1973; Pardo and Suarez, 1995; Manea et al., 2005; Kanjorski, 2003). Global plate reconstruction indicates that the Farallon plate fragmented about 23 Ma ago, at which point two new plates were created: the Cocos plate to the North and the Nazca plate to the South (Atwater and Stock, 1998; Londsdale, 1991; Mann, 2007). About 13 Ma later, the Rivera plate came into existence by separating from the Cocos plate.

Based on seismicity, focal mechanisms, and the slab geometry determined from the hypocenter locations of local events, the area under Mexico can be split into several sections (Fig. 1.1; Pardo and Suarez, 1995): (1) the Jalisco section, where the Rivera plate subducts steeply at approximately 50°, (2) the Michoacan section, where the dip of the Cocos plate undergoes a transition from steep to almost parallel to the surface, (3) the Guerrero-Oaxaca section, where the slab is flat for about $\sim$ 250 km, and (4) the southern Oaxaca and Chiapas section, where the dip of the Cocos plate increases up to 30°. As a result of the complex subduction, the Trans-Mexican Volcanic Belt (TMVB), which consists of nearly 8000 volcanoes, became apparently oblique to the Trench instead of being parallel to it (Fig. 1.1). These relatively shallow features can be imaged by surface waves.

Detailed information on the slab depth under the transect from Acapulco to Tampico has been obtained from the teleseismic data collected during the Middle America Subduction Experiment (MASE) (Chapter 2; Perez-Campos et al., 2008; Husker, 2008; Iglesias et al.,

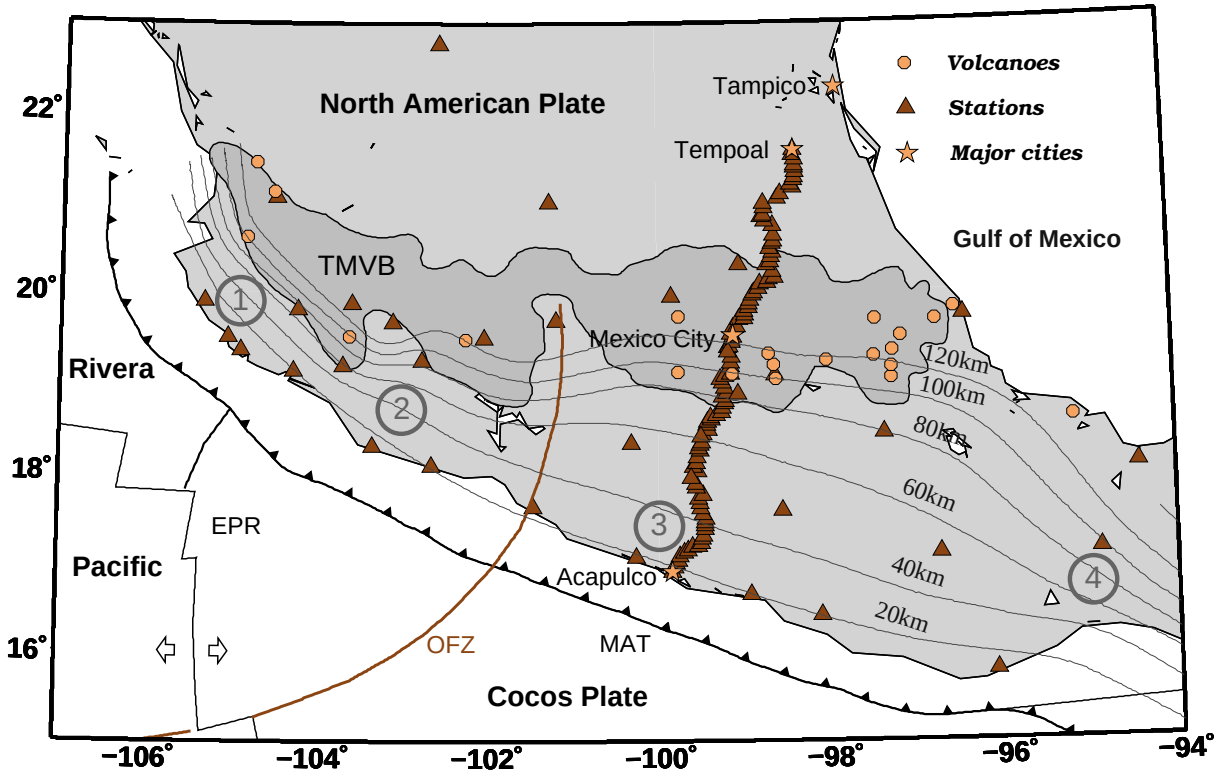

Figure 1.1: Tectonic setting of the region. The area imaged in this study is centered under the MASE array, which stretches from Acapulco to Tempoal. The MASE stations and other stations that fall within the map area are shown as triangles. The Middle America Trench (MAT), East Pacific Rise (EPR), Orozco Fracture Zone (OFZ) are also displayed. The circles represent the volcanoes that are part of the Trans-Mexican Volcanic Belt (TMVB). The isodepth lines of the Wadati-Benioff zone obtained from the local seismicity (Pardo and Suarez, 1995) indicate that the slab is steeper in the North-West than in the South-East, and that the slab under the southern half of the MASE array is relatively flat. The circled numbers indicate the four sections of the slab geometry from (Pardo and Suarez, 1995): (1) Jalisco, (2) Michoacan, (3) Guerrero-Oaxaca, (4) Oaxaca.

2010; Stubailo et al., 2012; Dougherty and Clayton, 2014). The results based on receiver function analysis (Perez-Campos et al., 2008) and body wave tomography (Husker, 2008; Husker and Davis, 2009) show an approximately 40-km thick, flat, shallow slab, which starts dipping $\sim$ 250 km inland from the trench at approximately 74°, and which is truncated at $\sim$ 520-km depth. The flat subduction under the MASE array is consistent with the prior study by Pardo and Suarez, 1995. A two-dimensional (2-D) slab image based on S-wave velocities was also obtained by Iglesias et al., 2010 using regional earthquakes. The authors described a well-resolved low-velocity zone below the TMVB consistent with the presence of a mantle wedge. Chen and Clayton, 2009 showed low attenuation associated with the subducting part of the slab (forearc) and high attenuation near the mantle wedge and beneath the TMVB. The authors interpreted the high-attenuation zone in the mantle wedge as related to relatively high temperature, fluids, and partial melts produced during the subduction process. The current 2-D view of the slab under the Central Mexico region (MASE line) based on the prior studies (Kim et al., 2006; Husker, 2008) is shown in Fig. 1.2.

In this study, we use the unique MASE data, together with data from other networks, to develop a 3-D model of S-wave velocity and azimuthal anisotropy of the Mexican subduction zone (Chapters 3 and 4), and compare the amplitude and direction of the determined anisotropy with the one calculated based on the shear-wave splitting measurements (Chapter 5) and Rayleigh wave higher modes (Chapter 6). The 3-D nature of our surface wave results allows for better understanding of the interaction between the subducting slab, mantle lithosphere, and asthenosphere in the top $\sim$ 200 km. Shear wave splitting reflects the anisotropy over a much greater depth range, since it is a phenomenon that occurs when a polarized SV (for SKS) shear wave enters an anisotropic media traveling from the core-mantle boundary (CMB). The incident shear wave splits into two polarized shear waves arriving at different times and providing integral information about the underlying anisotropy.

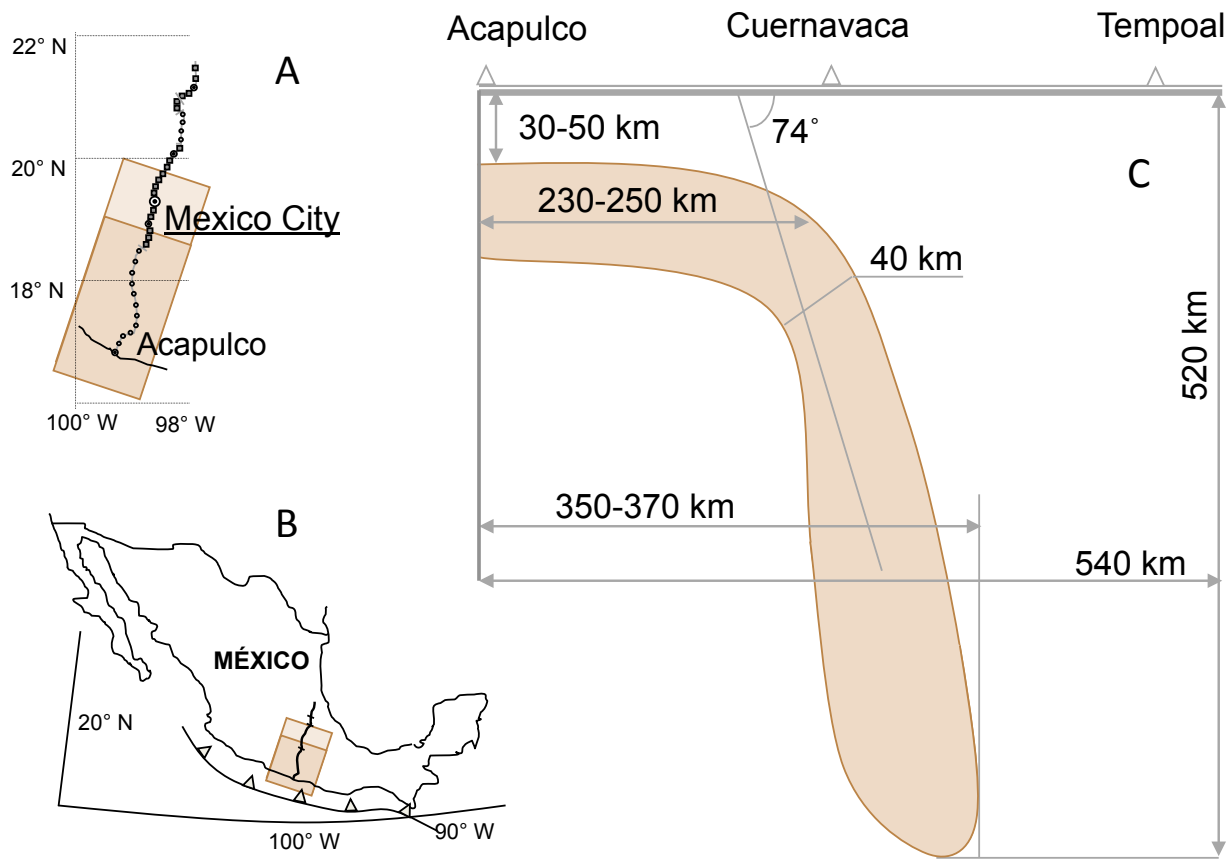

Figure 1.2: 2-D view of the slab under the MASE array based on P-wave tomography (Husker, 2008) and receiver function analysis (Perez-Campos et al., 2008). (A) Map view of the area showing the slab and the MASE array above it. Note the dense positioning of stations. (B) The location of the study area with respect to the trench. The study area lies within section 3 of Pardo and Suarez, 1995. (C) The side view of the slab. The subducting slab is nearly flat for $\sim$ 230-250 km, and then bends relatively abruptly below the middle of the MASE array, with the subducting angle of $\sim$ 74°. The slab truncates at $\sim$ 520 km depth.

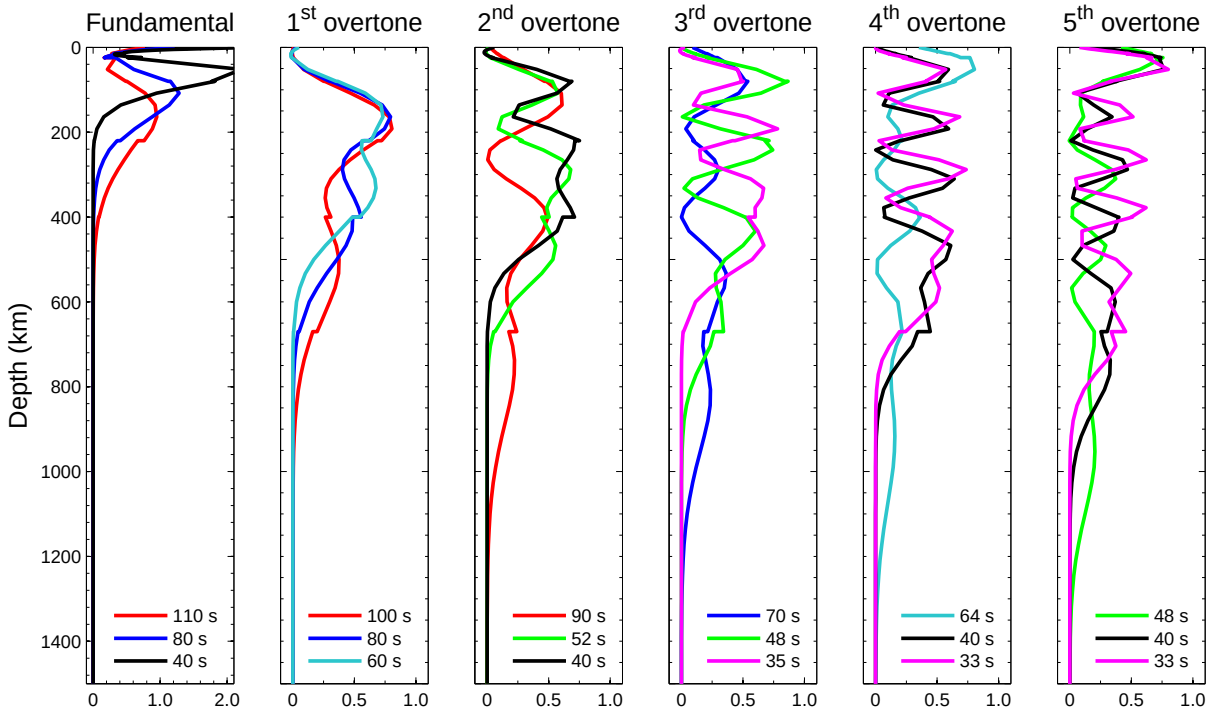

Figure 1.3: Normalized sensitivity kernels at different periods for fundamental and higher spherical modes.

Shear-wave splitting is effective for studying upper mantle anisotropy beneath receivers and has a better lateral resolution than Rayleigh wave phase velocity dispersion measurements, although it suffers from a poor depth resolution. In order to improve the depth resolution, we can use Earth's free oscillations. The free oscillations of the Earth result from the constructive interference of waves traveling in opposite directions. Two independent families of modes exist for an elastic non rotating spherically symmetric Earth model: the spheroidal modes, resulting from the P and SV waves, and the toroidal modes that include SH waves. Here, we use spheroidal modes to constrain the depth of anisotropy. At a given period, overtones sample the deep structure that is poorly sampled by the fundamental mode in retrievable frequency ranges (Fig. 1.3). The inclusion of the overtones should improve the depth resolution.

CHAPTER 2

Development of wireless seismic networks and data collection

This chapter is partially based on the following publications:
Lukac, M., Naik, V., Stubailo, I., Husker, A., and Estrin, D., In vivo characterization of a wide area 802.11b wireless seismic array. Mobicom, 2007.
Husker, A., Stubailo, I., Lukac, M., Naik, V., Guy, R., Davis, P., and Estrin, D., Wilson: The Wirelessly Linked Seismological Network and its application in the Middle American Subduction Experiment. SRL, 2008.

2.1 Introduction

Campaign data of excellent quality and spatio-temporal coverage is essential for expanding our knowledge about Earth's structure and dynamics. We have been actively involved in the development of instrumentation and protocols for novel temporary wireless seismic networks as well as in the site selection, installation, and data gathering from such networks in Mexico and Peru. The data from Mexico is used in the rest of this thesis for studying the structure of the Mexican subduction zone and its surroundings. The data from Peru will enable similar future investigations.

Prior to the deployment in Mexico, the only wireless network for seismic applications was used to monitor volcano activity (Werner-Allen et al., 2006). However, their network

consisted of small number (16) of nodes used within an area a small size (3 km) over a short period of time (19 days) with intermittent data transfer of only in-network detected events. Their network design would not be able to process the continuous data transfer or deal with the size (tens of kilometers) and time frame (years) required by the projects in Mexico and Peru.

Until recently, the golden standard in temporary seismic deployments has been installing stand-alone sites, which record seismic data onto local disks. Such sites need regular (monthly to yearly) visits for data gathering and health monitoring. The advantages of the stand-alone sites are their independence from local infrastructure and relative ease of installation. The disadvantages are the need for the regular visits as well as the intermittent nature of data recovery (only during visits) that prevents near-real-time analyses. Furthermore, the state of the site is not known between visits, potentially leading to large data losses.

With the rapid development in wireless communication and the ability to transport large quantities of data over Internet, temporary wireless networks have become a possibility. Such networks promise near-real-time data delivery and prompt identification of site problems. However, they require additional instrumentation for wireless and Internet communication, modification of standard protocols for potentially unreliable connections, and careful network topology design and site selection that allow for network connectivity. Our contributions to these areas are briefly described in this Chapter.

2.2 Instruments

Stand-alone stations commonly used in temporary installations include a sensor (seismometer), digitizer (an analog to digital data converter), and data logger. Sites in a wireless network need to communicate and transfer data among themselves. For this purpose, the data logger is replaced with a microcomputer and an antenna.

We have designed and built such a customized microcomputer as part of a Center for Embedded Networked Sensing (CENS) project and dubbed it CENS Data Communications Controller (CDCC) (Figures 2.1 and 2.2). It was decided to design the CDCC ourselves using standard readily available components and software (rather then purchase proprietary ones) for several reasons. First, standard software allows for full access to the operation system, which in turn allows to easily test various communication algorithms and other software solutions. Second, commonly available components allow for easy on-site repairs and do not require the unit to be shipped back to the company. Third, one can achieve full customization and greater involvement of students and researchers.

After extensive testing, the final configuration consists of a low-power 1-watt Intel XScale core microcomputer running Linux with a long-range radio and a flash disk enclosed in a water-tight fiberglass box. The microcomputer allows for a small and lightweight system and easy deployment. The long-range SMC2532W-B 200 mW 802.11b radio enables the CDCC to use standard Internet protocols. A one 4GB-16 GB flash disk provides data storage and hence the ability to temporarily turn a station into a stand-along one if the wireless communication fails. The stock antenna of the wireless card is removed and replaced by more powerful external antennas, either 15 dBi yagi or 24 dBi parabolic. More details are given in Husker et al., 2008.

2.3 Wireless data delivery

Internet is generally not available at the desired locations of the network nodes, which can be rather remote. Hence the nodes need to transmit the data wirelessly to the Internet locations, and robust network design and protocols are needed for data delivery from such networks.

Data transfer proceeds as follows. Each site sends it data through other sites to a base

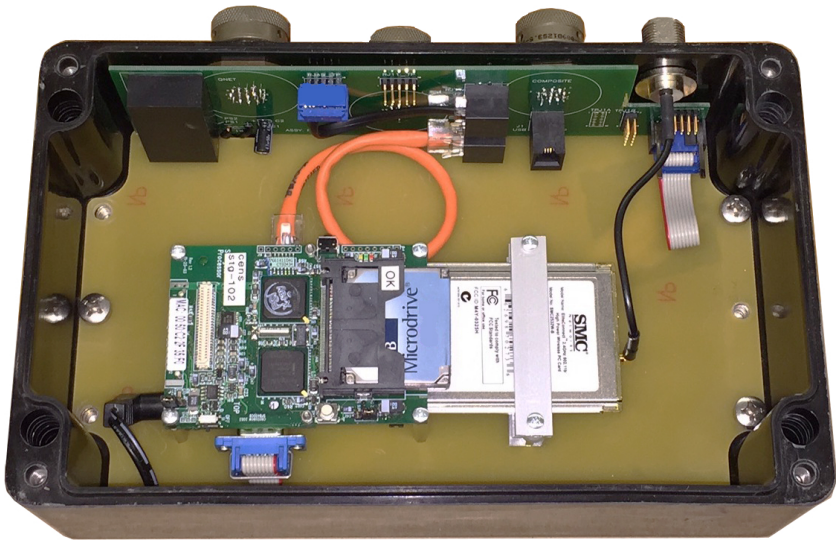

Figure 2.1: The developed wireless data collection and processing instrument, CENS Data Communications Controller (CDCC), essentially a field computer. The waterproof and low-power unit uses generic over-the-shelf components for easy repairs, runs Linux, and can be powered from a car battery and/or solar panel.

station which has a desktop computer connected to the Internet (Fig. 2.3). The base station also provides fault-tolerant data storage and processing power. Base stations transmit data to a large storage array at UCLA via Internet. This can be done either continuously or episodically (e.g., at night when the connection is fastest), utilizing the local storage as needed. If the scientifically desired sites are too far from the Internet-enabled base station, relay stations are needed to deliver the data. The goal was to transfer 24-bit, 100-sample/s data across at least a 15-node network for each base station.

In the light of such a setup, it is crucially important to have an appropriate network topology design tested in the field. Each site needs to have wireless connection to at least one, and preferably more, other sites to transmit its data. Hence antennas at the corresponding sites literally need to see each other (i.e., have an unobstructed line-of-site). This means that

Figure 2.2: The set of instruments for one node of a wireless network: a seismic sensor, CDCC, digitizer (Kinemetrics Q330), and car battery.

the site does not necessarily communicates with the closest site, which may be behind trees or a hill, but rather the closest "visible" site. The surface topography plays a key role, as shown in the schematic but representative example of Fig. 2.4a where the network is located over three hills. Some sites may not see each other but they can see a site at the top of a hill (Fig. 2.4b).

The need for wireless connectivity increases the demands on the site selection in the field. While sites for stand-alone nodes can be chosen by one person/group, the site selection for wireless nodes requires at least two people/groups, to test connections between various candidate sites. The 802.11b radios use 2.4 GHz and provide high throughput but they

also require line-of-sight for the distances of interest (5 km or more). This is because the small wavelengths involved can be attenuated by something as small as tree leaves. Indeed, trees are the main problem for the wireless communication in rural areas, while manmade structures are the main obstacles in the urban areas. In addition, the sites still need to be able to collect high-quality seismic data without much noise, and hence they need to be positioned away from major roads.

Continuous long-term data transfer over large distances in networks with potentially long links and varying link quality because of weather and other factors requires novel data transfer protocols. We have contributed to the design and testing of such a protocol, Disruption Tolerant Shell (DTS), which has been programmed by CENS computer scientists at UCLA (Lukac et al., 2006; Lukac et al., 2007; Husker et al., 2008). In the Disruption Tolerant Shell (DTS), all sites are "aware" of all other sites within the field of view: commands are propagated through the entire system, and links can be temporarily up or down. The protocol allows for more efficient data movement, utilizing dynamic routing, smaller packet size, and aggressive data copying (with periodic evaluation and re-transfer of the lost data). The protocol generates comprehensive logs of all transfers, and all commands report the outcome back to the initiating station.

2.4 Deployments to Mexico (2005-2007) and Peru (2008-2011)

The first large-scale and relatively long-term wireless network for seismic applications was deployed with our active participation as part of the Middle American Subduction Experiment (MASE). It was dubbed the Wirelessly Linked Seismological Network (WiLSoN). WiLSoN functioned for more than a year and a half collecting about 2.5 GB of data daily. MASE was done in collaboration between UCLA and California Institute of Technology. The next large-scale wireless seismic network deployoment was a part of the Andean Seismic Project in Peru, another joint effort between UCLA and California Institute of Technology.

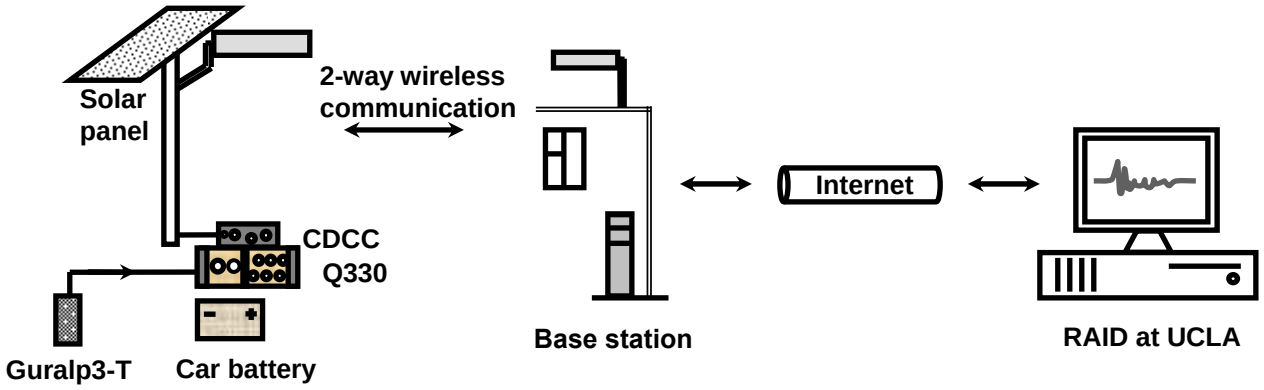

Figure 2.3: Schematics of the data propagation within our wireless network. The data is transferred between nodes and eventually selected nodes transfer the data to base stations, which are Internet connected sites (at universities, internet cafes etc). The base stations use Internet to transfer data to UCLA.

The overall network was arranged into a quadrilateral. One of the sides was a wireless array (line 1, Fig. 2.6) of 49 stations with spacing of 6 km on average, running through eight plains and seven mountain ranges (Lukac et al., 2010). The wireless connectivity of the stations was aided by the presence of a 6-km volcano peak that allowed us to have prominent antenna placements at the height of about 5 km. Such antenna locations enabled dedicated long-haul links (30-50 km) between several hubs.

Here we concentrate on the MASE deployment. The total MASE seismic array consisted of 100 seismometers installed over about 500 km in Mexico in a nearly perpendicular line from the Middle American trench (Fig. 2.5). 50 of the stations were stand-alone and 50 incorporated WiLSoN. Not all of the fifty stations were wirelessly connected to the base stations; ten of them were either directly connected to the Internet or connected wirelessly to a stand-alone site where data was stored and periodically collected. Some wireless links were as long as 40 km. Time synchronization of the nodes was provided by GPS.

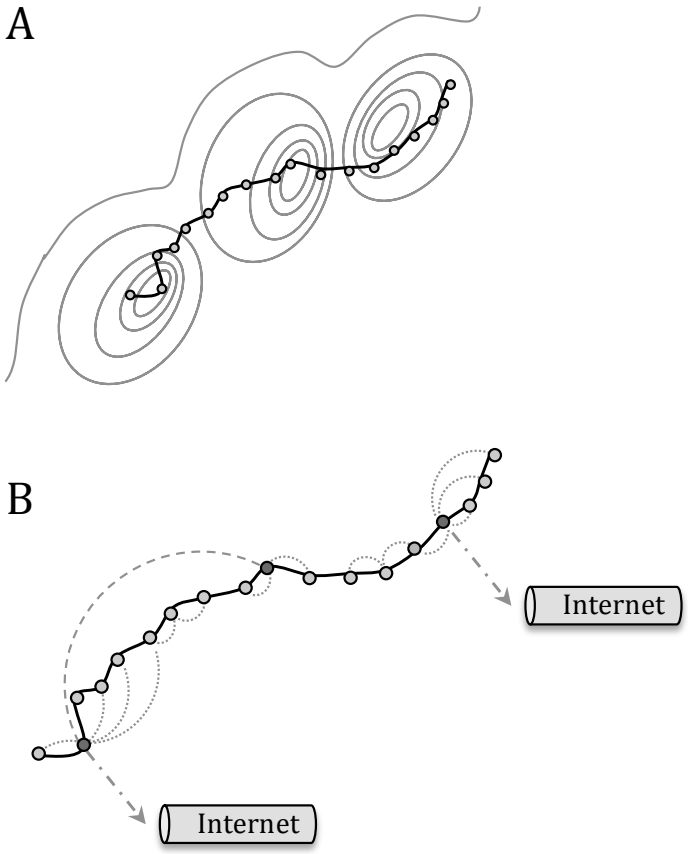

Figure 2.4: Schematic example of the relation between (a) the surface topography (contour lines) and (b) active data-delivery links in the network (dashed lines). The nodes located on the hilltops are responsible for longer connections. Only a few sites are connected to the Internet delivering data to UCLA.

To our knowledge, this wireless network deployment was unique in terms of its spatial scale, duration, and diversity of the environment. The network of 40 wirelessly connected stations performed well. Data from wireless nodes was delivered 78% of the time, compared to 86% of the time for the stand-alone sites. This is quite good given that the network protocols were being developed and adjusted while the network was functioning. Indeed, the performance was improving throughout the experiment.

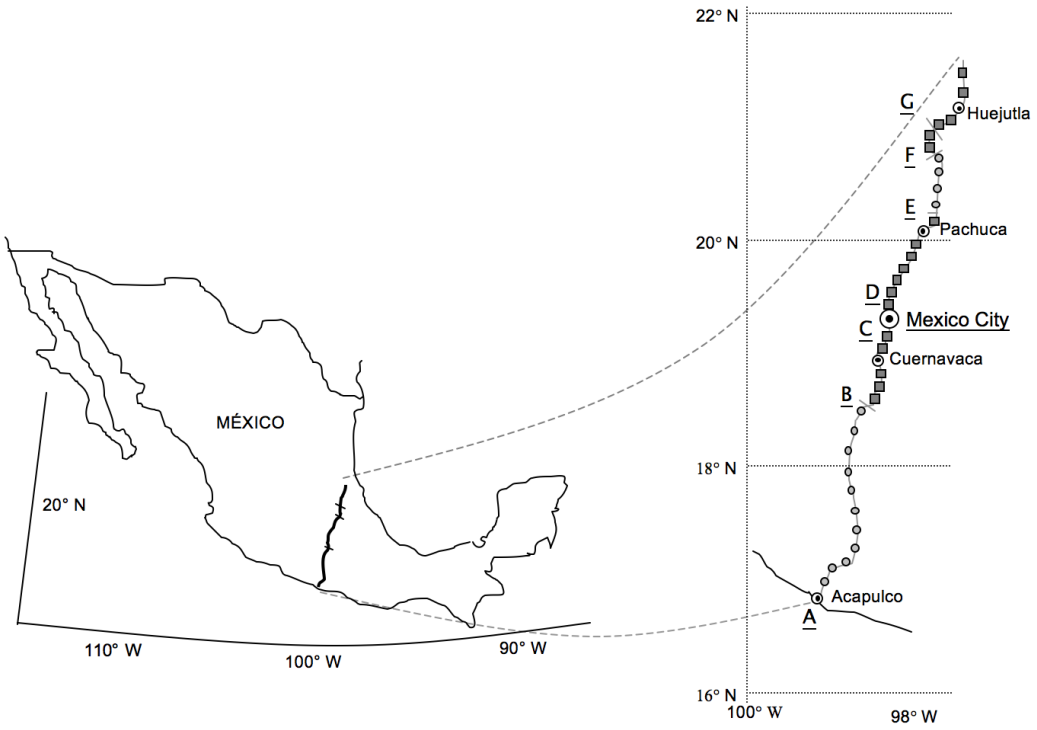

Figure 2.5: The Wirelessly Linked Seismological Network (WiLSoN) in Mexico, part of the Middle American Subduction Experiment (MASE). The wireless stations are represented by squares; dots indicate standard standalone stations.

The node uptime was much better in WiLSoN than in the previous application involving volcanoes (Werner-Allen et al., 2006; Lukac et al., 2007). This is likely due to our design of the controller (CDCC). First, we chose to run well-established computer system, Linux, which provided stability and accessibility to the node, enabling us to connect, diagnose, and correct problems remotely. Second, the hardware design stood up well to the elements. The analysis of reasons for node downtime (Lukac et al., 2007) showed that 62% of downtime was caused by software problems, 23% by connectivity issues, 10% by hardware malfunction, and 5% by unknown issues. This bodes well for future improvements, since software problems and connectivity issues can be fixed with further development.

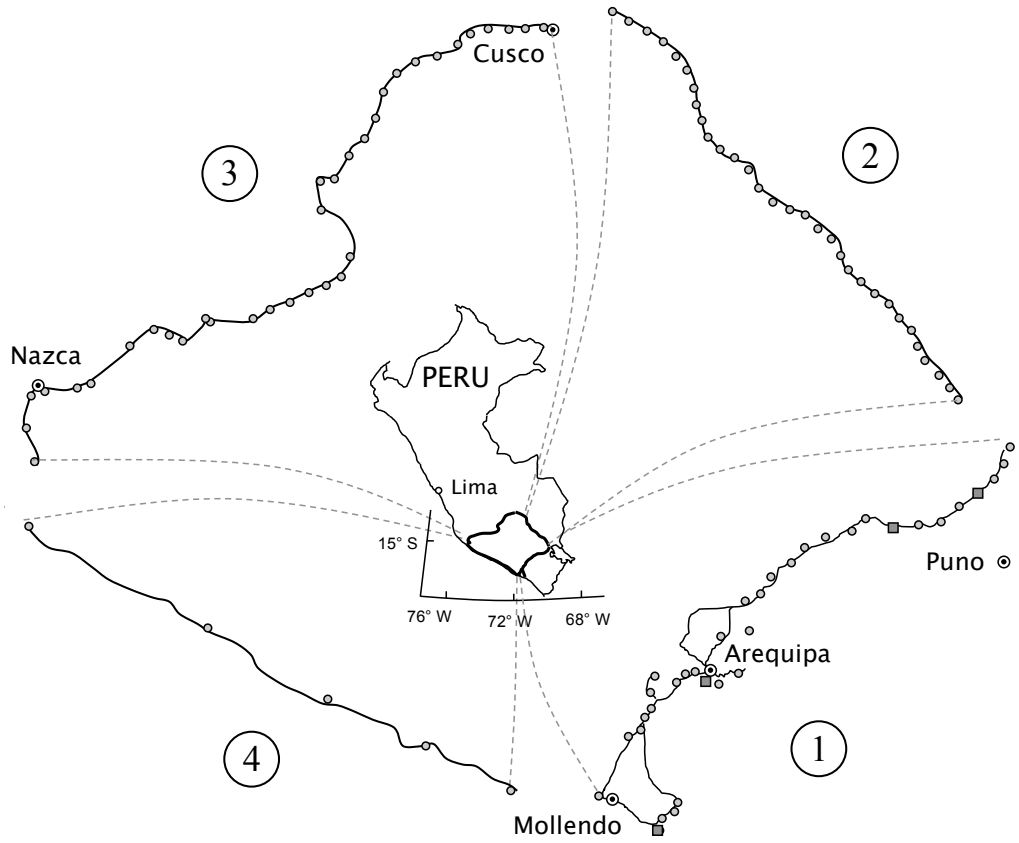

Figure 2.6: Map of the Peru site installation. The four lines installed at different times marked by encircled numbers.

CHAPTER 3

Azimuthally Anisotropic Phase Velocity Maps Of Fundamental Mode Rayleigh Waves

This chapter is partially based on the following publication:
Stubailo, I., Beghein, C., and Davis, P. M., Structure and anisotropy of the Mexico subduction zone based on Rayleigh-wave analysis and implications for the geometry of the Trans-Mexican Volcanic Belt. JGR, 2012.

3.1 Introduction

Seismic anisotropy is important to study since it can provide insights into the deformation history of a region. It may arise from the lattice preferred orientation (LPO) of intrinsically anisotropic crystals or from the shape preferred orientation of isotropic materials with contrasting elastic properties (Karato, 1998). Anisotropy in the crust may be caused by mineral fabrics, preferentially oriented fluid-filled cracks, and the presence of faults (Crampin et al., 1984). In the upper mantle, it is often attributed to the LPO of olivine over large scales as a result of the shear direction and shear plane or the orientation of stress, and therefore can give information on the past and current deformation processes in the lithosphere and asthenosphere, respectively (Karato, 1998; Silver, 1996; Karato, 1987).

To obtain a 3-D model of the Mexican subduction zone, we perform dispersion measurements of Rayleigh waves for periods of $16 - 171$ s and show that Rayleigh phase velocities

depend on the azimuth of propagation. The dense network of seismic stations used here and the analysis based on surface waves, which inherently have better depth sensitivity to structure than body waves, allow us to obtain a higher-resolution velocity and anisotropy model than in previous studies. The combined 3-D models of S-wave velocities and anisotropy enable us to infer information about the dynamics of the subduction process in the region.

3.2 Data

We use data collected by several networks on a total of 181 stations (Fig. 3.1): the Mesoamerican Seismic Experiment (MASE, 100 stations), the Network of Autonomously Recording Seismographs (NARS, 15 stations), USArray (24 stations), Mapping the Rivera Subduction Zone (MARS, 9 stations), and the Mexican Servicio Sismologico Nacional (SSN, 33 stations). All the Z-component waveforms used are down-sampled to 1 sample per second and corrected for the instrument response to eliminate phase distortion at higher frequencies.

Our data selection is tailored to the two-station method (Sato, 1955; Brune and Dorman, 1963; Knopoff et al., 1967; Herrmann, 1987), which allows us to measure phase velocities between two stations that share a common great-circle path with an event. This method has the advantage over single-station phase velocity measuring techniques of removing uncertainties related to the source and to the path between the source and its near station. The codes employed here are based on the method developed by Herrmann, 1987 and implemented by J. A. Snoke (Warren et al., 2008). We identify combinations of station pairs and events for which the angles between the great circles are no larger than 3° (Fig.3.2) to make sure that the stations are aligned near the common great circle path. To have suitable signal-to-noise ratio (SNR), we further restrict ourselves to events with moment magnitude 6.0 and larger in the USGS catalog and depths shallower than 250 km.

We perform a frequency-time analysis (FTAN) (Landisman et al., 1969; Dziewonski et al.,

1969) for each earthquake and station. We use the FTAN plots to narrow down both a range of group velocities and periods suitable for further processing in order to isolate the fundamental mode surface waves. A time window was then determined for each period range based on the group velocity range and epicentral distance.

Events and stations with low signal-to-noise ratio or irregular FTAN plots (Fig. 3.3) are rejected. We also reject pairs of stations for which the phase velocities differ for earthquakes arriving from opposite sides. For instance, if the phase velocity determined for station pair STA1-STA2 does not fall within the uncertainties estimated for the phase velocity of station pair STA2-STA1, the measurements for that station pair are rejected. Such phase velocity discrepancies can be caused by paths that cross tectonic boundaries at sharp angles leading to refraction, multipathing, and scattering. Of all the station pairs that were associated with events coming from opposite directions, only a small number (20 %) were rejected and the majority of these rejected pairs were originated from Peru, Chile, and Western Canada, i.e., from GCPs parallel to the coastline. Tanimoto and Prindle, 2007 showed that for waves propagating along such paths, off-great-circle path propagation can affect estimates of azimuthal anisotropy from Rayleigh waves by up to 30°. However, for paths that are roughly perpendicular to the coastline, they showed that off-great-circle path effects were negligible. Because of this, and since most of our events have GCPs perpendicular to the coastline (see Fig.3.2), we do not think the inversion results would be affected significantly.

3.3 Interstation phase velocity measurements

Based on the criteria described in Section 3.2, we are able to identify 7602 station pairs corresponding to 116 teleseismic events recorded between 2005 and 2009. If a pair of stations is linked to multiple events, we average the dispersion curve measurements. After averaging the dispersion curves, we are left with 5050 interstation phase velocity curves (with up to 12 events per path) for the periods of $16, 18, 20, 22, 25, 28, 33, 38, 44, 54, 68, 85, 102, 128$, and

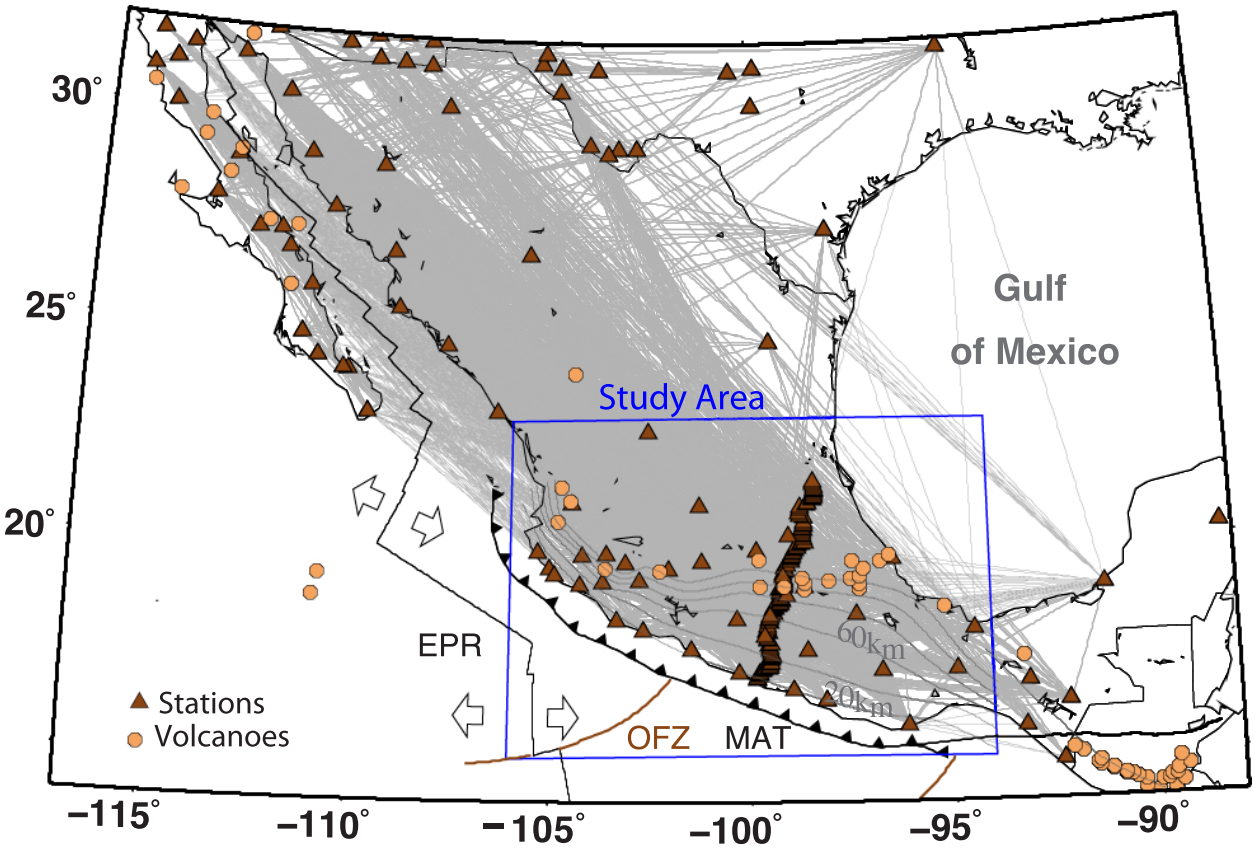

Figure 3.1: Seismic stations used in the study (triangles). The ray coverage is shown by grey lines. The area of best coverage is outlined by a blue rectangle. The circles indicate volcanoes.

171 seconds. The path density for the selected events is higher to the west of the study area (Fig. 3.1), but overall the selected paths result in excellent coverage as shown by the resolution tests described in Section 3.4.

The interstation method employed uses a reference phase velocity spectrum calculated for a local reference Earth model to remove the need for phase unwrapping. Our local reference Earth model (hereafter referred to as mTNA) is a composite model, modified from the upper mantle shear-wave velocity Tectonic North America (TNA) model (Grand and Helmberger, 1984) by adding the P-wave velocities and densities from model AK135 (Kennett et al.,

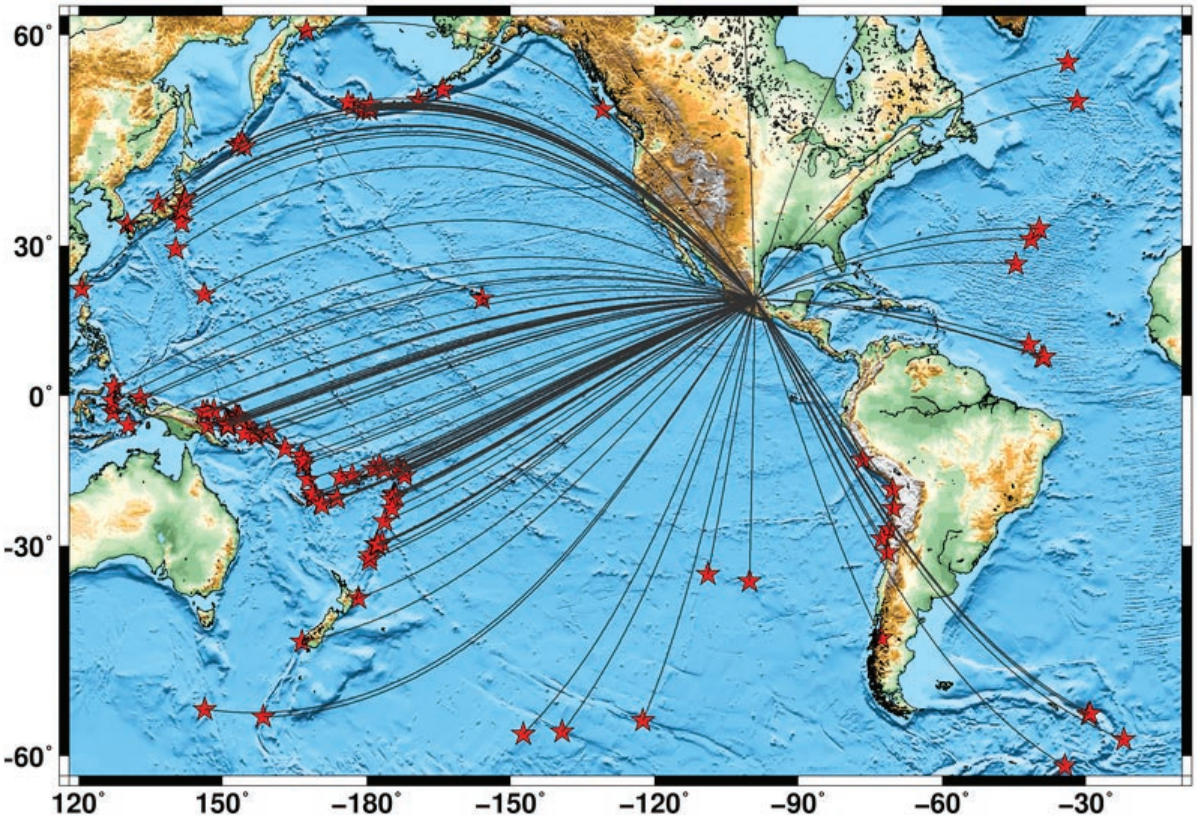

Figure 3.2: Representative events (red stars) used for the study and the corresponding great circle paths (grey lines) connecting them to a MASE array station. The chosen earthquakes are shallower than 250 km and of magnitude M $\geq$ 6.0 to have suitable signal- to-noise ratios. The events occurred between 2005/01/14 and 2009/11/13.

1995), and the Crust 2.0 crustal model (Bassin et al., 2000). This reference model is shown in Fig. 3.4 and described in Table 3.1. Phase velocity uncertainties are determined based on the coherence of the two waveforms after the near-station waveform has been time-shifted to the far-station epicentral distance using the calculated phase velocities (see details in Warren et al., 2008.

Examples of interstation measurements made along the MASE array at three different

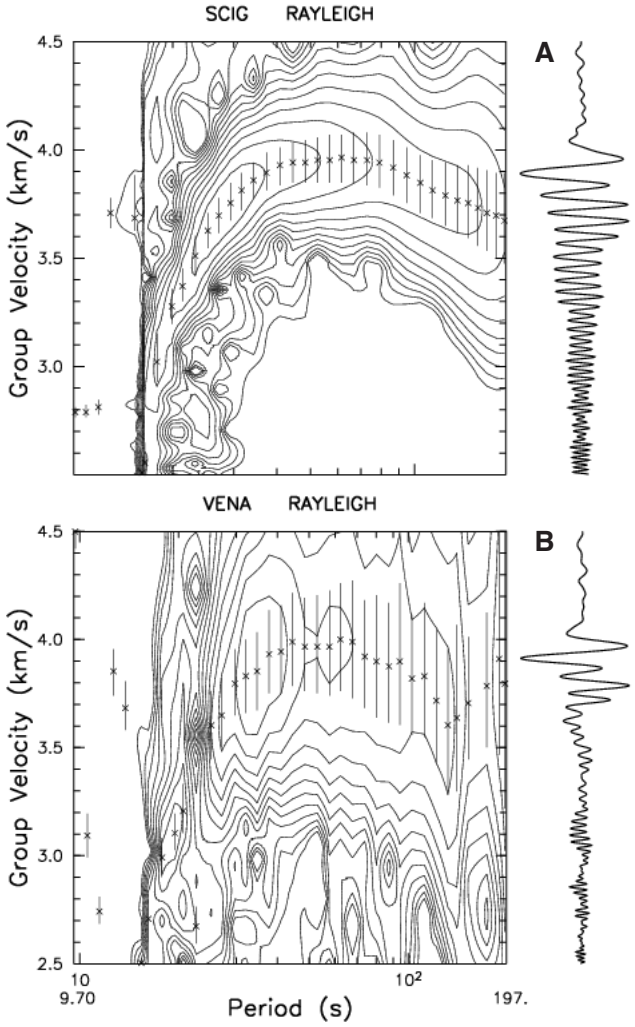

Figure 3.3: FTAN plots (Landisman et al., 1969; Dziewonski et al., 1969) showing single-station Rayleigh-wave group velocities vs. periods for the 1 March 2007 event (middle of the North Atlantic Ocean). The X symbols are computer-picked energy maxima for each period, the vertical lines span ±1 dB. Contours are placed every 3 dB. The corresponding waveforms are shown on the right sides. Panel (A) gives an example of a smooth FTAN plot for station SCIG that was used for data processing, and panel (B) shows an irregular FTAN plot for station VENA which was rejected. In (B), the contours are not smooth and well-behaved over all periods.

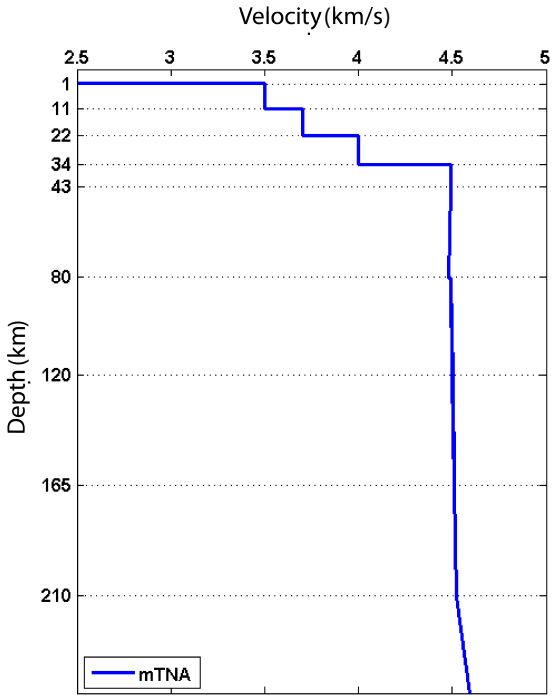

Figure 3.4: One-dimensional shear wave velocity profile used as a local reference Earth model. It is a composite model modified from the Tectonic North America (TNA) model (Grand and Helmberger, 1984) with the added P-wave velocities and densities from model AK135 (Kennett et al., 1995), and the Crust 2.0 crustal model (Bassin et al., 2000)

.

locations with respect to the slab are shown in Fig. 3.5. The interstation phase velocity measurements vary systematically along the MASE array, with a decrease in phase velocity from southwest to northeast, away from the subducting slab. The higher phase velocities are thus located above the region of flat slab subduction, consistent with the tomographic body-wave inversion of Husker and Davis, 2009.

depth (km)	ρ (kg/m^3)	Vp (km/s)	Vs (km/s)
1.0	2100.0	2.50	1.20
1.0	2700.0	6.00	3.50
11.0	2700.0	6.00	3.50
11.0	2900.0	6.60	3.70
22.0	2900.0	6.60	3.70
22.0	3100.0	7.20	4.00
34.0	3100.0	7.20	4.00
34.0	3580.1	8.04	4.49
43.5	3580.1	8.04	4.49
80.5	3502.0	8.04	4.49
120.5	3426.8	8.05	4.50
165.5	3371.1	8.18	4.51
210.5	3324.3	8.30	4.52
260.5	3366.3	8.48	4.61
310.5	3411.0	8.66	4.70
360.5	3457.7	8.85	4.78
410.5	3506.8	9.03	4.87
410.5	3931.7	9.36	5.08
460.5	3927.3	9.53	5.19
510.5	3923.3	9.70	5.29
560.5	3921.8	9.86	5.40
610.5	3920.6	10.03	5.50

Table 3.1: Modified Tectonic North America model (mTNA). Fig. 3.4 illustrates the V_S velocity profile of this model.

3.4 Azimuthally anisotropic phase velocity maps

3.4.1 Method

The two-station technique employed here enables us to measure path-averaged phase velocities $\bar{c}$ between two stations :

$$\bar{c}(T) = \frac{1}{d_2 - d_1} \int_{d_1}^{d_2} c(T, l) dl \tag{3.1}$$

where T indicates the period considered, and stations 1 and 2 are located along the great-circle path l at epicentral distances d_1 and d_2, respectively. We invert our path-averaged phase velocity measurements using a least-squares (LSQR) method (Darbyshire and Lebedev, 2009) previously employed by Beghein et al., 2010. With this method, the study area is parameterized by a 2-D triangular grid. The choice of the grid spacing is subjective, but the

spacing should remain smaller than the features we are trying to resolve, which themselves depend on the station spacing and the azimuthal coverage achieved. Cells that are too large would smooth the data unnecessarily and potentially hide interesting model features, while cells that are too small could display variations that are not resolvable with our data. After testing parameterization with $45, 60$, and 100 km spacing, we select the grid spacing of 60 km (for the total of 898 grid cells).

This method not only enables us to obtain isotropic phase velocity maps at different periods, but also allows us to model the azimuthal dependence of the phase velocity. In a slightly anisotropic medium, phase velocities can be expressed as (Smith and Dahlen, 1973):

$$c(T,\Psi) = c_0(T) + c_1(T)cos(2\Psi) + c_2(T)sin(2\Psi) + c_3(T)cos(4\Psi) + c_4(T)sin(4\Psi) \quad (3.2)$$

where c is the phase velocity, T is the period, Ψ is the azimuth, $c_0(T)$ is the isotropic term, and c_{1-4} are the azimuthal coefficients (Backus, 1970). The Eq. 3.2 can also be written as:

$$\boldsymbol{d} = \boldsymbol{G}\boldsymbol{m} \quad (3.3)$$

where where $\boldsymbol{d}$ is the data vector, $\boldsymbol{G}$ is the matrix describing the physical relationship between observations and model parameters, and $\boldsymbol{m}$ is the vector representing the parameters of the model c_{1-4}.

The directions Θ of fast propagation for Rayleigh waves and the amplitude A of the anisotropy can be obtained using :

$$\Theta_{2\Psi} = 1/2 \arctan(c_2/c_1), \quad (3.4)$$

$$\Theta_{4\Psi} = 1/4 \arctan(c_4/c_3), \quad (3.5)$$

$$A_{2\Psi} = \sqrt{(c_1^2 + c_2^2)}, \quad (3.6)$$

$$A_{4\Psi} = \sqrt{(c_3^2 + c_4^2)}. \tag{3.7}$$

Like most geophysical inverse problems, the inversion of Eq. 3.1 is non-unique, which means that a subjective regularization must be imposed. The anisotropic and isotropic terms are smoothed independently, and each period is treated separately from the others. We use the trade-off curves (or L-curves) to choose a damping value for each period (Fig. 3.6). The preferred damping is chosen near the corner of the L-curve. After a damping value is chosen for the isotropic term, we proceed with varying the damping for the anisotropic terms (first the 2Ψ terms, then the 4Ψ terms, independently). Even though dispersion curves are obtained for periods between 16 s and 171 s, our ray coverage is not sufficient to reasonably resolve phase velocity anomalies at periods greater than 100 s (a large damping is needed and no significant variation in phase velocity is found). We thus focus the rest of the manuscript on the results obtained at periods between 16 s and 100 s.

To evaluate the significance of the reduction in χ^2 misfit when adding anisotropy, we perform standard F-tests (Bevington and Robinson, 1992) following the method described by Trampert and Woodhouse, 2003: we vary the damping and compute the χ^2 misfit and the trace of the resolution matrix $\boldsymbol{R}$ for the isotropic model, for the 0Ψ+2Ψ model, and for the model that includes all anisotropic terms (0Ψ, 2Ψ, and 4Ψ). We define χ^2 as:

$$\chi^2 = \frac{1}{N-M}(\boldsymbol{d} - \boldsymbol{Gm})\boldsymbol{C_d^{-1}}(\boldsymbol{d} - \boldsymbol{Gm}) \tag{3.8}$$

where N is the total number of data, M is the trace of the resolution matrix $\boldsymbol{R}$, and $\boldsymbol{C_d^{-1}}$ is the data covariance matrix.

The resolution matrix $\boldsymbol{R}$, which is not readily calculated by the LSQR method, is determined for various damping values following Trampert and Woodhouse, 2003. Each column j of the matrix $\boldsymbol{G}$ that describes the physical relation between the data and the model

parameters is inverted :

$$\boldsymbol{R_j} = \boldsymbol{L}\boldsymbol{G_j} \tag{3.9}$$

where $\boldsymbol{R_j}$ is column j of matrix $\boldsymbol{R}$, $\boldsymbol{L}$ is the LSQR operator, and $\boldsymbol{G_j}$ is column j of matrix $\boldsymbol{G}$. In our case, $\boldsymbol{R}$ is a 4490x4490 matrix, with 898 rows and columns for the isotropic part, 1796 rows and columns containing 2Ψ sin and cos components, and 1796 rows and columns with 4Ψ sin and cos components (see Eq. 3.2). Fig. 3.7 displays χ^2 as a function of the trace of $\boldsymbol{R}$ for the isotropic and anisotropic inversions for the period of 28 s. This Figure, combined with the F-tests, shows that the 2Ψ terms are needed to explain the data, but the 4Ψ terms do not improve the data fit significantly. We obtain similar outcomes for the other periods. Hence, in the following, we discuss only the isotropic (0Ψ) and 2Ψ terms.

To evaluate the quality of our data coverage, we conduct isotropic and anisotropic resolution tests for all periods. Figures 3.8 and 3.9 show three representative tests at a period of 44 s : (1) a test of the isotropic inversion with a checkerboard input (Fig. 3.8), (2) a test of the anisotropic inversion with a purely isotropic input (Fig. 3.9, A and B), and (3) a test of the anisotropic inversion where the input has variations in both isotropic velocity and anisotropy (Fig. 3.9, C and D). In the anisotropic tests, the isotropic inputs are chosen to coincide with our preferred phase velocity model at the period considered. Fig. 3.8 and 3.9 demonstrate that the input isotropic and anisotropic models are well recovered in the middle of the study area, close to the MASE array, marked by the green line on the figures, with some discrepancies and smearing north of 21° latitude and east of 96° longitude (shaded area in the figures). We find that an anisotropic inversion of an isotropic input model (Fig. 3.9A and B) yields an output model with virtually no anisotropy (less than 0.5%) everywhere in the study area. Because the resolution of our models is better in the center of our study area, where the number of stations, and therefore the number of crossing paths, is higher, we will concentrate the discussion of the results on that part of the region.

Trade-offs between isotropic and anisotropic terms in the inversion of Eq. 3.1 can affect

the results. The synthetic tests shown in Fig. 3.9A and B demonstrate that our inversion scheme can detect the absence of anisotropy, and therefore that there is little trade-off between the isotropic and anisotropic terms. Another way to analyze these trade-offs is by computing the resolution matrix $\boldsymbol{R}$ from Eq. 3.9, which we do using the damping values chosen for our preferred anisotropic model (Fig. 3.10). Each line of $\boldsymbol{R}$ corresponds to a model parameter, and the matrix is divided into nine sub-matrices c_i and c_j $(i, j = 0, 1, 2)$, where c_0 spans parameters that correspond to the 0Ψ term, and c_1 and c_2 span parameters that correspond to the two 2Ψ terms. The off-diagonal submatrices c_i and c_j $(i \neq j)$, represent trade-offs between the three terms, and the off-diagonal elements within the submatrices c_i and c_i indicate lateral trade-offs, i.e., trade-off within the same c_i term but at different geographic locations. Figure 3.10 shows the existence of some lateral trade-offs, which result from imperfect ray coverage and lateral smoothing. It also demonstrates that trade-offs exist between the isotropic and anisotropic terms and between the two 2Ψ terms, but that they are relatively small. The synthetic tests performed in addition to the resolution matrix shown here give us confidence in the significance and resolution of the obtained anisotropy.

3.4.2 Results

The obtained phase velocity maps are shown in Fig. 3.11 for periods of 18 s, 44 s, and 85 s. The results reveal lateral variations in isotropic phase velocities at all periods, consistent with the presence of a flat slab : phase velocities are generally larger than average in the forearc, and lower than average near the TMVB. At short periods (16 s-33 s), there are strong lateral variations in phase velocities and anisotropy. Considering the depth sensitivity of Rayleigh waves at these periods (see sensitivity kernels in Figure 3.12), these rather complex variations may reflect changes in the crustal and mantle lithospheric structure, and deformation history. At periods of 38 s and higher, the phase velocity anomalies and anisotropy are smoother. It is remarkable to note that the transition between the faster and slower than average

phase velocities follows the isodepth lines of the local seismicity, both in the flat and steeper portions of the slab.

We also find an east-west variation in phase velocity anisotropy at all periods, and a change in the fast direction between the forearc and the backarc. Both findings are likely to be the signature of complex 3-D deformation at depth. Interestingly, at periods of 38 s and higher, the fast direction of propagation in the western part of our study region is perpendicular to the trench near the coast. In the southeast, the fast direction found above the slab is subparallel to the trench at most periods. In the backarc, azimuthal anisotropy is present at all periods up to 85 s, with the fast direction of propagation often at a steep angle to the strike of the arc. Considering that at periods larger than 33 s our data are mostly sensitive to structure below 50 km depth (Fig. 3.12), and considering previous estimates of the slab geometry from body wave data (Husker and Davis, 2009), the orientation of the fast direction likely reflects lithospheric and/or asthenospheric deformation.

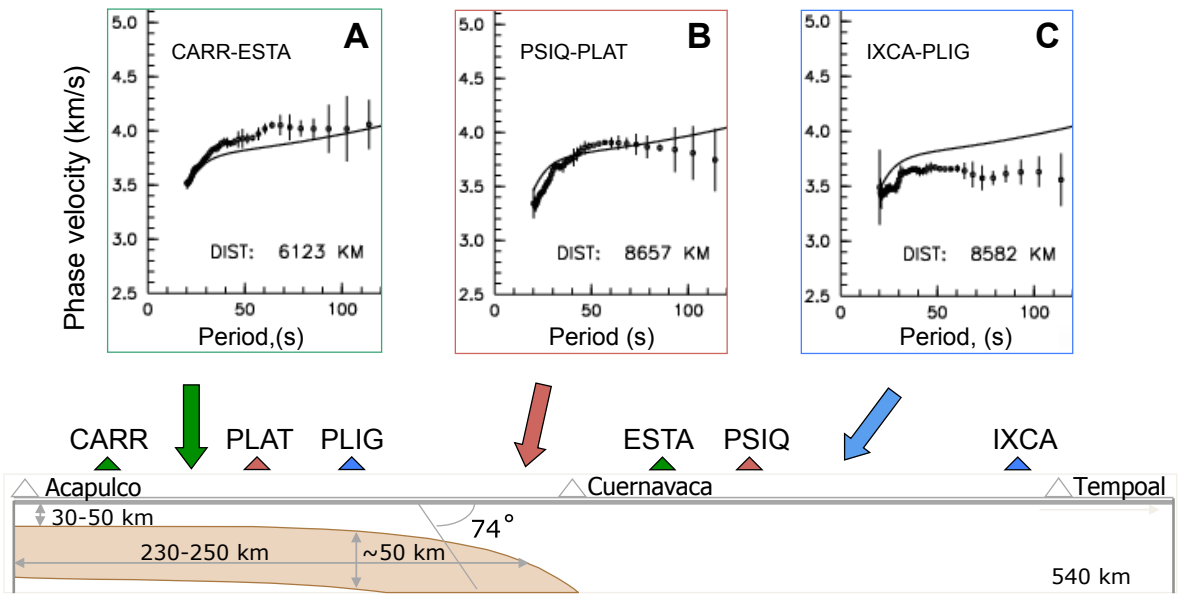

Figure 3.5: Dispersion curves along the MASE transect for three pairs of stations: (a) CARR and ESTA, located right above the slab, (b) PSIQ and PLAT, located only partially above the slab, and (c) IXCA and PLIG, located away from the slab. The location of the slab is assumed based on previous 2-D studies (e.g. Husker and Davis, 2009). The black dots and vertical lines give the interstation phase velocities and uncertainties measured by the two-station method. The solid lines indicate the dispersion curves predicted by the 1-D modified Tectonic North America model (mTNA). Note the systematic differences between the dispersion curves, both in terms of their departure from the 1-D model and in terms of their variation along the transect. The phase velocities above the slab are larger, and diminish while moving away from the slab, as we would expect.

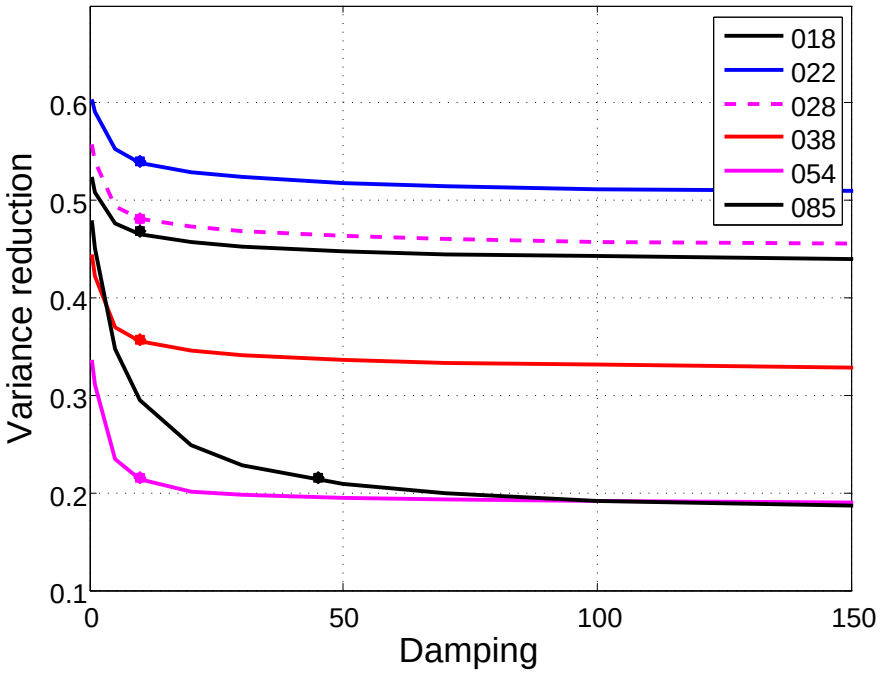

Figure 3.6: L-curves (trade-off curves) for the periods of $18, 22, 28, 38, 54$, and $85\,\mathrm{s}$. The L-curve displays a measure of the misfit of each model against a measure of the complexity of the model itself (damping). The dots show the points used as damping values for the preferred model; they differ for different periods.

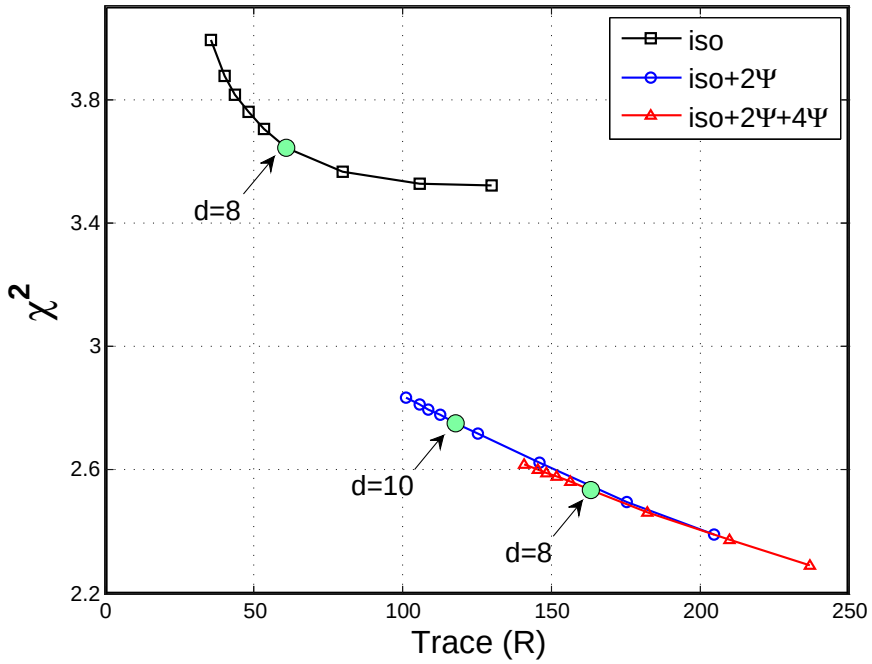

Figure 3.7: An example of reduced χ^2 as a function of the trace of $\boldsymbol{R}$ for the isotropic (squares), isotropic and 2Ψ inversions (circles), and isotropic and full anisotropy of 2Ψ + 4Ψ (triangles) for the period of T=28 s. The values for the χ^2 and trace are calculated for a range of damping parameters with the values of the preferred model marked by arrows. The dampings increase from right to left. We can see that the 4Ψ terms do not improve the fit significantly, and thus only isotropic and 2Ψ terms are used for anisotropic depth inversions.

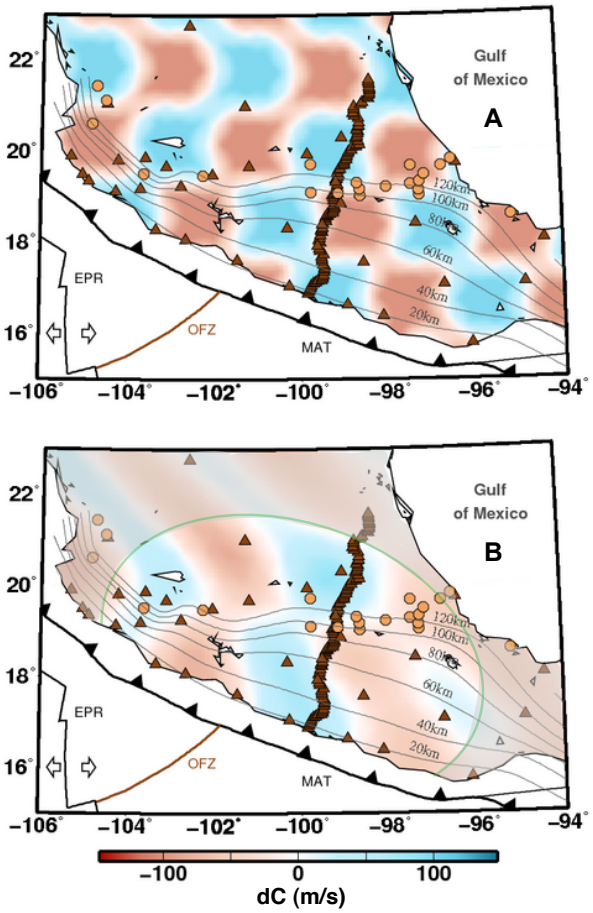

Figure 3.8: Isotropic resolution test for $T = 44\,s$. The comparison between the isotropic checkerboard input model (A) and the recovered isotropic phase velocity map (B) shows that the area around the MASE array (the non-shaded region) is well-resolved. The resolution near the MASE array is good due to the high number of the intersecting paths.

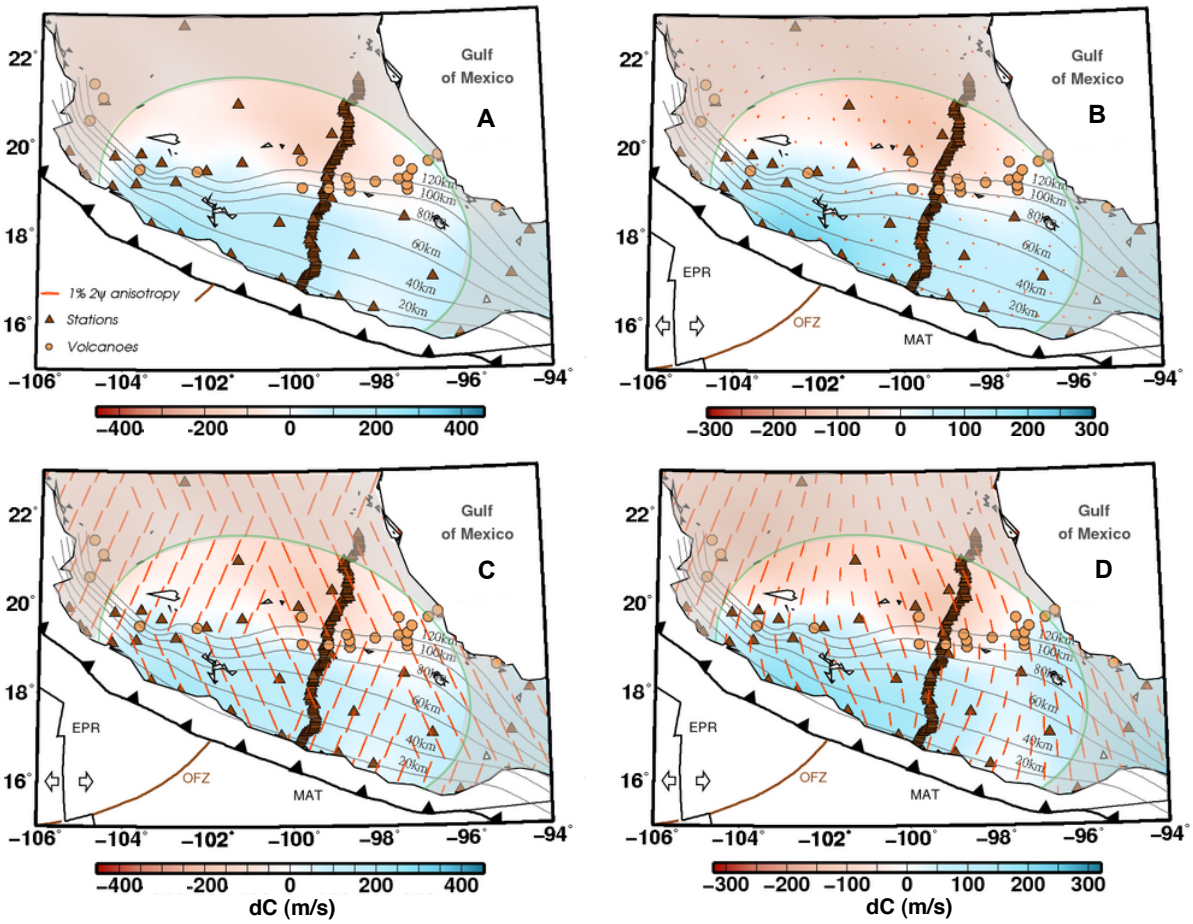

Figure 3.9: Anisotropic resolution tests for $T = 44\,s$. Panels (A) and (B) correspond to anisotropic inversions of an isotropic input model, and panels (C) and (D) show anisotropic inversions of an anisotropic input model. The input models are shown to the left and the output models are represented on the right. The input model with zero anisotropy (A) is chosen to coincide with the isotropic component of our preferred model of the region.

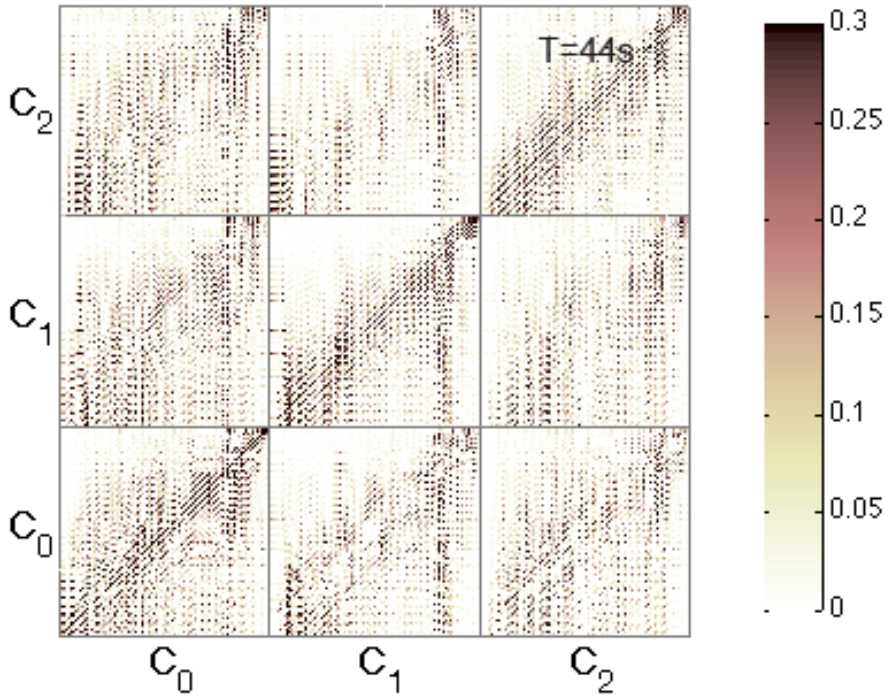

Figure 3.10: Resolution matrix for 44 s period calculated using our chosen damping. The nine submatrices represent trade-offs between the isotropic terms of the phase velocity map c_0, and the 2Ψ terms c_1 and c_2 of Eq. 3.2. The elements of each submatrix represent our 898 triangular grid cells. The off-diagonal submatrices indicate trade-offs between the isotropic and anisotropic terms and between the two anisotropic terms. The off-diagonal elements of the diagonal submatrices indicate lateral trade-offs, i.e. trade-offs within the isotropic or one anisotropic term at different geographic locations.

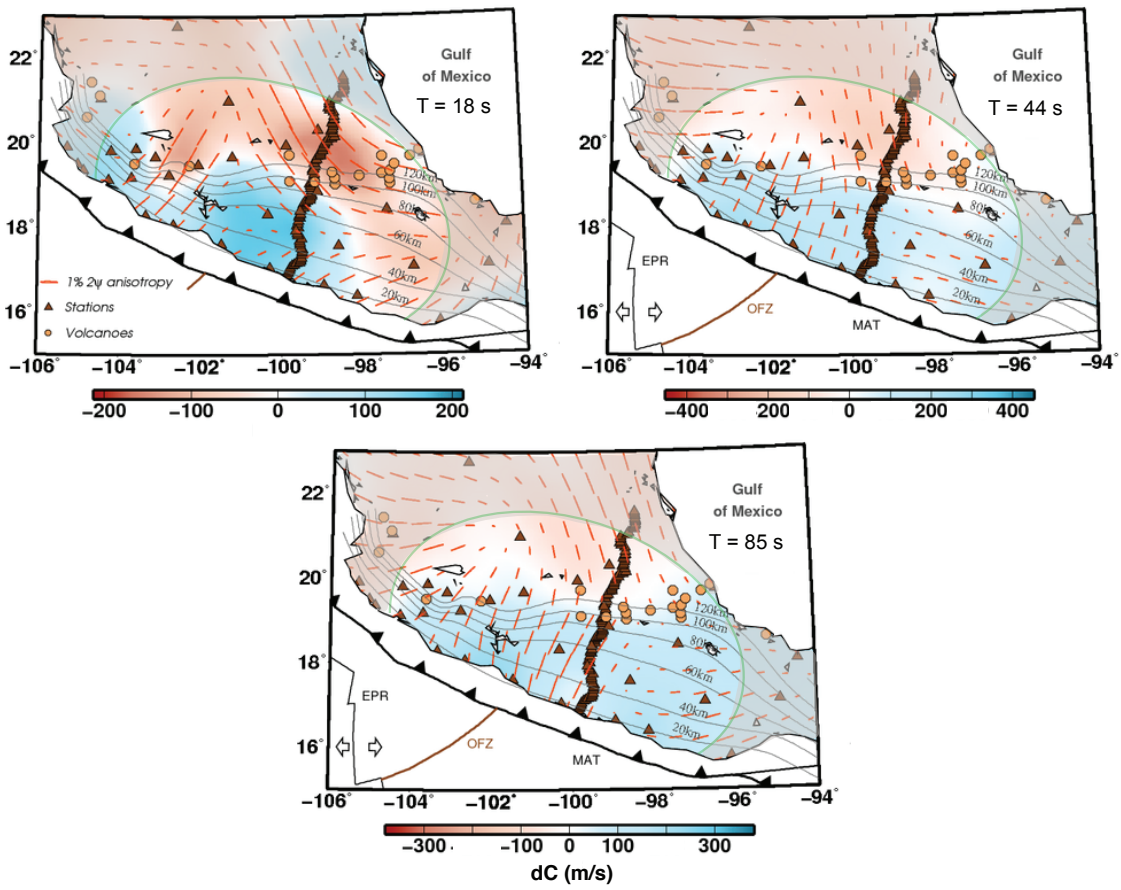

Figure 3.11: Anisotropic phase velocity maps for selected periods. The color scale represents deviations in isotropic phase velocity with respect to the phase velocity calculated for our local reference model mTNA. The red lines show both the fast direction and the magnitude of the 2Ψ-anisotropy. The non-shaded area (with the green semi-elliptical boundary) marks the well-resolved area as determined by the resolution test (Fig. 3.8). The isolines of slab depth based on local seismicity are shown by grey lines as in Fig. 1.1.

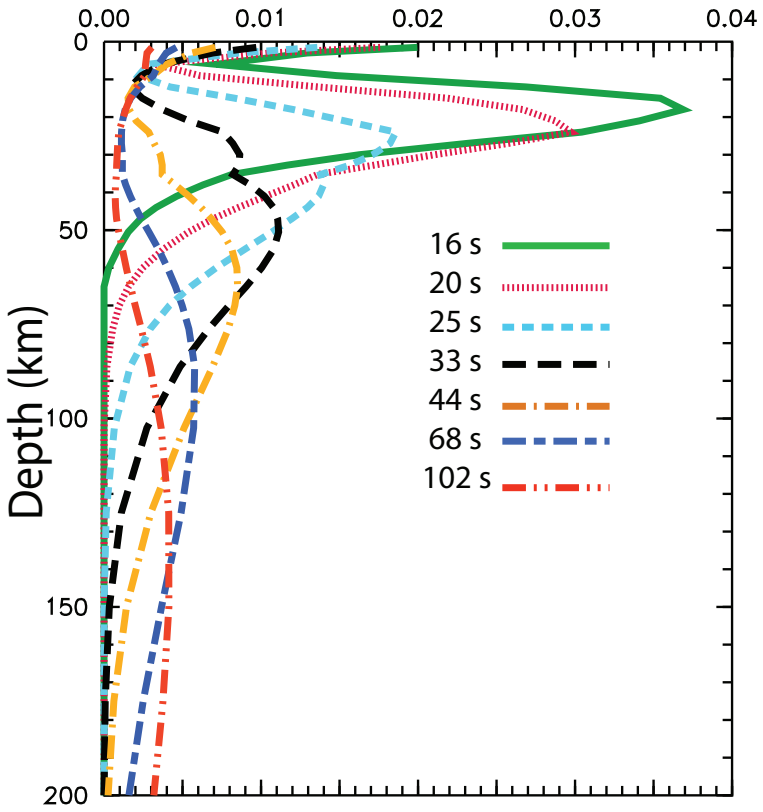

Figure 3.12: Sensitivity kernels for V_S as functions of depth for several of the different periods analyzed. The kernels are the partial derivatives for fundamental-mode Rayleigh wave phase velocities with respect to V_S based on the reference velocity model mTNA.

CHAPTER 4

Three-dimensional models of S-wave velocity and azimuthal anisotropy

This chapter is partially based on the following publication:
Stubailo, I., Beghein, C., and Davis, P. M., Structure and anisotropy of the Mexico subduction zone based on Rayleigh-wave analysis and implications for the geometry of the Trans-Mexican Volcanic Belt. JGR, 2012.

4.1 Shear-wave velocity structure

Phase velocities correspond to a depth-integrated image of the upper mantle. In order to obtain a 3-D model, we need to invert the phase velocity maps for shear wave velocity and anisotropy.

Perturbations in the isotropic part of the phase velocity c_0 correspond to the depth average of perturbations in shear-wave velocity (δV_S), P-wave velocity (δV_P), and density ($\delta\rho$) weighted by sensitivity kernels (Fig. 3.12) :

$$\delta c_0 = \int_0^a [K_{V_S}(r)\delta V_S(r) + K_{V_P}(r)\delta V_P(r) + K_\rho(r)\delta\rho(r)]dr \tag{4.1}$$

where a represents the radius of the Earth, and $K_m(r)$ is the phase velocity sensitivity kernel or partial derivative with respect to model parameter m (here m stands for V_S, V_P, and ρ).

In this work, the isotropic part of the phase velocity maps is inverted for V_S via a linearized least-squares inversion using code $surf96$ (Herrmann, 1987; Herrmann and Ammon, 2002).

We impose a depth parameterization in terms of three layers down to 200 km depth, with the top layer representing the crust and the other two layers being located in the mantle (Fig. 4.1D). The middle layer spans depths going from the Moho, as constrained by receiver function analyses (see explanations below), to 100 km depth. We choose approximately $50 - 60$ km as the average lithosphere thickness based on the subducting plate age

Herrmann's method uses differential smoothing during the inversion, which means that it damps the differences between V_S in adjacent layers. After investigating a range of values for the damping parameter, we choose to start with a damping of 10% of the maximum eigenvalue of the data kernel, decreasing it to 3% after five iterations in the total of 30 iterations. The selection of the damping values and number of iterations is based on the final solution stability and improvement in misfit.

The depth inversions are carried out at every grid cell that parametrizes the study area (Section 3.4), and the resulting shear-wave velocity profiles are combined to form a 3-D V_S model of the region as displayed in Fig. 4.1. Our model shows lateral variations in V_S at all depths, with larger values in the south of the study region, most likely reflecting the presence of the slab, and slightly lower in the northern part of the region. We find lateral variations in V_S of approximately 0.3 km/s in the mantle and crust. Note that, since our 3-D V_S model results from the inversion of phase velocity maps that are themselves generated by inversion of dispersion measurements, our V_S model amplitude is indirectly affected by the smoothing applied during the construction of the phase velocity maps. A lower damping of the shortest period dispersion data may have resulted in stronger phase velocity anomalies and stronger crustal V_S.

4.2 Azimuthal anisotropy

At a given period T, the phase velocity azimuthal anisotropy relates to azimuthal anisotropy at depth through equations similar to Eq. 4.1 :

$$c_1 = \int_0^a K_G(n) G_c(r) dr \tag{4.2}$$

$$c_2 = \int_0^a K_G(n) G_s(r) dr \tag{4.3}$$

where c_1 and c_2 are the 2Ψ anisotropic terms of Eq. 3.2, G_c and G_s are elastic parameters that describe the azimuthal anisotropy of vertically polarized shear-waves, and K_G describes the sensitivity of Rayleigh waves to G_c and G_s.

We invert Eqs. 4.2 and 4.3 for $G_c(r)$ and $G_s(r)$ using a singular value decomposition (SVD) method. We follow the procedure described by Matsu'ura and Hirata, 1982 to determine how many eigenvalues to keep in the reconstruction of the model. The inversion is done over the same layers used for the inversion of the isotropic term. After obtaining a model for G_s and for G_c, we calculate the amplitude A of the anisotropy and the fast direction of propagation Θ for vertically polarized shear-waves at every grid cell and in every layer using :

$$A = \sqrt{(G_c^2 + G_s^2)} \tag{4.4}$$

$$\Theta = 1/2 \arctan(G_s/G_c) \tag{4.5}$$

The results are displayed in Fig. 4.1. In our interpretation, we concentrate on the patterns in the mantle lithosphere and asthenosphere (Fig. 4.1B,C). Unlike most subduction zones that display anisotropy with the fast direction parallel to the trench (Long and Silver, 2008), our results show a more complex pattern of anisotropy, with the fast azimuth of propagation

perpendicular to the trench northwest of MASE and almost parallel to the trench in the southeast (Fig. 4.1B, C). There is a clear and sharp near-vertical transition between 45 and 200 km depth showing $0.5 - 2\,\%$ variations in anisotropy with higher amplitudes where the fast direction is parallel to the trench. In the crust (Fig. 4.1A), we observe a complex anisotropy pattern. Overall, the crustal anisotropy does not coincide with that of either mantle lithosphere (Fig. 4.1B) or asthenosphere (Fig. 4.1C). This is not surprising, since anisotropy at different depth likely has different origins (Lin et al., 2010; Yang et al., 2011): the anisotropy in the crust correlates with geologic/tectonic features whereas the anisotropy in the upper mantle depends on temperature variations and mantle flow. A similar variation in anisotropic behavior with depth is also observed in the western United States (Lin et al., 2010; Yang et al., 2011).

Our anisotropy results combined with our S-wave velocity model enable us to obtain new insights into the Mexico subduction zone, as discussed in the next section.

4.3 Discussion

4.3.1 Evidence for tear in the slab along the Orozco Fracture Zone

Our results confirm the conclusions of prior studies (Kanjorski, 2003; Pardo and Suarez, 1995; Blatter et al., 2007) that the angle of subduction varies substantially along the trench. There are several distinctive features observed with V_S that vary gradually between layers in Fig. 4.1D. The higher velocities of 4.4 km/s are seen in the middle layer (Fig. 4.1B) in the subduction zone near the coast, extending inland beneath the southern part of the MASE array. We associate these higher velocities with the slab subduction, specifically with a shallow flat slab under the MASE and a steep slab to the west of it. This finding is consistent with the shallow slab location determined by Pardo and Suarez, 1995; Perez-Campos et al., 2008; Husker, 2008, and Husker and Davis, 2009 based on seismicity patterns,

receiver function tomography, and P-wave tomography, respectively. The slabs at the depths of up to 100 km appear to be almost disconnected.

Another striking feature is a low velocity zone in the northern part of the MASE array (Fig. 4.1B), with a velocity contrast of 0.3 km/s between the low and high velocity regions. We attribute the velocity reduction to the presence of water or melt in a mantle wedge as a consequence of the subduction process. It is interesting to note that the low velocity area almost coincides with the location of volcanoes from the TMVB. Our results show a wave velocity lower than average near the location of the most recent volcanic activity (Osete et al., 2000), but also at the location of older volcanoes. The fact that we cannot distinguish between old and young volcanic areas is due to the limited lateral resolution of our surface waves. The results for the bottom layer located between 100 and 200 km depth (Fig. 4.1C) exhibit a low velocity zone in the northern part of the MASE array and an absence of the high shear velocities associated with the flat slab beneath the southern part of the MASE array. This can be explained by the fact that the flat part of the slab is mostly absent at this depth and its steeply dipping part at 74 is not detectable by the surface waves since it is quite thin as was shown by the P-wave tomography (Husker and Davis, 2009). On the other hand, the mantle wedge to the north is much wider and more detectable by Rayleigh waves and corresponds to a low velocity area. The asthenospheric low velocities beneath the TMVB are likely caused by altered mantle due to slab dehydration and/or increase in temperature in the mantle wedge. Although the slab itself is not visible as a high velocity zone, the transition to the low velocities in the north can also be used for locating the slab.

Higher velocities are seen to the west of the MASE array. This is probably explained by the large detectable size of the steeply dipping slab that crosses this zone. We note that the isodepth line at 120 km depth runs on the edge of the blue region supporting the presence of the slab. The low velocity zone to the northwest of the steep slab is close to the boundary of our well-resolved area and hence potentially suspect, but it can be associated with a possible

signature of the mantle wedge associated with subduction of the Rivera slab as mentioned in Yang et al., 2009.

We can thus observe that the subducting slab in the study area is separated into two sections, one of which is flat and shallow (section 3, Fig. 1.1) while the other one is steep and deep (section 2, Fig. 1.1). An important issue is how the subduction changes across the boundary between the flat and steep portions. One possibility is that the slab is continuous, experiencing relative rapid but continuous change in subduction angle (Fig. 4.3.1, bottom). Such a scenario was hypothesized by Pardo and Suarez, 1995. However, our results on anisotropy, combined with prior studies on the ocean plate structure, age and convergence rates, as well as the slab rollback and retreat (Mori et al., 2007; Orozco et al., 2007; Manea et al., 2005), point towards the scenario with a tear in the slab, as illustrated in Fig. 4.3.1 (top). Note that the study area is rotated in Fig. 4.3.1 relative to that of Fig. 3.11 and 4.1, to give a better view of the slab morphology. The location of the transition from steep (B) to shallow (A) subduction is consistent with the location of the Orozco Fracture Zone (OFZ), which separates the older, cooler and denser oceanic crust (17.6 Ma old) from the younger oceanic crust and lithosphere (12.3 Ma old) (Manea et al., 2005; Pardo and Suarez, 1995).

The existence of the tear is further supported by our anisotropy results. The fast directions in the mantle lithosphere and asthenosphere are, in general, parallel to the trench, except near the OFZ. In the vicinity of the OFZ they rotate to become near-parallel with the OFZ projected path, eventually deviating slightly to the west (Fig. 4.1B and 4.1C). One of most likely causes of anisotropy is the flow-induced, lattice-preferred orientation of olivine. This theory is supported by a study based on P wave tomography results (Yang et al., 2009) that describes the mantle flow between our steep slab (B) and the Rivera slab (C) as caused by an existance of a gap between the Rivera and Cocos. Studies on GPS velocities (DeMets et al., 1994) and volcanic migration (Blatter et al., 2007) suggest that slab retreat and/or rollback are occurring at $\sim$5 cm/year in our study area. The rollback/retreat should displace

mantle asthenosphere and, in the presence of the slab tear, the mantle material would flow through it. The associated toroidal flows (Fig. 4.3.1, top, blue arrows) would give rise to the anisotropy pattern obtained in our study (Fig. 4.1B and 4.1C). The "currents" converge in front of the steep slab B, creating a characteristic line. This is similar to the explanation of the circular pattern of anisotropy in the Western US given by Zandt and Humphreys, 2008. Note that the flow between segments A and B may also contribute to the flatness of subduction, dynamically elevating the flat slab section. We conclude that the A-B tear occurs where the plate is weakened by the presence of the fracture zone. In the back arc, the steep angle of mantle anisotropy to the strike of the arc can be explained by the flow in the mantle wedge (Fig. 4.3.1, top, green arrows).

Several studies discussed the detachment of the deeper Farallon slab and its effect on the subduction structure of the region. For instance, the tomographic study of Gorbatov and Fukao, 2005 presents evidence for the slab tear and resulting gap caused by the (30 Ma) collision of the East Pacific Rise and the coast of California. The gap widened and propagated southeastwards. On the basis of the tomographic images, they infer the present gap between the subducting Cocos plate and the Farallon slab is located much further to the north and deeper than our study area. They also proposed that the tearing is responsible for the overall shape of the Cocos subducting slab in terms of its flat and steep portions. A second more recent tear, further south, was proposed by Ferrari, 2004 in which the Farallon slab detachment started beneath the present southern Gulf of California quickly propagating over in the southeast direction between 11.5 and 6 Ma. It would have caused migrating volcanism induced by the hot upwelling subslab asthenosphere. The proposed tear crosses our study region but would now be located at larger depths ($\sim$500 km) than we can resolve.

4.3.2 Implications for the geometry of the TransMexican Volcanic Belt (TMVB)

It is commonly pointed out that TMVB is oblique to the trench (Ferrari, 2004; Pardo and Suarez, 1995). The slab model with the tear allows for an alternative interpretation of TMVB as a combination of two segments both of which are parallel to the trench (Fig. 4.2). One segment of the volcanic belt (B′ in Fig. 4.2) is generated by the steeper portion of the slab (B in Fig. 4.2), and hence it is located closer to the trench. The other segment (A′) is generated by the flatter portion of the slab and hence it is farther from the trench. Each of the segments of the volcanic belt is parallel to the trench, consistent with typical understanding of the subduction zone volcanism (Mori et al., 2007; Manea et al., 2013). However, the difference in their distance to the trench results in what appears to be an oblique angle between the TMVB, taken as a whole, and the trench. Note that the oblique character of TMVB has already been linked to the changing subduction angle by prior studies (e.g., Pardo and Suarez, 1995; Manea et al., 2013. However, what is new in our results is the possibility that the TMVB is actually segmented.

This new interpretation allows for a natural explanation for the existence of the Tzitzio gap in volcanism (e.g., Blatter et al., 2007. The gap occurs right on top of the projected path of the OFZ, and hence on top of the proposed tear in the slab structure. In this interpretation, the Tzitzio gap is simply the result of the two parallel segments that are displaced with respect to each other, as illustrated in Fig. 4.2. The zone between them does not have steeply subducted material that would generate volcanism.

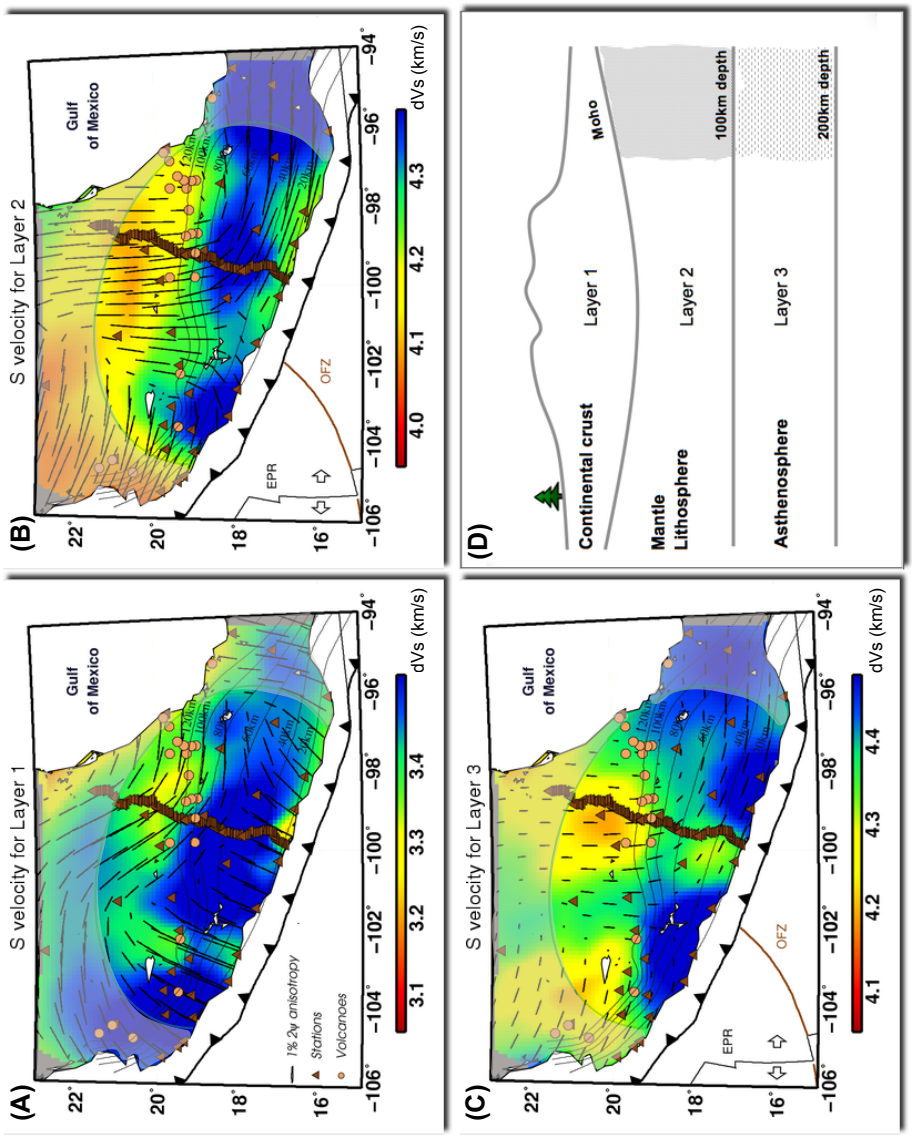

Figure 4.1: 3-D shear-wave velocity and anisotropy model based on the inversion of our Rayleigh wave phase velocity maps. (A-C) Shear-wave velocities (color) and fast directions (black dashes) averaged over each of the three layers of the model (D). Layers 1 and 2 have variable depth to account for lateral changes in crustal thickness. The velocity variations in the mantle lithosphere (layer 2) show high velocities in the subduction zone near the coast, extending inland beneath the southern part of the MASEarray. These higher velocities are likely associated with the flat slab. Asthenospheric velocities (C) have low values beneath the TMVB, probably due to altered mantle from slab dehydration.

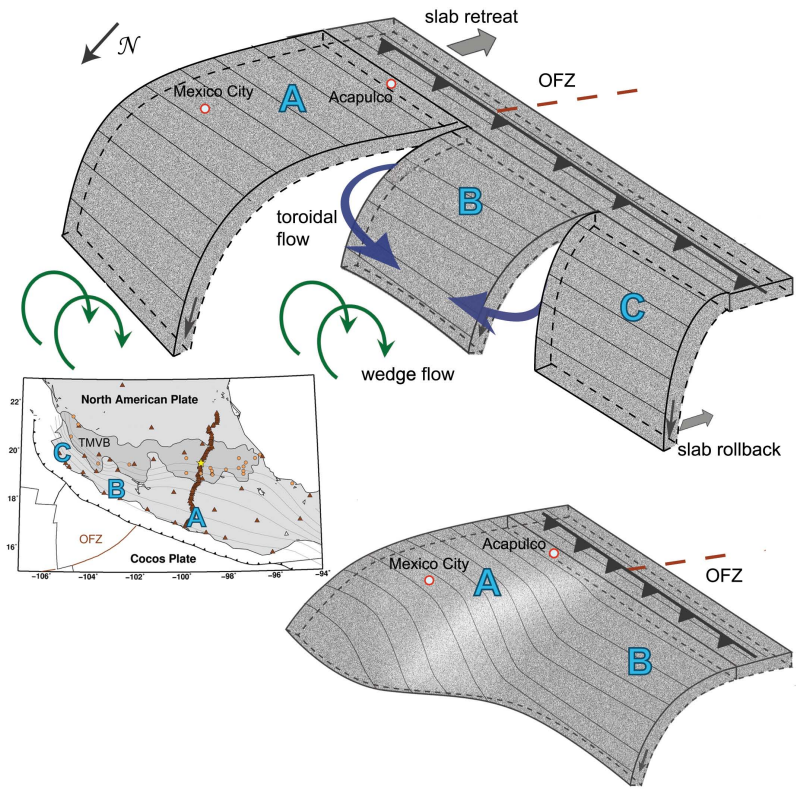

Figure 4.2: Two potential interpretations of the subduction structure in Mexico. *Top*: The flat (A) and steep (B) portions of the slab discussed in this paper separated by a tear. This is our preferred model that explains the anisotropy pattern (Fig. 4.1). The slab retreat/rollback proposed for the area (Mori et al., 2007; Manea et al., 2013) should displace the mantle asthenosphere, causing a toroidal flow through the tear and around the steep part of the slab (the blue arrow between A and B). The flow would explain the rotation of the fast direction in the anisotropy inversion. The tear between the two parts of the slab coincides with the projected path of the OFZ that separates the Cocos plate into areas of different ages. In addition, a mantle flow through the tear between the steep slab (B) and the Rivera slab (C) was observed in Yang et al., 2009 based on P-wave tomography results. The converging flows from both sides of the steep slab B along with a wedge flow (green arrows), that has fast directions perpendicular to the trench in the back arc, explain the sharp change in the anisotropy direction line in front of the slab B (Fig. 4.1). *Bottom*: The scenario in which the transition from the flat to steep subduction is continuous. In this scenario, the fast anisotropy direction perpendicular to the trench would be caused by the wedge flow which may be further enhanced by the slab retreat/rollback. This scenario does not explain the observed continuous rotation of the fast directions towards the OFZ that separates the two modes of subduction. *Insert*: The map view of the area with the locations of slab portions A, B, and C.

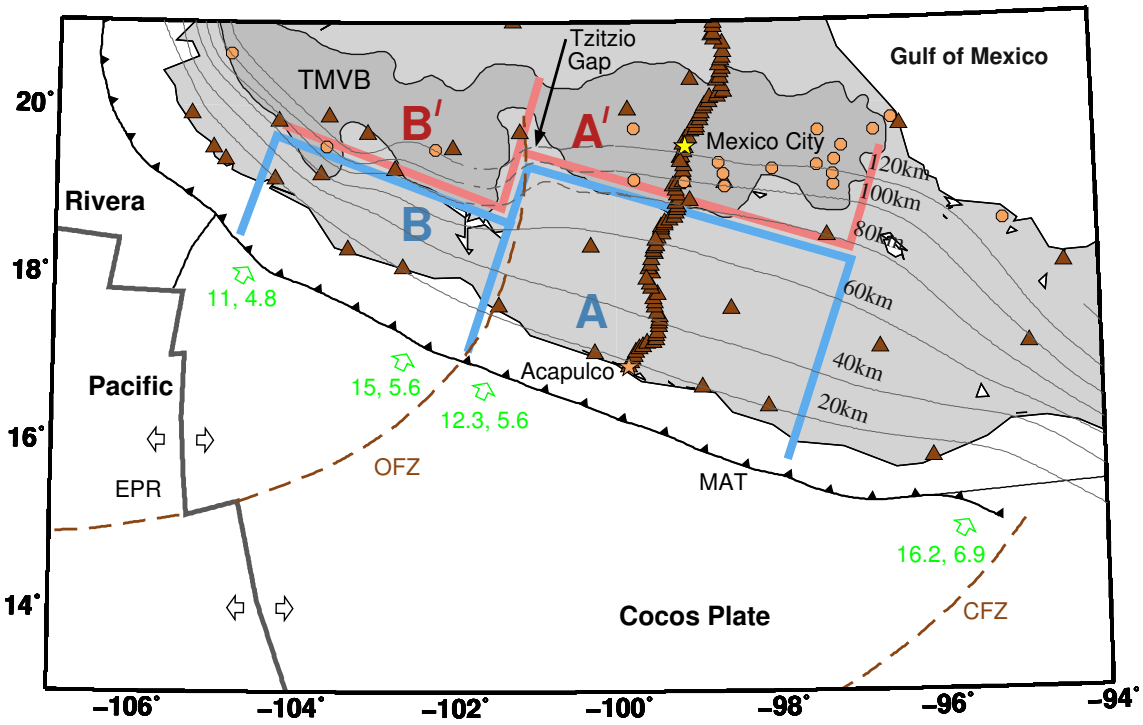

Figure 4.2: Interpretation of the TMVB structure as consisting of two trench-parallel segments. The segments (red areas A′ and B′) are signatures of the two segments of the subducting slab, the flat one (blue area A) and the steep one (blue area B), respectively. The two segments are independently parallel to the MAT, as typical for subduction zones, while the entire TMVB appears oblique to the MAT if the two segments are considered together. The projected path of the OFZ constitutes the boundary between the two segments. The segmented nature of the TMVB with the off-set in the distance to the trench is a natural explanation for Tzitzio gap in volcanism (Blatter et al., 2007). The sketch of the area is based on Manea et al., 2006 and Wilson, 1996. Triangles indicate several seismic stations used in the study, circles are the local TMVB volcanoes, OFZ, CFZ, and MAT denote Orozco Fracture Zone, Clipperton Fracture Zone, and Middle America Trench, respectively. The thick grey lines show the boundaries between tectonic plates. Green numbers are the sea floor ages in Ma and plate convergence rates in cm/year.

CHAPTER 5

Shear-wave splitting analysis

5.1 Introduction

To further study anisotropy in the Mexico region, we perform shear wave splitting analysis. When a linearly polarized shear wave propagates through an anisotropic medium, assumed to be azimuthally anisotropic, the shear wave splits into two separate waves traveling at different velocities. One can recover the original polarization of the split shear waves recorded at surface stations which gives information about the anisotropic medium (Silver and Chan, 1991; Vinnik et al., 1992; Montagner et al., 2000).

We use the SKS and SKKS phases for the calculation of the shear wave splitting parameters. The conversion from P to S waves at the CMB ensures that the shear waves have linear polarization and carry no effects of the source anisotropy (Fig.5.1), since a shear wave cannot propagate through a gas or a liquid and a P wave has only radial motion. The vertically (i.e. radially) polarized shear wave (SV) splits into fast and slow parts traveling through the azimuthally anisotropic medium. The fast and slow waves arrive at the seismic station out of phase and the splitting can be characterized by the splitting phase shift time Δt and the fast direction ϕ. The angle ϕ is measured between the North direction and the fast seismic direction and is referred to as the fast polarization azimuth. The Δt and ϕ reflect the total anisotropy encountered by a wave traveling from the CMB, and hence this technique has no depth resolution. The time delay Δt observed between the slow and fast shear waves is proportional to the ray path length and the magnitude of anisotropy along the ray path. In

the case of a dipping axis of anisotropy, the fast polarization direction is not in the horizontal plane. However, most often, only the horizontal (i.e., surface-parallel) components are analyzed for shear-wave splitting, and therefore only the horizontal projection of the fast polarization direction is obtained. This is the analysis performed here, and hence we use the data for East and North components only.

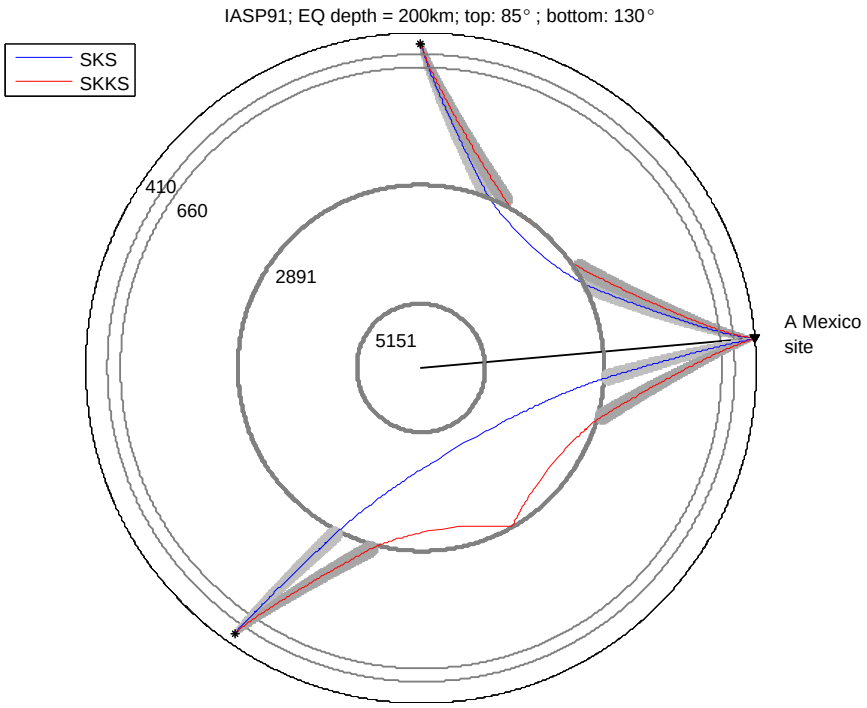

Figure 5.1: Travel paths of SKS and SKKS phases for events that occur at different distances from a Mexico seismic site. The shaded area around the rays corresponds to the Fresnel zones. The Core-Mantle Boundary (CMB) is marked by the circle at the depth of 2891 km.

5.2 Data selection and magnetic declination correction

The data selection is governed by different considerations than those for the surface wave study. We consider teleseismic events with locations within arc distances (Δ) of 90°-110°

for SKS and 100°-135° for SKKS with respect to a representative station, to limit ourselves to events that are likely to have isolated SKS and SKKS phases (Fig. 5.2). For example, a shallow source 80°-90° away produces the SKS phase that is close to S and ScS. Such source also produces SKKS (polarized at CMB) that is close to S-diff that may contain polarization generated at the source; the S-diff may have been previously split by the source anisotropy. To ensure that the phases are indeed isolated, we analyze the waveforms with the tauP package (Crotwell et al., 1999) that marks them with theoretical phase arrivals based on the theoretical arrival times of the AK135 earth model (Kennett et al., 1995). We select only those waveforms in which SKS and SKKS theoretical arrivals are separated by at least 15 s from the arrivals of the other phases.

The magnitude range of events suitable for shear wave splitting calculations is limited for the following reasons. Events that are too large generate interfering coda, making it difficult to isolate the SKS and SKKS arrivals. Events that are too small do not release enough energy for clearly detectable SKS and SKKS phases and the results would become inaccurate. We start by considering events larger than magnitude 6.0. To identify suitable events, we determine the signal-to-noise ratio (SNR) for their records using the method of Earle and Shearer, 1994. The events are selected for our analysis if they result in the SNR larger than 3 for at least 10 stations.

These criteria result in 53 suitable events in the magnitude range 6.2-7.0 (Table 5.1). Such events, at the distances involved in this study, may be considered as point sources. Note that the suitable events provide us with limited azimuthal coverage (Fig. 5.4). The SNR for these events is quite good, as illustrated in Fig. 5.7.

We start with data recorded at 100 samples/s and downsample to 20 samples/s to reduce the processing time. Since the dominant SKS periods are 8-10 s, we use a Butterworth bandpass filter with corner frequencies of 0.02-0.2 Hz and 2 poles applied in 2 passes to the waveforms prior to the splitting analysis. The filtering is done to improve the SNR (Earle

and Shearer, 1994).

The data is corrected for the magnetic declination since the stations use the magnetic North for orientation. We use data from the World Magnetic Model (Maus et al., 2010). The average declination in Mexico is $\sim 5.4^\circ$ (Fig. 5.5). We use different magnetic declination angles ϵ for different seismic stations, as given by the World Magnetic Model. If E' and N' are the original waveform components obtained from a seismic station, then the corrected E and N components can be found as:

$$E = E' \cos\epsilon + N' \sin\epsilon, \tag{5.1}$$

$$N = -E' \sin\epsilon + N' \cos\epsilon. \tag{5.2}$$

Examples of the filtered waveforms from a teleseismic event with clearly visible SKS and SKKS phases are shown in Fig. 5.3. The phase arrivals are marked using the theoretical phase arrival times generated by the tauP package (Crotwell et al., 1999).

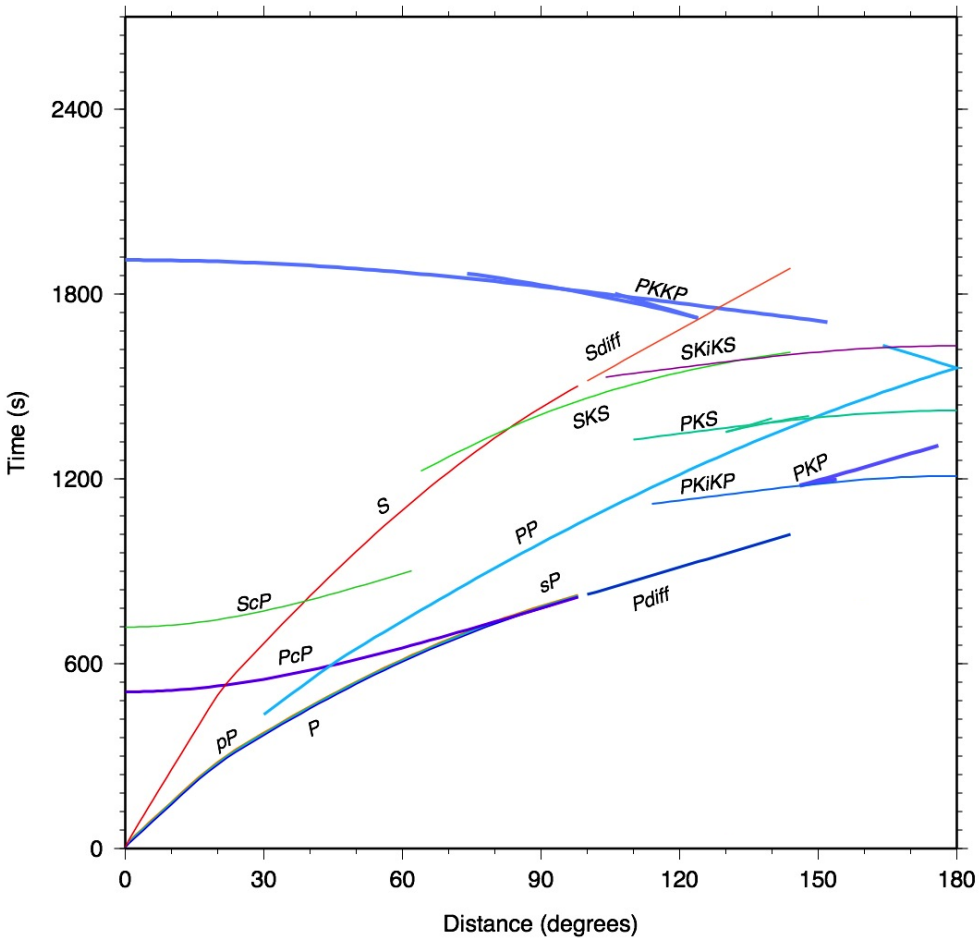

Figure 5.2: Theoretical phase arrivals for events at 10 km source depth from the IASPEI91 model. The SKS and SKKS are well separated and have a good signal-to-noise ratio between 90°-135°. The plot is adapted from Astiz et al., 2014.

#	yyyyMMddHHmmSS.ss	latitude	longitude	depth (km)	magnitude	Δ° to MIXC	baz (deg)
1	20070228231315.61	-55.24	-29.14	10	6.2	94.2	147.3
2	20050516035414.62	-32.59	-179.35	34	6.6	92.3	236.4
3	20060516103923.34	-31.81	-179.31	152	7.4	92.2	237.1
4	20050723085143.57	-30.25	-178.07	10	6.0	90.5	238.0
5	20051207233251.55	-30.01	-177.64	21	6.4	90.2	238.2
6	20050711230601.74	-27.00	-176.32	10	6.0	87.8	240.5
7	20071016210543.27	-25.77	179.53	509	6.6	90.8	243.1
8	20050116082504.47	-25.53	-176.30	16	6.2	87.2	241.9
9	20071005071752.81	-25.19	179.46	509	6.5	90.6	243.6
10	20060226030827.81	-23.61	-179.99	535	6.4	89.6	244.9
11	20050811090846.81	-22.68	169.51	10	6.2	98.4	249.0
12	20050330174157.16	-22.46	-179.75	588	6.1	89.0	245.9
13	20050319173446.18	-21.89	-179.55	598	6.3	88.6	246.3
14	20070727144626.88	-21.46	170.94	10	6.1	96.8	249.7
15	20070928010149.18	-21.21	169.36	12	6.3	98.1	250.4
16	20060815235346.77	-21.19	-176.25	154	6.1	85.5	245.8
17	20071119005212.51	-21.18	-178.75	558	6.3	87.7	246.7
18	20070927195744.00	-21.10	169.28	9	6.1	98.2	250.6
19	20050809052617.53	-20.94	173.82	23	6.1	94.1	249.4
20	20060602073136.46	-20.84	-178.70	591	6.0	87.5	247.0
21	20070404110027.94	-20.72	168.83	13	6.2	98.4	251.0
22	20060102221340.49	-19.93	-178.18	582	7.2	86.7	247.7
23	20050806095613.54	-19.61	-175.85	205	6.0	85.5	247.3
24	20061003180313.43	-18.84	169.00	161	6.3	97.7	252.8
25	20060224141545.21	-18.00	-179.59	622	6.1	87.2	250.0
26	20060202124843.44	-17.75	-178.39	597	6.7	86.1	250.0
27	20060609055827.77	-17.53	-178.75	564	6.1	86.3	250.1
28	20060807221855.09	-15.80	167.79	150	6.8	97.9	256.1
29	20070715092734.48	-15.38	168.60	8	6.1	85.3	252.1
30	20070425133414.23	-14.28	166.86	55	6.4	98.3	257.8
31	20050208144821.97	-14.25	167.26	206	6.7	97.9	257.7
32	20070902010518.15	-11.61	165.76	35	7.2	98.5	260.7
33	20071127114958.01	-10.95	162.15	16	6.6	101.7	262.4
34	20070816083928.44	-9.83	159.46	15	6.5	103.8	264.3
35	20070402120223.34	-8.71	157.62	14	6.2	105.2	266.0
36	20050122203017.35	-7.73	159.48	29	6.4	103.2	266.4
37	20050302104212.23	-6.53	129.93	201	7.1	130.6	278.2
38	20060218155922.09	-5.19	152.05	44	6.2	109.4	271.3
39	20050215144225.85	4.76	126.42	39	6.5	129.1	293.4
40	20050205122318.94	5.29	123.34	525	7.1	131.5	296.0
41	20071031033015.96	18.90	145.39	207	7.2	106.1	297.1
42	20061226122621.14	21.80	120.55	10	7.1	123.6	314.5
43	20070928133857.88	22.01	142.67	260	7.5	106.9	301.2
44	20050119061136.40	34.06	141.49	27	6.6	101.5	312.4
45	20051019114442.79	36.40	140.84	32	6.3	100.7	314.7
46	20070716141737.34	36.81	134.85	350	6.8	104.4	317.9
47	20051202131309.52	38.09	142.12	29	6.5	98.9	315.5
48	20050816024628.40	38.28	142.04	36	7.2	98.9	315.7
49	20050830181045.46	38.48	143.18	21	6.1	98.0	315.4
50	20050118140906.22	42.95	144.87	42	6.3	94.6	318.5
51	20060930175023.05	46.35	153.17	11	6.6	87.7	318.7
52	20051015100617.01	46.82	154.11	42	6.1	86.9	318.8
53	20070802023742.38	47.12	141.80	5	6.2	94.1	323.2

Table 5.1: 53 events used for the SKS/SKKS splitting listed by latitude.

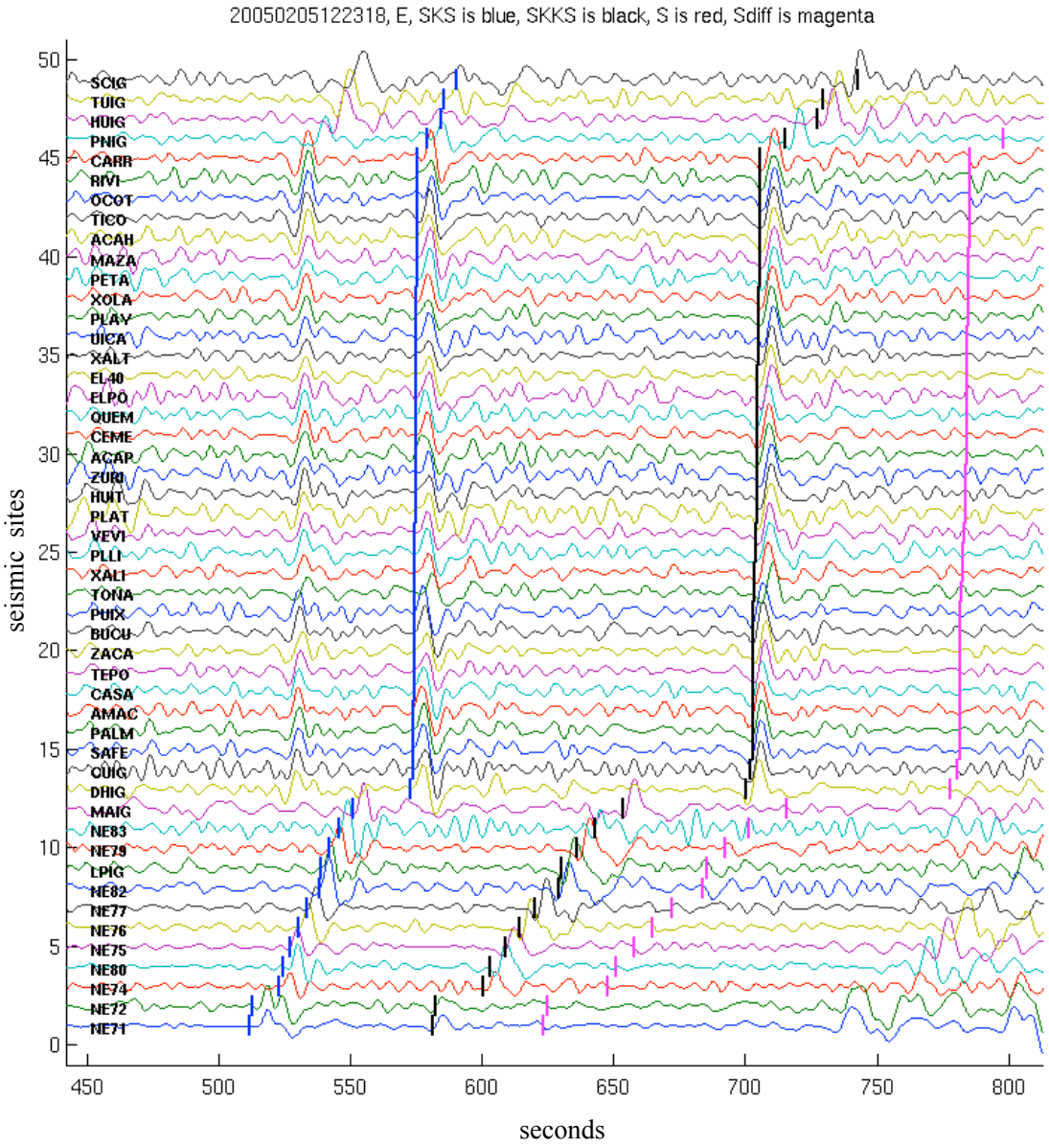

Figure 5.3: The SKS, SKKS, and Sdiff phases (with the arrivals marked in blue, black, and magenta, respectively) for event #40 (Table 5.1). The waveforms are sorted by the great-circle-path distance between the event and the stations.

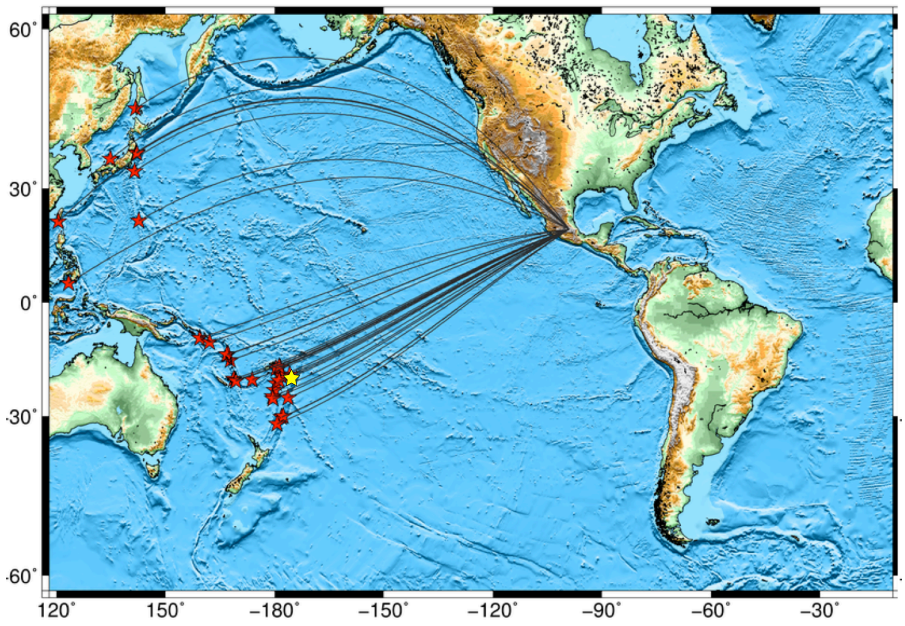

Figure 5.4: Locations of the best 32 events, M>6.0, $90° < \Delta < 135°$. The event marked with the yellow star (#20 (Table 5.1) is used for examples later in the text.

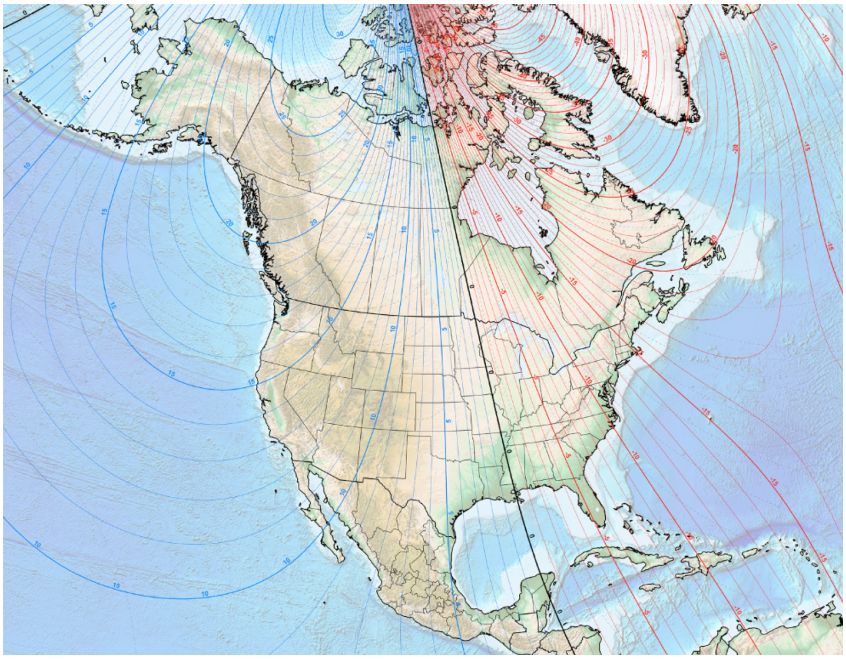

Figure 5.5: Magnetic declinations (Maus et al., 2010), positive in blue, negative in red.

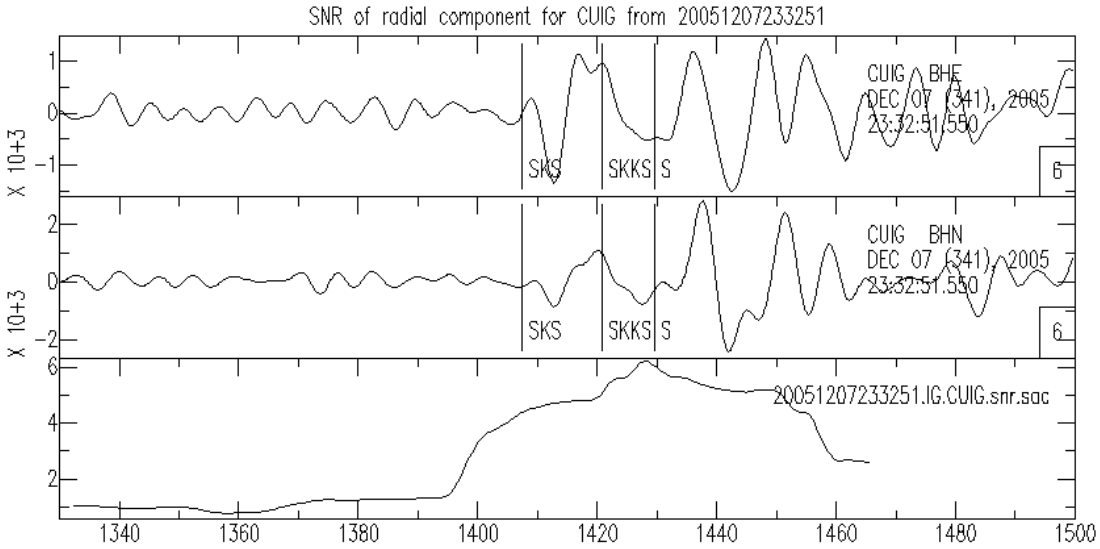

Figure 5.6: Example of the signal-to-noise ratio (SNR) computation. The E and N components of a waveform (top and middle panels) are used to compute the radial (R) and transverse (T) components. The SNR of the radial component (bottom panel) is computed using the method of Earle and Shearer, 1994. The SNR of 4-6 during the phases of interest indicates that the waveform is of high quality.

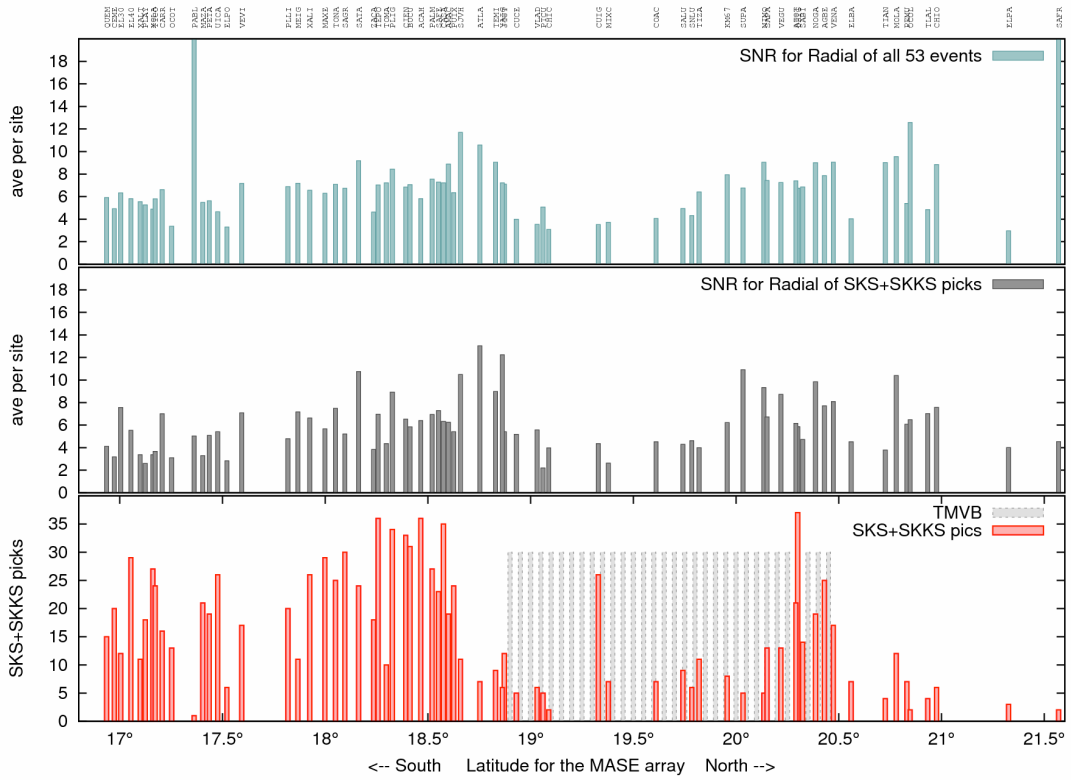

Figure 5.7: Signal-to-noise ratio of the best 53 events used for the shear-wave splitting calculations.

5.3 Methods

Our goal is to find, for each station location, the angle ϕ that characterizes the fast direction and the delay Δt that characterizes the strength of anisotropy. We apply the method of Silver and Chan, 1991 together with the waveform stacking of Davis, 2009. To improve the quality of our solution, we use not only single-event data at each station, but also data concatenations (also called stacks) from multiple events at the same station as well as data stacks for three nearby stations. As our results show, the stacking greatly improves the estimates of the shear wave splitting parameters, allowing us to obtain more robust results

compared to the averaging of the splitting parameters from individual events.

Our notation for different directions, components, and angles is given in Table 5.2 and illustrated in Fig. 5.8. The calculations involve transformations of the East (E) and North (N) displacement components into the transverse (T) and radial (R) ones as well as into slow (S) and fast (F), which are accomplished by rotations through the angles θ and ϕ, respectively:

$$T = E\cos\theta + N\sin\theta = \Re(\mathbf{W}e^{-i\theta}), \tag{5.3}$$

$$R = -E\sin\theta + N\cos\theta = \Im(\mathbf{W}e^{-i\theta}), \tag{5.4}$$

$$S = E\cos\phi + N\sin\phi = \Re(\mathbf{W}e^{-i\phi}), \tag{5.5}$$

$$F = -E\sin\phi + N\cos\phi = \Im(\mathbf{W}e^{-i\phi}), \tag{5.6}$$

where

$$\mathbf{W} = E + iN. \tag{5.7}$$

Notation	Meaning
E	East direction, corrected for the magnetic declination
N	North direction, corrected for the magnetic declination
R	Radial direction, points from an earthquake to a station
T	Transverse direction, perpendicular to **R**
S	Slow direction
F	Fast direction
E	East component, corrected for the magnetic declination
N	North component, corrected for the magnetic declination
R	Radial component, along direction **R** that points from an earthquake to a station
T	Transverse component, along direction **T** perpendicular to **R**
S	Slow component
F	Fast component
z	Backazimuth (baz), angle between the **N** and **-R** measured clockwise
θ	Angle between **N** and **R** as well as **E** and **T** measured counterclockwise; $\theta = \pi - z$
φ	Angle between **N** and **F** and well as **E** and **S** measured counterclockwise.
α	Angle between **F** and **R**, **S** and **T** measured counterclockwise.

Table 5.2: Notation for directions, components, and angles used in the calculations.

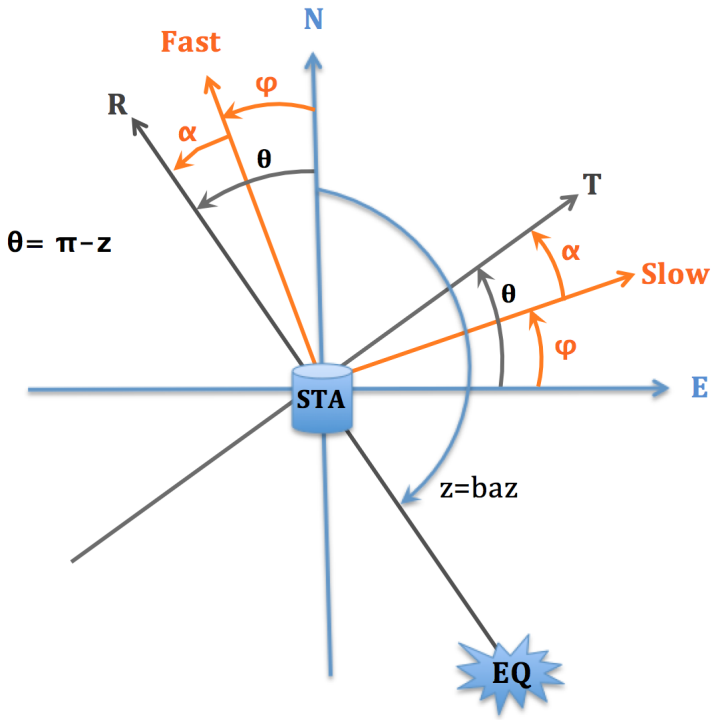

Figure 5.8: Directions and angles used in calculations.

To verify that a seismogram is suitable for shear wave splitting analysis, we compare its T component with the time derivative R' of its R component (Fig. 5.9). If T and R' are in phase, this suggests the presence of anisotropy (Vinnik et al., 1992) unobstructed by wave propagation complications such as reflections and refractions. We then choose for further processing the parts of the seismogram for which T and R' are in phase, separately for the SKS and SKKS phases. Note that each seismogram can result in either a suitable SKS window, or a SKKS window, or both. Next, we concatenate the identified windows either for one event at one station, or for multiple events at one station, or for multiple events at three stations, depending on the chosen approach as discussed further in section 5.4. The concatenation of the identified windows is done separately for the E and N components, resulting in two concatenated waveforms, which we call "E and N components" in the following discussion.

To find the anisotropy-characterizing parameters ϕ and Δt, we look for their values that allow us to "reverse" the effects of the anisotropy, following the method of Silver and Chan, 1991. Given the correct angle ϕ, one can transform the E and N components into the S and F components. If the S component is advanced by the correct Δt - negating the effect of the anisotropy - and then combined with the F component, the resulting seismogram should have no anisotropy effects, which means that only its R component is nonzero, and its T component is zero. This consideration suggests that one should look for values of ϕ and Δt that turn this corrected T component, which we denote by $\tilde{T}$, into zero. However, in reality, even in the absence of anisotropy, one would expect some signal in the T component, at least due to noise. So, instead, one considers the problem of minimizing the energy of $\tilde{T}$.

In other words, we find ϕ and Δt by minimizing the function:

$$\Sigma_T(\phi, \Delta t) = \int_{t_1}^{t_2} \tilde{T}^2(\phi, \Delta t; t)\, \mathrm{d}t, \tag{5.8}$$

where t_1 and t_2 are the ends of our concatenated waveforms. The corrected transverse component $\tilde{T}(\phi, \Delta t; t)$ as a function of ϕ and Δt is constructed by (i) rotating components

$E(t)$ and $N(t)$ by angle ϕ to compute the trial slow and fast components $S(\phi;t)$ and $F(\phi;t)$, (ii) advancing the slow component by Δt to get $\tilde{S}(\phi,\Delta t;t) = S(\phi;t+\Delta t)$, and (iii) computing the "corrected" transverse component $\tilde{T}(\phi,\Delta t;t)$ of the waveform given by $\tilde{S}(\phi,\Delta t;t)$ and $F(\phi;t)$. An example of the "corrected" transverse energy $\Sigma_T(\phi,\Delta t)$ for a range of ϕ and Δt is given in Figure 5.10. One can see a clear area of near-zero values (dark blue).

The initial guesses for the minimization procedure are $\phi = 120°$ and $\Delta t = 1.5$ s, for all cases, since the anisotropy does not vary significantly throughout our study area. These values are chosen based on initial trial-and-error runs. As Figure 5.10 shows, this is a reasonable initial guess. The value of the minimum for the case shown in the Figure is $\phi = 147°$ and $\Delta t = 1.3$ s. Selecting a good initial guess is important for fast convergence.

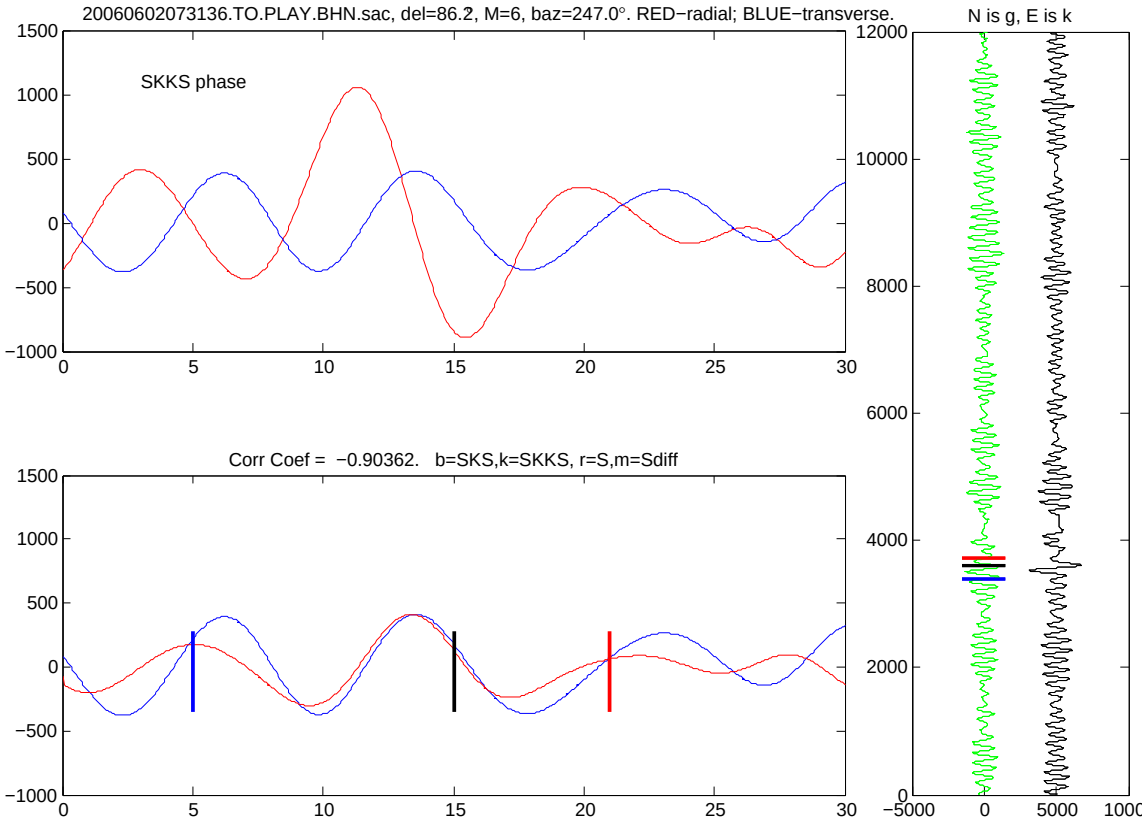

Figure 5.9: Example of a waveform with the SKKS phase suitable for our analysis. Top: R (red) and T (blue) components for station PLAY from the MASE array for event #20 (Table 5.1). The event is marked by a yellow star in Fig. 5.4. The horizontal axis gives time in MATLAB points, one point is equal to 5 s; the vertical axis is the amplitude. Bottom: Comparison between R' (red) and T (blue). Theoretical arrival times for SKS, SKKS, and Sdiff phases are marked by vertical blue, black, and red bars, respectively. R' and T are in phase within the 8-17 time window around the predicted SKKS arrival, which means that this is a waveform with a clear SKKS split. We select the 8-17 time window for further processing to find the splitting parameters. Note that the R and T are out of phase in the same window, as expected. Right: N (green) and E (black) components with the theoretical phase arrivals marked by the same colors.

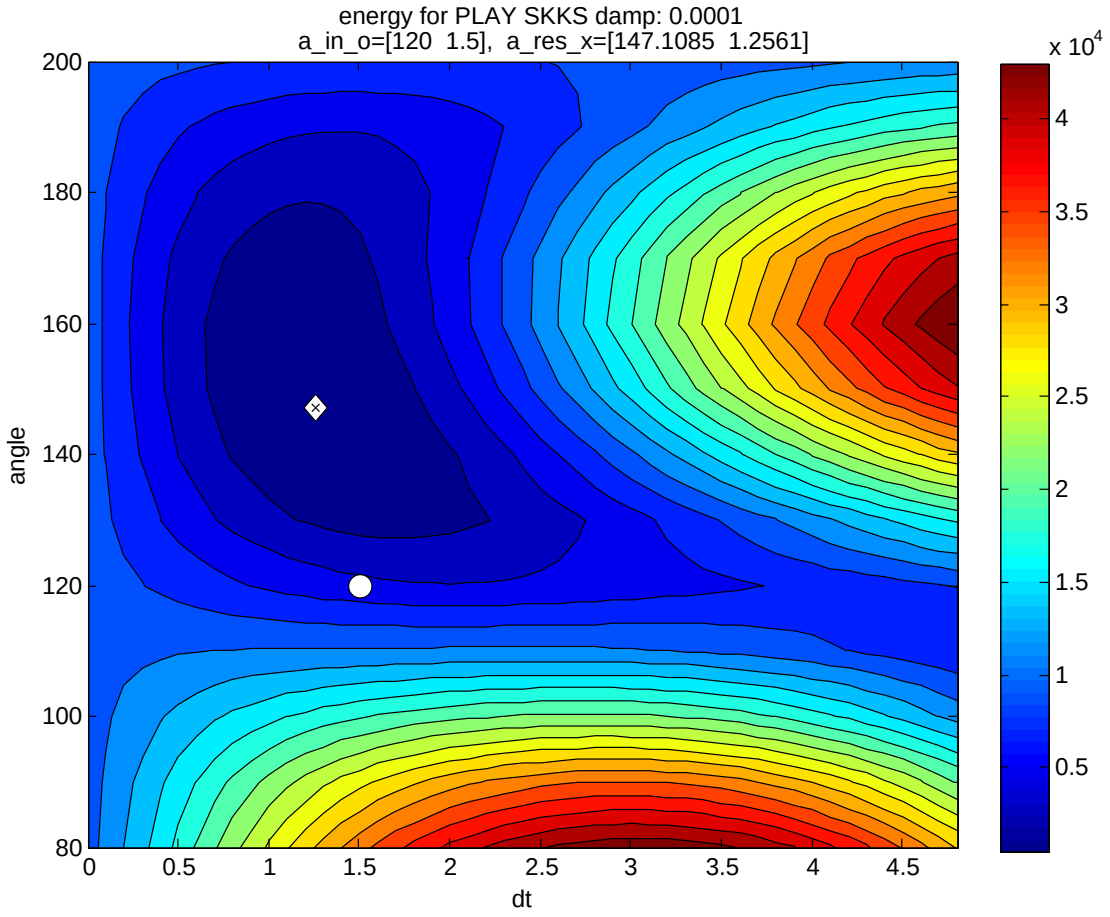

Figure 5.10: Energy of the corrected transverse component, $\tilde{T}$, for the one-event SKKS data shown in Fig. 5.9 as a function of ϕ and Δt. The minimum of the energy gives the splitting parameters, which are $\phi = 147°$ and $\Delta t = 1.3$ s in this case (marked by a white diamond with a cross). The initial value used for the minimization is the same for all approaches and stations in this study and it is given by $\phi = 120°$ and $\Delta t = 1.5$ s (marked by a white circle).

5.4 Approaches with different levels of data stacking, their validation and results

We start by obtaining the anisotropy using one event at each station. Then we show how the splitting results improve for approaches with stacking (Wolfe and Silver, 1998; Davis, 2009) the SKS and SKKS phases from different events as well as with our newly developed three-station stacking approach.

5.4.1 One-station single-event approach

As the first step, we find the shear wave splitting parameters using one event at each station, and then compare our results to the ones obtained by SplitLab (Wustefeld et al., 2008). An example of waveforms we analyze for station PLAY of the MASE array is given in Fig. 5.9. As discussed in section 5.3, we select for processing the window close to the theoretical arrivals of either SKS or SKKS components in which the R' and T are in phase. For example, for the waveform of Fig. 5.9, we identify a clear in-phase window close to the SKKS theoretical arrival. Next, we find the splitting parameters by minimizing the energy (5.8) of the corrected $\tilde{T}$ component within the identified window; the results for the waveform of Fig. 5.9 are $\phi = 147^\circ$ and $\Delta t = 1.3$ s, as shown in Fig. 5.10.

Note that we have developed an efficient procedure for storing the information about suitable SKS and SKKS time windows. For each waveform, the selections are done only once, and the beginning and end of the selected windows are saved in the waveform header. The header is written in the Seismic Analysis Code (SAC) (Goldstein et al., 2003), with several places for user-defined variables, and enables automated use of the saved data. This approach allows us to process the selected windows repeatedly, e.g., for different approaches and stacking procedures, without repeating the effort-intensive selection process.

To validate our solution procedure, we compare the results with those obtained by Split-

Lab (Fig. 5.11). We find that the results are quite similar: $\phi = 145°$ and $\Delta t = 1.5$ s for SplitLab and $\phi = 147°$ and $\Delta t = 1.3$ s for our method. This similarity gives us confidence in our solution procedures.

For a given station, the results of the single-event approach obtained using different events are broadly similar but not identical. This is illustrated in Fig. 5.12 that shows the splitting parameters for several stations based on two events. Averaging the results for these and other events is not straightforward, because the differences appear both in angle ϕ and time delay Δt. Because the time delay is linked to its direction, a simple averaging of angles and time delays separately would not produce physically meaningful quantities. That is why we turn to waveform stacking, as described in the following sections, to determine ϕ and Δt that provide the best fit for a number of instances of wave splitting in many events. We also concatenate SKS and SKKS windows together to improve our results. This is because both phases come from the core-mantle boundary along nearly the same paths with wide Fresnel zones (Fig. 5.1) and hence should reflect the same anisotropy. This is confirmed by a separate analysis for SKS and SKKS phases for a single event at each station (Figure 5.12), which shows similar results for the two phases.

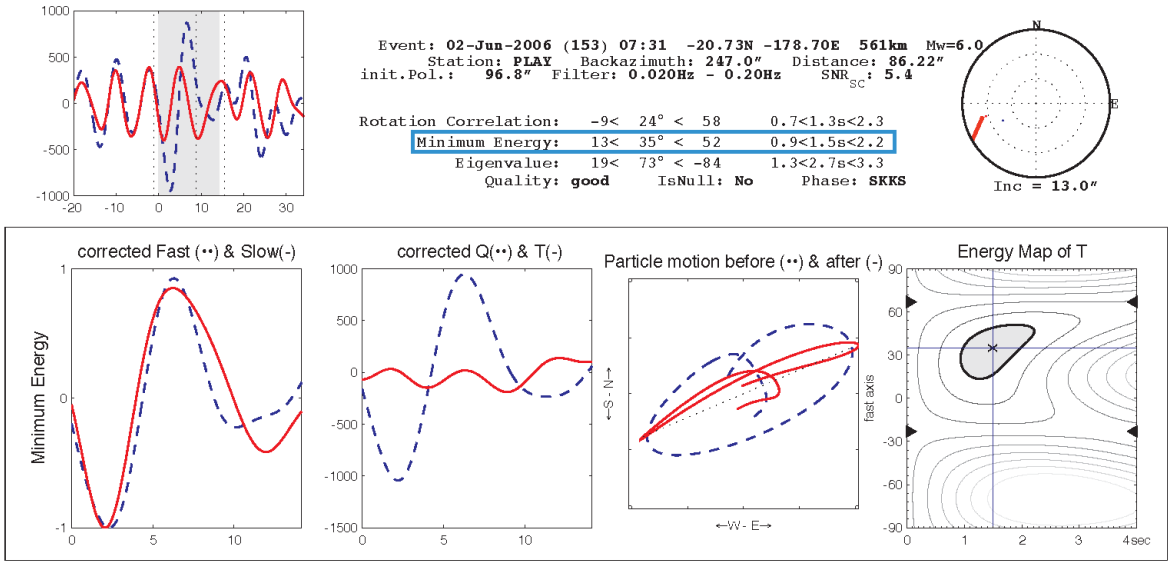

Figure 5.11: Splitting results for the one-event SKKS data shown in Fig. 5.9 produced by the SplitLab code (Wustefeld et al., 2008). The SplitLab values of $\phi = 145°$ and $\Delta t = 1.5$ s are quite similar to the $\phi = 147°$ and $\Delta t = 1.3$ s obtained by our method (Fig. 5.10). Note that the fast angle ϕ' in SplitLab is positive clockwise and hence $\phi = \pi - \phi'$. SplitLab plots the particle motion (the third panel at the bottom), and the corrected motion (red) is nearly flat, with mostly radial and minimized transverse component, as one would expect. The energy map of the corrected T (bottom right) is also similar to ours.

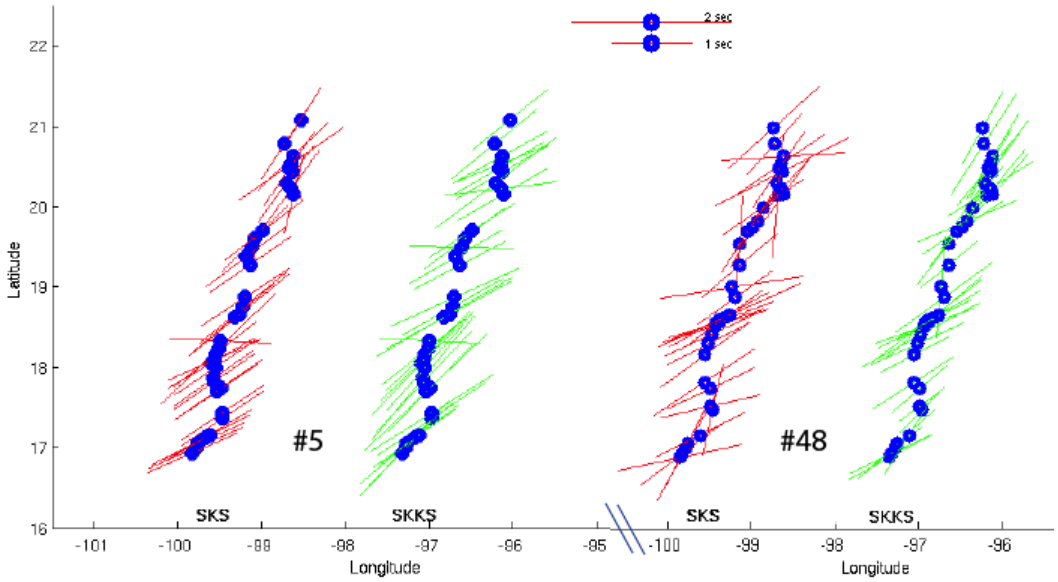

Figure 5.12: Shear wave splitting results for SKS (red) and SKKS (green) phases using events #5 (left) and #48 (right) (Table 5.1) for all MASE stations for which these events result in suitable windows. The SKKS results are shifted in longitude for clarity. At each station, the inclination of the line gives the fast direction angle ϕ. The length of the line reflects the time delay Δt. The two events produce broadly similar results. Note that the results for the two phases are also similar for a given event. This is expected since the Fresnel zones for both phases often overlap or are close to each other, thus sampling similar volume (Fig. 5.1).

5.4.2 One-station multiple-event stacking approach

To obtain more robust estimates, we stack (i.e., concatenate) at each station all identified SKS and SKKS windows from multiple events. A part of a stacked waveform containing three phases is illustrated in Fig. 5.13; the full stacked wave form typically has 5-30 phases (Fig. 5.14). An example of how the stacking modifies the energy and minimum of the corrected $\tilde{T}$ is shown in Fig. 5.15 (to be compared with Fig. 5.10) for the MASE station PLAY. The one-event shear wave splitting parameters of $\phi = 147°$ and $\Delta t = 1.3$ change to $\phi = 130°$ and

$\Delta t = 1.6$ for this case, which uses the stacking of phases from 13 events.

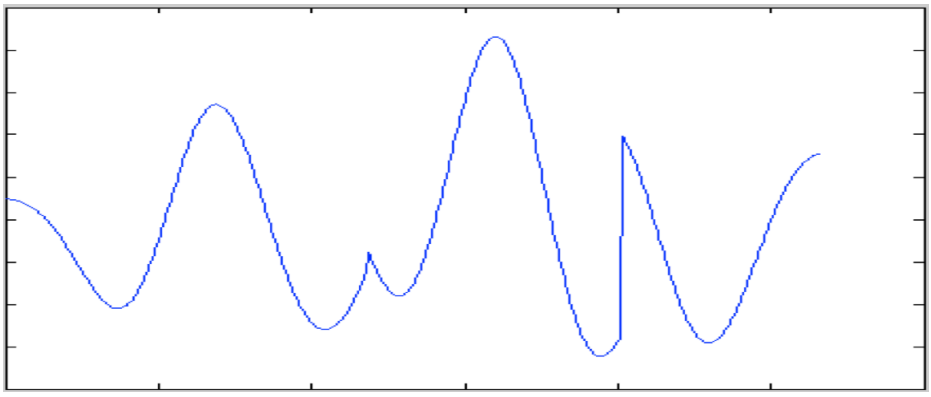

Figure 5.13: An example of a stack (concatenation) of three SKS and SKKS phase windows picked from two events for the same station (MASE station PLAY).

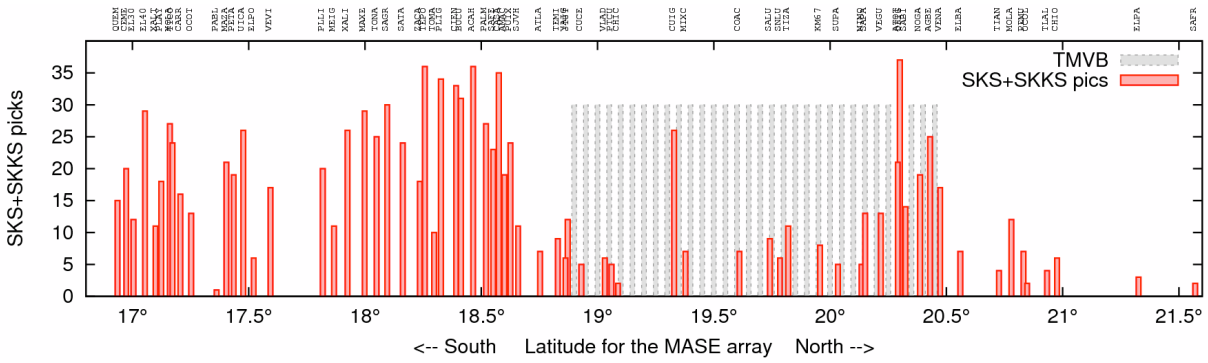

Figure 5.14: The number of the SKS and SKKS picks for the MASE sites.

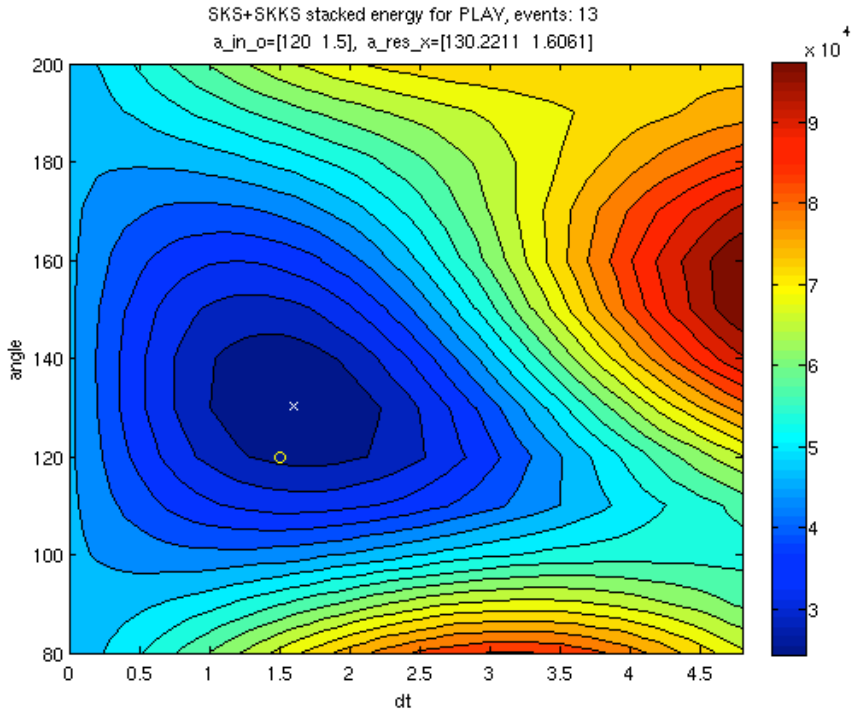

Figure 5.15: Energy of the corrected transverse component, $\tilde{T}$, for the SKS and SKKS stacked waveforms from 13 events for the MASE site PLAY as a function of ϕ and Δt. The minimum of the energy gives the splitting parameters, which are $\phi = 130°$ and $\Delta t = 1.6$ s in this case (marked by a cross). The initial value used for the minimization is the same for all approaches and stations in this study and it is given by $\phi = 120°$ and $\Delta t = 1.5$ s (marked by a white circle).

To validate our one-station multiple-event approach and compare its results with published findings, we perform the SKS analysis for Baja California (Fig. 5.16). The obtained results are similar to the shear wave splitting results of van Benthem et al., 2008 who used data collected over a different time period. In both set of results, the fast direction is broadly aligned with the absolute plate motion. This finding will be further discussed in section 5.5.

The shear wave splitting parameters for the stations of the MASE array obtained by

the one-station multiple-event approach are shown in Fig. 5.17 (blue thin line). The fast angle ϕ varies mostly between 120° and 150° degrees; the time delay Δt is mostly between 0.5 and 2 s. The values at nearby stations, spaced only by 5 km on average, occasionally show relatively abrupt variations. This issue is further discussed in the next section, which introduces the three-station stacking approach and reconsiders the results for the MASE array. In our final shear wave splitting results for Mexico, presented in section 5.5, the one-station multiple-event method is used for the permanent SSN stations in Mexico that are well-separated from each other (with distances of the order of 100 km).

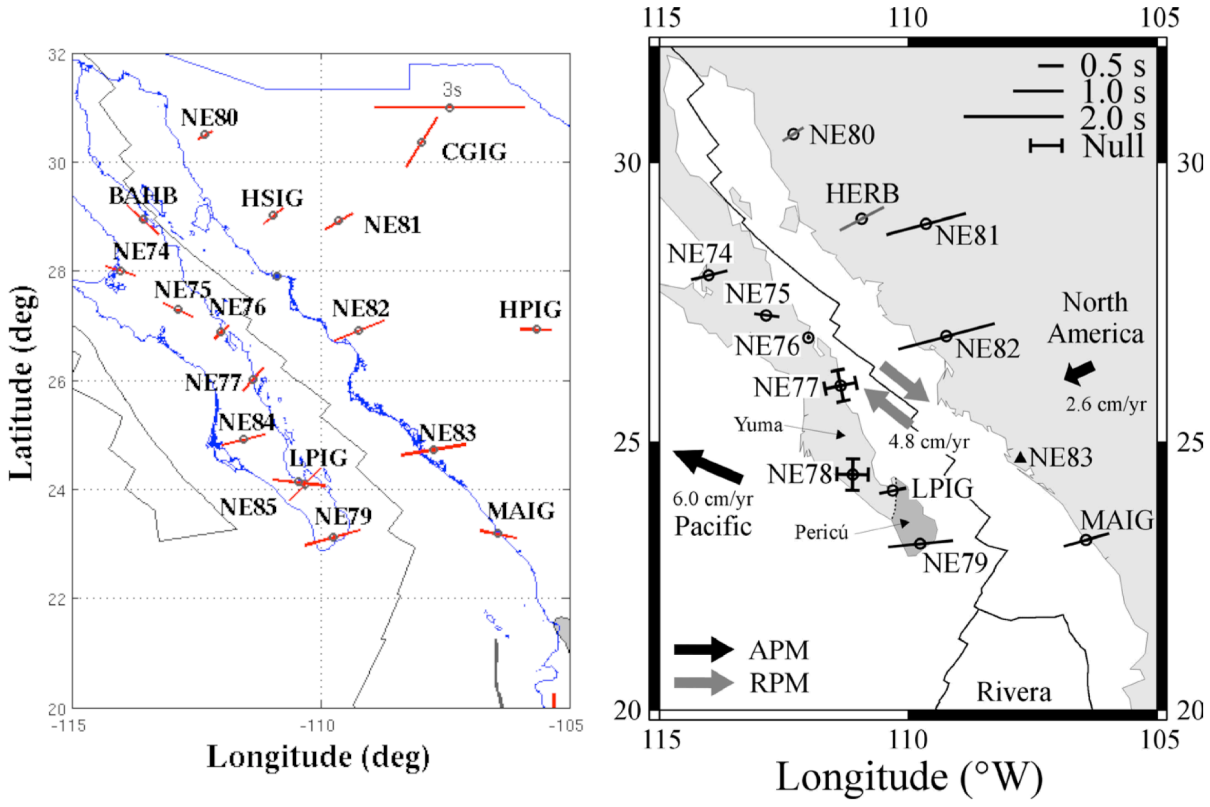

Figure 5.16: (Left) Shear-wave splitting results for Baja California of the one-station multiple-event stacking approach of this work. (Right) Shear-wave splitting results for the same area from van Benthem et al., 2008. The two sets of results are quite similar.

Figure 5.17: Fast angle ϕ (top) and time delay Δt (bottom) for the MASE stations obtained with the one-station multiple-event approach (thin blue line) and three-station multiple-event approach (think grey line). The stations are identified by their number, with the southmost stations being #1. The vertical red line indicates the south edge of the Trans-Mexican volcanic belt (TMVB), which corresponds to station #39.

5.4.3 Three-station multiple-event stacking approach

The shear wave splitting parameters obtained by the one-station multiple-event method for the MASE array (Fig. 5.17) occasionally exhibit relatively large variations from one

station to the next. For example, the fast direction varies from less than 120° for station #16 to more than 150° for station #17, over a distance of about 5 km. As discussed in more details later, the delay times of 1 to 1.5 s for those stations are much larger than the ones obtained with the surface waves in chapter 4, suggesting the origin for the anisotropy uncovered by the shear wave splitting is deeper than 200 km. Given this deeper origin, the Fresnel zones of waveforms at the nearby stations should significantly overlap, making rapid changes in the shear splitting parameters unphysical. As already mentioned, averaging the fast angle and the time delay separately is not physically meaningful.

Hence, to determine more robust parameter estimates, we employ a sliding three-station stacking for the dense MASE array. For each station, excluding the first and last ones, its shear wave slitting parameters are determined by stacking all identified SKS and SKKS windows for that station as well as its two neighbors. The results of this approach are given in Fig. 5.17 (dark grey line). Both parameters vary more smoothly in this approach, as expected.

5.5 Shear-wave splitting results for Mexico and their interpretation

The shear wave splitting results for Mexico are shown in Fig. 5.18. One clear observation is that the fast directions for the MASE stations, as well as the stations to the east of the MASE array, are nearly identical and coincide with the absolute plate motion (Fig. 5.19). These stations also have similar delay times, of 1-2.0 s. To the west of the MASE array, the overall results are similar, although there is more variability.

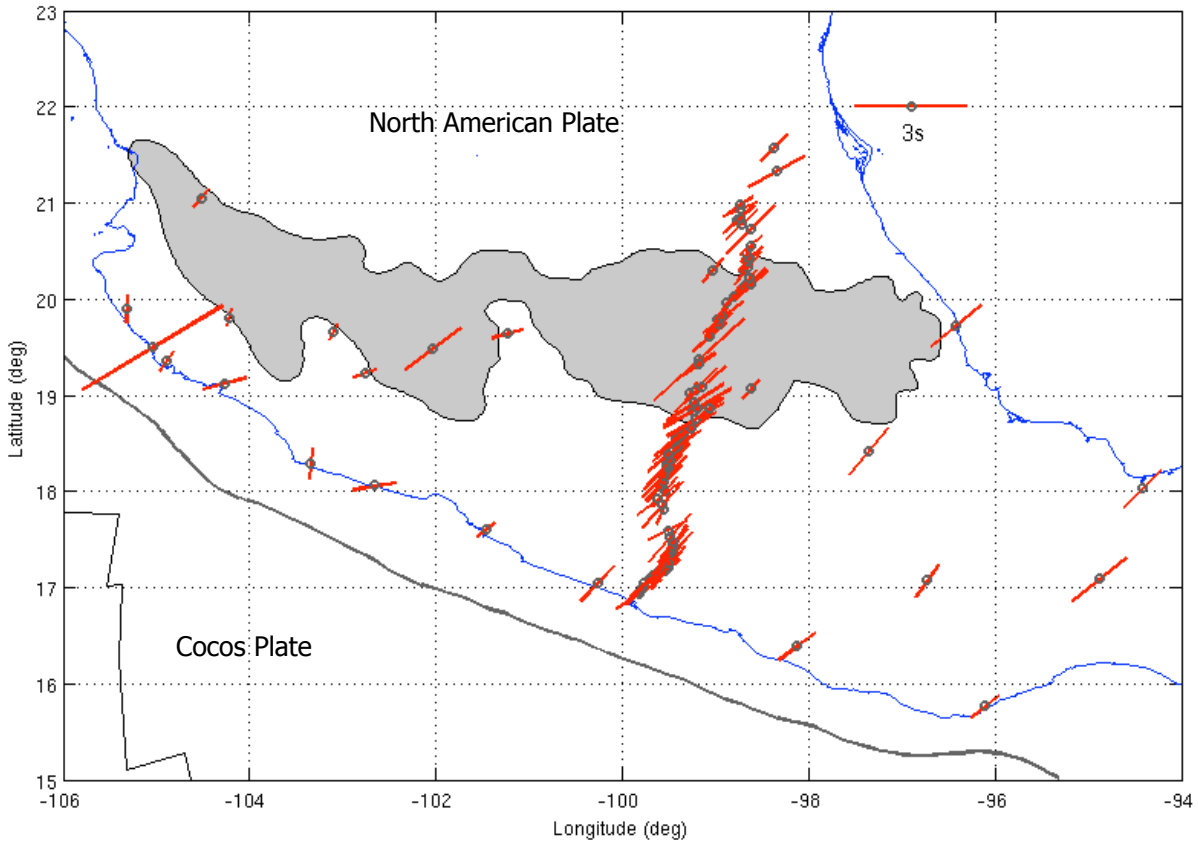

Figure 5.18: Shear-wave splitting results for Mexico. The slope of the red lines indicates the fast angle ϕ while the length of the lines reflects the delay time Δt. The values for the MASE stations are obtained using the three-station multiple-event approach; the one-station approach is used for the rest of the stations.

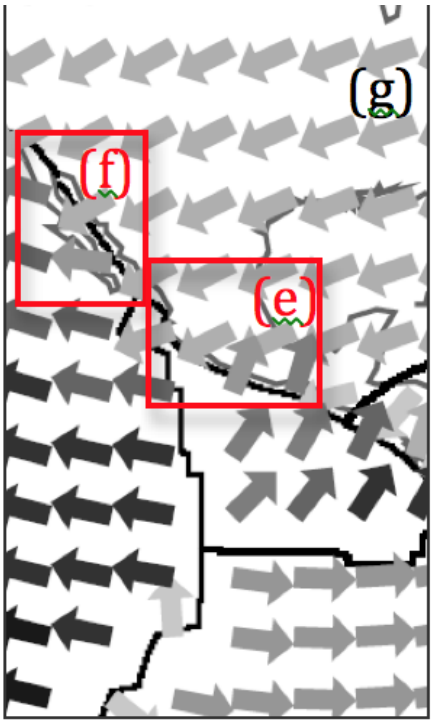

Figure 5.19: Absolute plate motion (APM) vectors (DeMets et al., 1994). The area of the shear wave splitting analysis in mainland Mexico is marked by a red rectangle and letter (e), Baja California is marked by (f). The absolute plate motion coincides with the shear-wave splitting fast directions for Mexico (Fig. 5.18).

Another clear observation is that the anisotropy parameters determined from our shear wave splitting analysis are quite different from those based on the surface wave inversion results of Chapter 4 (Fig. 5.20, red vs black lines), both in terms of the fast direction and the time delay. Here we use layer 3 from the surface wave results for comparison. At the location of the MASE array, the fast directions are nearly orthogonal to each other. The time delay is significantly longer for the shear wave splitting, by about a factor of three. The anisotropy based on the surface wave results varies with depth (Fig. 4.1); however, the comparison with all three layers of the surface wave results indicates similarly substantial differences. Note that the anisotropy amplitude in the surface wave results of Chapter 4 is

expressed as a percentage of the shear wave speeds; this amplitude is interpreted here in terms of the predicted shear wave splitting delay Δt. The 1% of 2ψ surface wave anisotropy corresponds to approximately 0.3 s of shear wave splitting Δt .

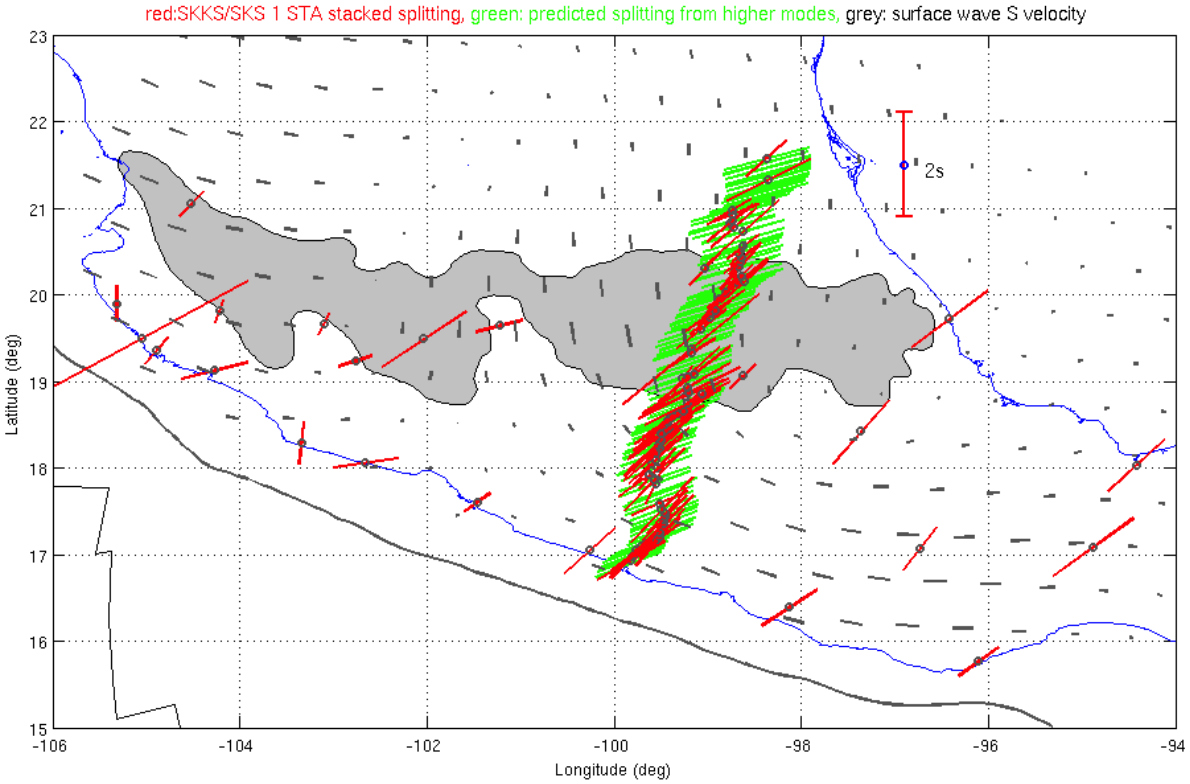

Figure 5.20: Comparison of the shear-wave splitting parameters based on our SKS and SKKS analysis, surface wave results from chapter 4 (Fig. 4.1, panel C), and the predicted splitting from the surface wave higher modes (Yuan and Beghein, 2013). The surface wave results for the top 200 km is significantly different from the shear-wave splitting parameters, indicating that the anisotropy captured by the shear wave splitting occurs deeper than 200 km. The similarity in ϕ and Δt between our shear wave splitting analysis and the higher mode study of Yuan and Beghein, 2013 supports the deep origin of the splitting.

The significant difference of the anisotropy in the upper 200 km, as detected by the surface

wave analysis, and the average anisotropy between the CMB and the surface, as resolved by the shear wave splitting, implies that the shear wave splitting results are dominated by a structure deeper than 200 km. Since the time delays are significantly longer for the shear wave splitting results, the deeper structure is either much larger than 200 km, or has stronger anisotropy, or both. The deeper origin of the anisotropy from the shear wave splitting analysis is supported by the favorable comparison of our results with the predicted values based on higher surface wave modes for 0-1400 km depth (Yuan and Beghein, 2013).

While the anisotropy based on the shear wave splitting and surface wave analyses differs significantly, as already pointed out, closer examination of the shear wave splitting results reveal potential influences of the shallow structure and its deeper extensions.

First, the shear wave splitting results for the MASE array, shown in more detail in Fig. 5.17, reveal a change (dip) in the fast direction around the southern edge of the TMVB, which is located above the transition from the flat to steep subduction. This fast direction change is associated with the beginning of the decreasing trend in the delay times, which continues towards the eastern end of the MASE array. These variations in the anisotropy parameters may reflect the change in the shear direction due to the flow induced by the steeply subducting and retracting slab; the slab has been imaged down to 540 km depth (Fig. 1.2). The waveforms for the stations with the decreasing delay-time trend have paths that cross the steeply subducting slab and the surrounding slab-parallel flow (Fig. 5.21). Around the steeply subducting slab, the fast direction is likely to be parallel to the slab, and hence the projection of the corresponding delay times onto the horizontal (i.e., earth-surface-parallel) plane imaged in this study should lead to the decrease of the delay times, as observed.

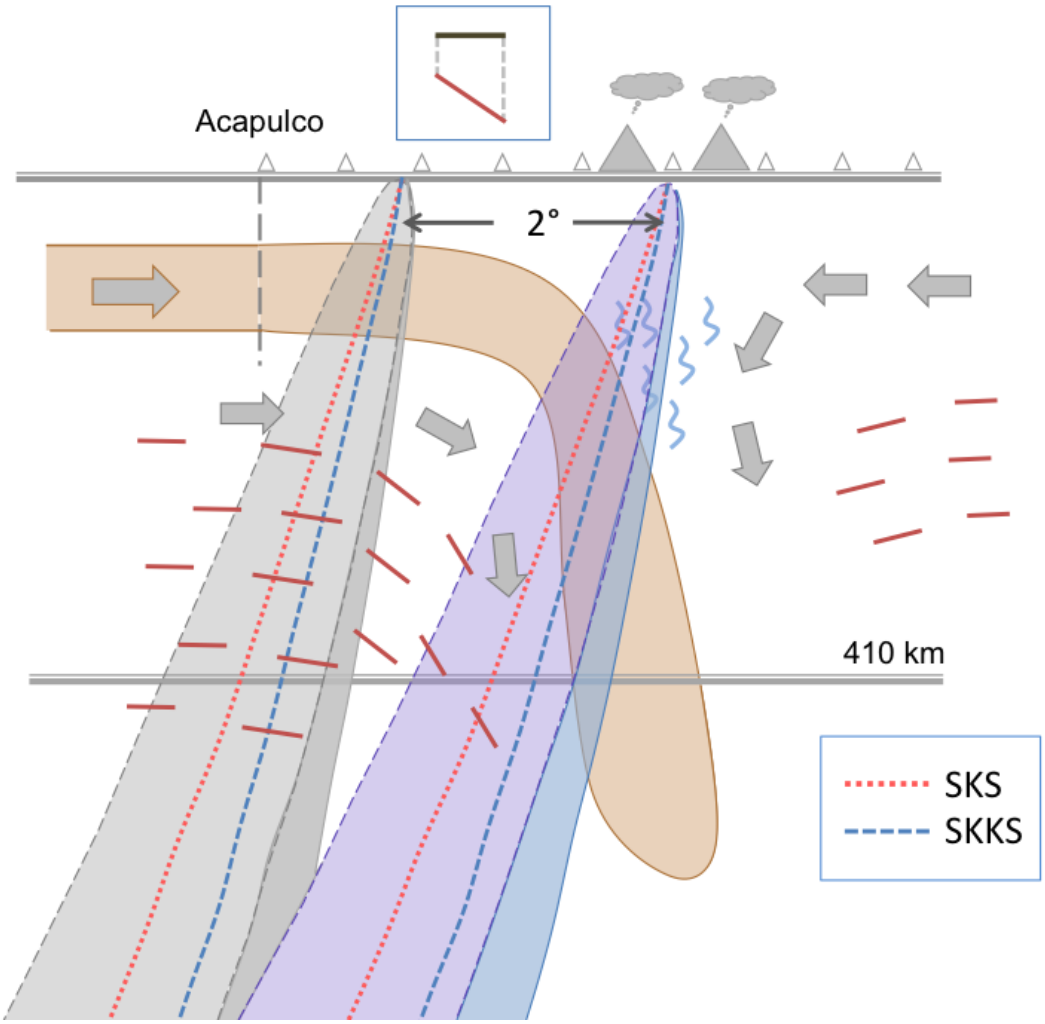

Figure 5.21: The waveforms for the stations with the decreasing delay-time trend have paths that cross the steeply subducting slab and the surrounding slab-parallel flow. Insert: projection of the splitting onto the horizontal axes. The Fresnel zones for SKS and SKKS phases from the same event to the MASE stations 2° apart like in the Fig. 5.22.

Second, the pattern of fast directions and delay times west of the MASE array (Fig. 5.18) is somewhat more complex, with variations in both ϕ and Δt. This coincides with the presence of two smaller subducting slabs, with gaps, inferred from the surface wave analysis of Chapter 4 (Fig. 4.2). The shear wave splitting results in this area are likely affected by

the slabs and the flow they create.

The shear wave splitting results for the MASE array (Fig. 5.18) show remarkable similarity for stations south of the TMVB (station #1-30). These stations cover the distance of approximately 2°. The Fresnel zones for the SKS and SKKS phases arriving at stations 2° apart are schematically illustrated in Fig. 5.22. If the similarity of the shear wave splitting results is attributed to the common volume that such zones cover, then the origin of the observed anisotropy would be deeper than $\approx$ 600 km. However, even though the Fresnel zones do not intersect much in the shallower regions, one cannot exclude a presence of a near-horizontal structure of uniform anisotropy at the depths somewhere between 200 and 600 km. To provide more constraints on the origin depth of the observed shear wave splitting, we develop the higher mode analysis described in the next Chapter.

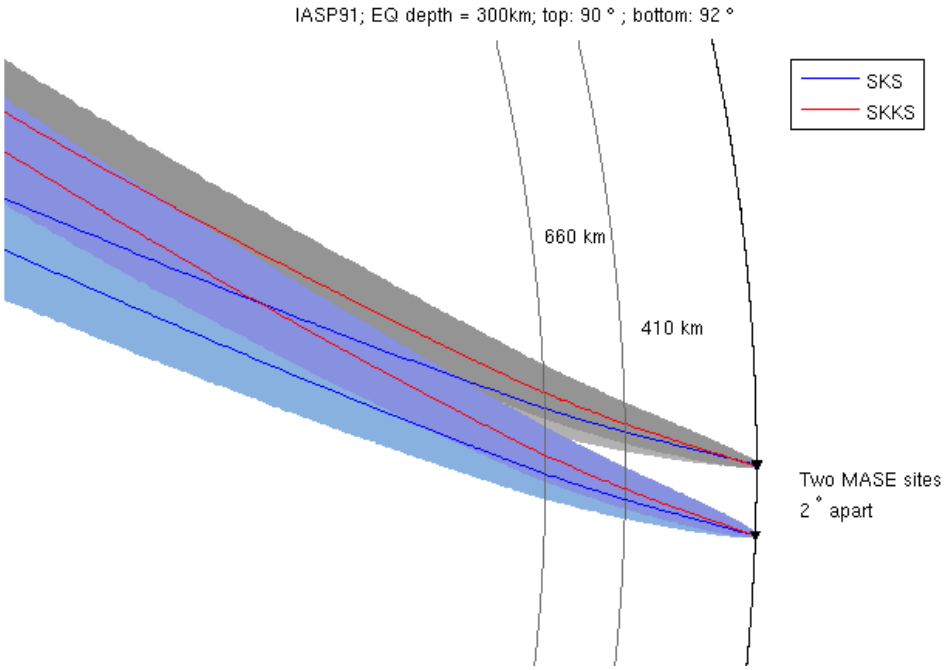

Figure 5.22: Fresnel zones for SKS and SKKS phases from one event for two sites 2° apart. The Fresnel zone diameter for the period of 8 s, which is the mean value for the SKS and SKKS periods, is approximately 230 km at the 400-km depth (Alsina and Snieder, 1995).

CHAPTER 6

Anisotropy calculation methods based on spheroidal modes

6.1 Introduction

To constrain the depth of the anisotropy identified by our shear wave splitting analysis, we use spheroidal higher modes, since their overtones at different periods are sensitive to different depths (Fig. 1.3). Normal modes create a complete basis for surface displacements of the Earth, which means that any displacement can be expressed as a linear combination of the normal modes, with several first terms containing most of the signal (Montagner and Roult, 2008; Dahlen and Tromp, 1998).

In order to characterize the anisotropy, we determine the propagation velocities of the several first overtones along the fast and slow directions (as obtained by the shear wave splitting analysis, Fig. 6.1) in the region of interest. The final objective is to interpret the obtained velocities, with the following basic premise: if an overtone has higher velocities along the fast direction (or lower velocities along the slow direction), this would indicate that anisotropy may be occurring at the depths to which this particular overtone is sensitive. In contrast, if a particular overtone has lower velocities along the fast direction, then the depths that this overtone samples are likely not contributing to the anisotropy identified by the shear wave splitting results.

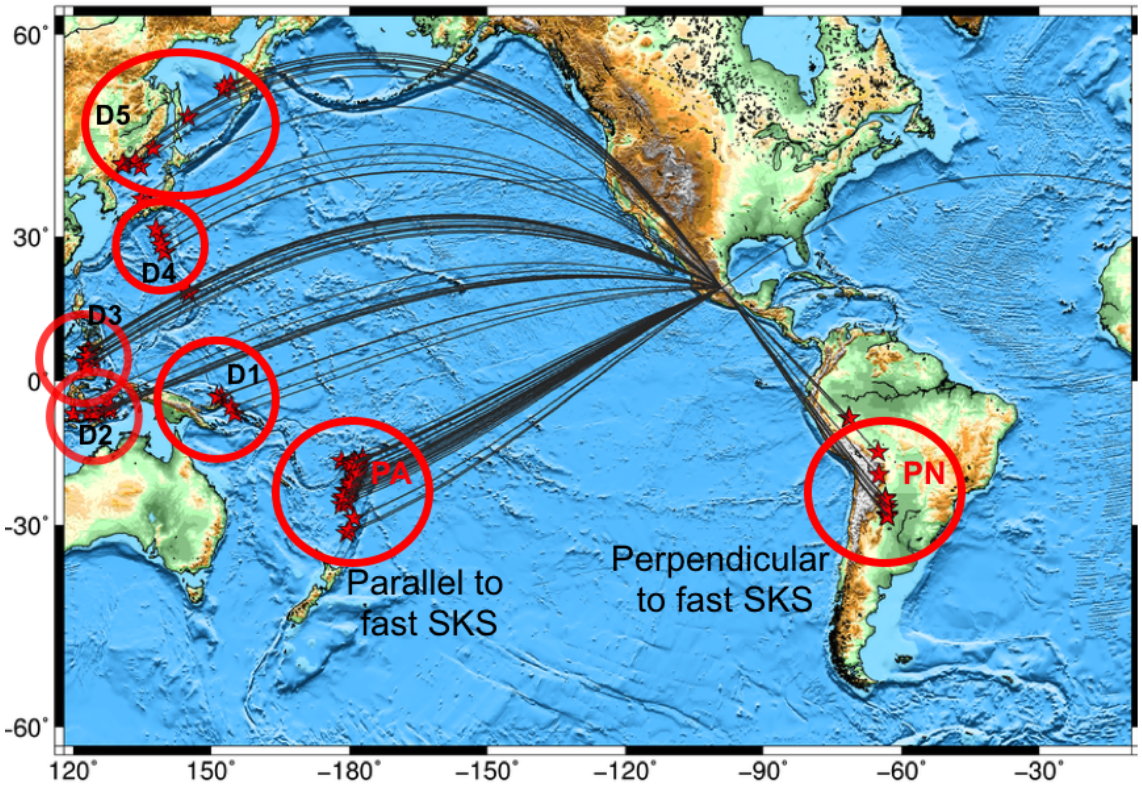

Figure 6.1: Representative event locations with epicenter depths at 365-676 km.

6.2 Data

The data was collected by stations from four networks: the temporary dense MASE array that was installed by the UCLA and Caltech during 2005-2007 (TO), USArray Transportable Array from the NSF EarthScope Project (TA), the permanent sites from the Mexican Servicio Sismologico Nacional during 2005-2013 (IG), and the United States National Seismic Network (US). For the events, we select deep (> 300 km) and strong (>M 6.0) earthquakes with waves approaching Mexico from parallel to perpendicular to the fast SKS anisotropic directions (Fig. 6.1). The events are intentionally chosen to be deep to minimize the amplitude of the Rayleigh fundamental mode. There are 96 deep events between 2005 and 2013 that

are selected under those conditions. 54 of them can be separated into 7 clusters based on their location, as shown in Fig. 6.1 and Table 6.1. Having clusters is important, since we utilize the stacking technique to improve the results. Based on a good signal-to-noise ratio (found separately for filtered and unfiltered data), we use 42 of these events in our analysis. To reduce the processing time, we downsample the 90 min long waveforms from 10 to 1 sample/s. Prior to the higher mode analysis, we use a Butterworth bandpass filter with corner frequencies of 0.008-0.04 Hz and 2 poles applied in 2 passes to the waveforms.

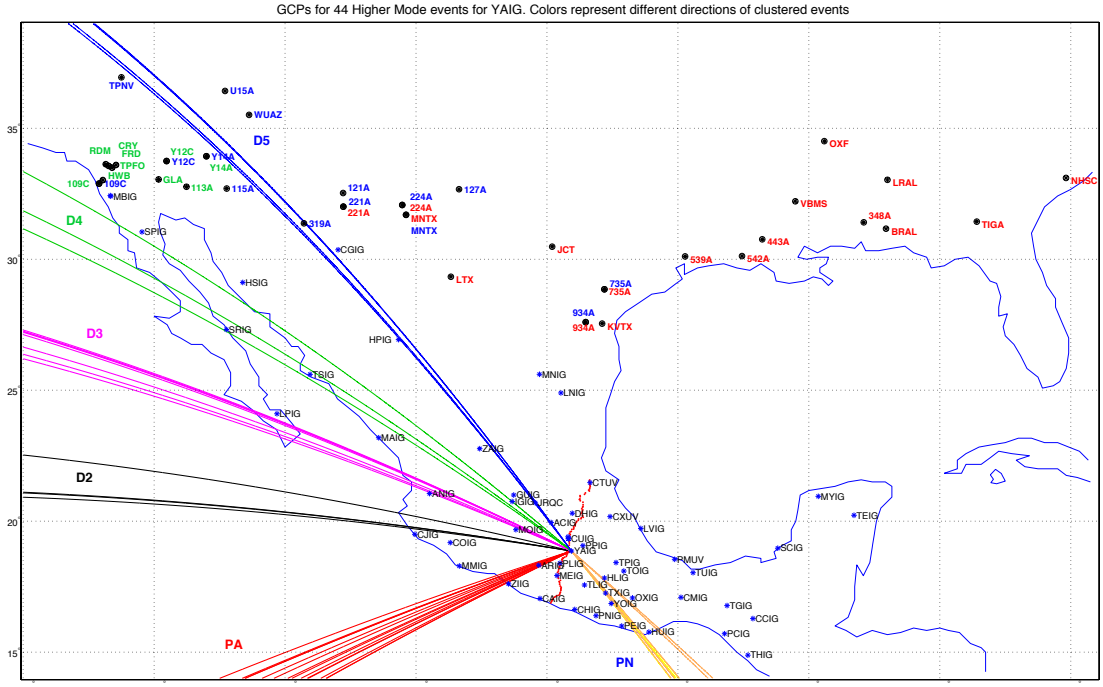

Figure 6.2: The seismic site locations in Mexico and USA from four different networks (TO, IG, TA, and US) used for the higher mode velocity computations. The rays of different colors marked as PN, PA, D2, D3, D4, and D5 show the great circle paths from the events to the site YAIG.

#	yyyyMMddHHmmSS.ss	latitude	longitude	depth (km)	magnitude	event	Δ° to CAIG	baz (deg)	
1	20071016210543.20	-25.78	179.53	509	6.6	Ev67	88.8	242.7	direction PA
2	20110915193104.00	-21.61	-179.53	645	7.3	Ev18	86.6	246.3	
3	20060102221340.40	-19.93	-178.18	583	7.2	Ev89	84.8	247.5	
4	20091109104455.10	-17.24	178.33	595	7.3	Ev49	87.1	251.1	
5	20060202124843.40	-17.75	-178.39	598	6.7	Ev87	84.3	249.6	
6	20110403140709.30	-17.64	-178.59	552	6.4	Ev23	84.4	249.8	
7	20110221105752.40	-26.14	178.39	558	6.5	Ev25	89.9	242.7	
8	20071005071752.80	-25.19	179.46	509	6.5	Ev68	88.7	243.3	
9	20110729074222.60	-23.78	179.76	523	6.7	Ev22	87.9	244.5	
10	20060226030827.80	-23.61	-179.99	535	6.4	Ev85	87.7	244.6	
11	20100630043102.10	-23.31	179.12	581	6.4	Ev39	88.4	245.2	
12	20070506211152.50	-19.40	-179.35	676	6.5	Ev73	85.7	248.3	
13	20091122074820.60	-17.79	-178.43	523	6.4	Ev48	84.3	249.6	
14	20080115175215.60	-21.98	-179.54	598	6.5	Ev65	86.7	246.0	
15	20061113012635.80	-26.05	-63.28	572	6.8	Ev79	55.9	139.2	direction PN
16	20050321122354.00	-24.98	-63.47	579	6.9	Ev94	55.1	138.5	
17	20110902134709.60	-28.40	-63.03	579	6.7	Ev19	57.8	140.9	
18	20120528050723.40	-28.04	-63.09	587	6.7	Ev11	57.5	140.7	
19	20110101095658.10	-26.80	-63.14	577	7.0	Ev30	56.6	139.7	
20	20080903112514.40	-26.74	-63.23	570	6.3	Ev58	56.5	139.7	
21	20050321124312.30	-24.73	-63.51	570	6.4	Ev93	54.8	138.3	
22	20111122184816.30	-15.36	-65.09	550	6.6	Ev16	47.3	130.9	
23	20100524161829.00	-8.09	-71.56	581	6.5	Ev40	37.8	129.1	
24	20070421071248.00	-3.55	151.27	407	6.1	Ev74	109.6	273.2	D1
25	20100320140049.90	-3.36	152.25	415	6.6	Ev42	108.6	273.0	
26	20110207195342.90	-7.15	155.18	415	6.4	Ev28	107.0	268.3	
27	20110310170836.80	-6.87	116.72	511	6.5	Ev24	142.5	281.1	direction D2
28	20060909041312.00	-7.22	120.11	572	6.3	Ev81	139.4	278.9	
29	20090828015120.40	-7.15	123.43	642	6.9	Ev53	136.2	277.5	
30	20081206105526.30	-7.39	124.75	398	6.4	Ev54	135.1	276.7	
31	20110830065741.60	-6.36	126.75	470	6.9	Ev20	132.9	277.2	
32	20060127165853.60	-5.47	128.13	397	7.6	Ev88	131.3	277.8	
33	20091007214113.20	4.08	122.37	574	6.8	Ev51	132.9	292.6	direction D3
34	20110210143927.70	4.20	122.97	523	6.5	Ev27	132.4	292.4	
35	20110210144158.80	4.08	123.04	525	6.6	Ev26	132.4	292.2	
36	20100729073156.20	6.55	123.22	618	6.6	Ev34	131.0	295.0	
37	20100723231510.10	6.78	123.26	641	7.5	Ev36	130.9	295.2	
38	20050205122318.90	5.29	123.34	525	7.1	Ev96	131.5	293.4	
39	20091004105800.10	6.74	123.38	620	6.6	Ev52	130.8	295.0	
40	20100723220811.20	6.72	123.41	607	7.3	Ev38	130.8	295.0	
41	20100723225111.80	6.50	123.48	578	7.6	Ev37	130.0	294.7	
42	20100724053501.00	6.22	123.52	553	6.6	Ev35	130.9	292.4	
43	20120101052755.90	31.46	138.07	365	6.8	Ev15	106.1	310.8	D4
44	20101130032440.10	28.35	139.19	470	6.8	Ev32	106.9	307.5	
45	20110112213253.80	26.97	139.88	512	6.4	Ev29	107.1	305.9	
46	20091224002331.70	42.25	134.72	392	6.3	Ev45	102.3	321.5	direction D5
47	20100218011319.50	42.59	130.70	578	6.9	Ev44	104.4	323.7	
48	20130405130002.10	42.71	131.11	562	6.3	Ev07	104.0	323.6	
49	20120814025938.40	49.80	145.06	583	7.7	Ev10	92.1	323.9	
50	20091210023052.60	53.42	152.76	656	6.3	Ev46	86.2	325.0	
51	20130524054449.60	53.42	152.76	609	8.3	Ev02	86.2	325.0	
52	20130524145631.80	53.42	152.76	623	6.7	Ev01	86.2	325.0	
53	20080705021204.40	53.88	152.89	633	7.7	Ev60	85.9	325.4	
54	20081124090258.70	54.20	154.32	492	7.3	Ev56	85.0	325.3	

Table 6.1: 54 clustered events selected for the higher mode analysis listed by the back azimuth (*baz*) directions marked in Fig. 6.1. The events in red are not used because of the poor data quality.

6.3 Higher mode separation technique

In order to identify and isolate the first several higher modes in our data, we use the synthetic seismograms generated by the MINEOS code package (Masters et al., 2014). MINEOS computes synthetic seismograms in a spherically symmetric non-rotating Earth by summing the normal modes. To isolate the higher modes in the data, we input information about our source events (locations and moment tensors), produce synthetic seismograms for the first five overtones, and compare their sum with the actual time series. We utilize only the vertical component in our analysis.

The waveforms (data and synthetics) are narrowly (10 s consecutive intervals) bandpass filtered in the range of 25-125 s, because the separation of the first five higher modes is the largest for these periods, as evident from the PREM higher mode dispersion curves (Fig. 6.3). In this frequency range, our tests on synthetic seismograms (up to the fifteenth overtone, n = 15) show that modes with n $\geq$ 5 have negligible amplitudes (Fig. 6.4). That is why, in our data processing, we assume that the first 5 modes can be isolated at a particular frequency. In general, it is difficult to separate the different overtone branches as their group velocities overlap over a wide range of frequencies.

Examples of our data are given in Figures 6.5 and 6.6; the vertical velocity component is shown. The event of magnitude 7.7 occurred at the depth of 632 km near the Sea of Okhotsk and approached Mexico from the NW side, perpendicular to the fast SKS directions (cluster D5). Since the synthetics are computed for radially symmetric, isotropic Earth, we expect to find time shifts between the synthetics and actual data. Indeed, a noticeable discrepancy is seen between the observed phase arrivals (bottom trace in Fig. 6.5) and the synthetic ones (second from the bottom waveform, cumulative from the fundamental through the fifth mode), caused by both anisotropy and lateral heterogeneity. Our goal is to find the time shifts, and hence the updated phase velocities, for the separate modes needed for the cumulative synthetic seismogram to match the data. The calculated phase velocities can

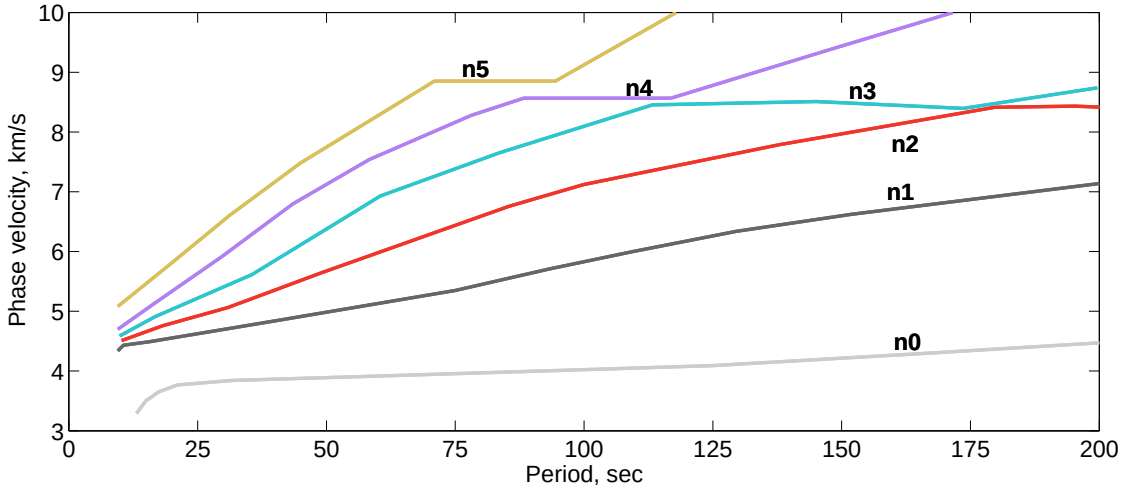

Figure 6.3: Rayleigh fundamental and higher mode dispersion curves for phase velocities. Adapted from Dahlen and Tromp, 1998.

then be interpreted in terms of anisotropy and its depth and strength.

The main difficulty in obtaining dispersion measurements from teleseismically observed surface waves at periods less than about 100 s is that variations in phase velocity are sufficiently large to cause path variations of several cycles in phase, and isolated residual phase measurements in the range $[-\pi, \pi]$ at a single period are therefore ambiguous in multiples of 2π. For minor arc observations, however, phase measurements at periods longer than 100 s can be associated with a total cycle count without difficulty. We window our data using predicted time arrivals based on the Hilbert transform envelopes of the synthetic higher mode waveforms to eliminate the cycle skipping problem around a particular phase arrival (Fig. 6.9, insert).

In order to remove the path effects outside the region of interest, the station closest to or farthest from the events is used as a reference, and its travel time is subtracted from the travel times of all other stations. The differences in travel times across Mexico are then used to determine the propagation velocity of each overtone and period.

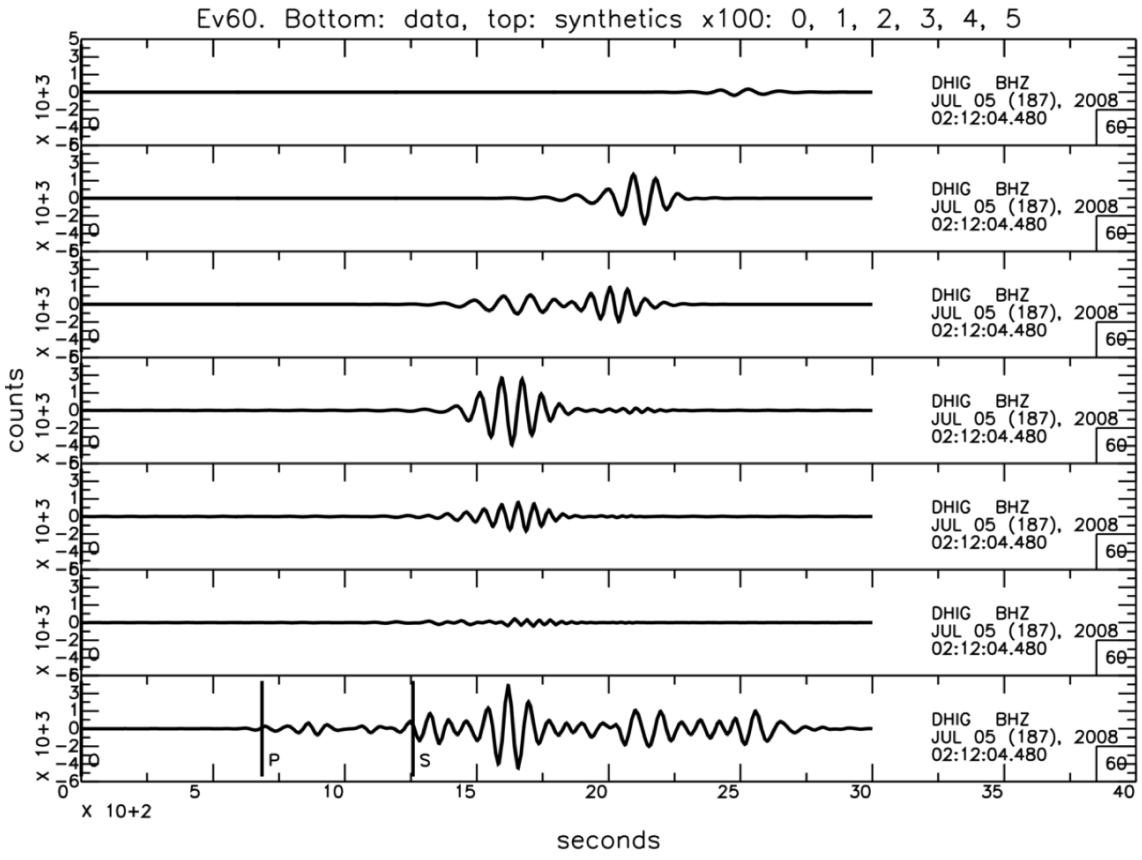

Figure 6.4: Synthetics and data for a deep (632 km) event near the Sea of Okhotsk for one station (DHIG). Synthetics of the fundamental (top, $n = 0$) and the first five overtone spheroidal-mode waveforms are shown, as well as the actual seismogram (bottom). The bandpass filter is between the periods of 66 and 125 sec.

For stable results for a given overtone, it is important to consider the periods that contain significant energy for that overtone, which we calculate based on the continuous wavelet transform. An example of how the energy depends on the period for a particular event is shown in Figures 6.7 and 6.8. For the first overtone (top panels), most of the energy is concentrated between periods of 40 and 150 s, for the second one - between 35 and 95 s, etc. In all cases, we are also limited by the broadband instrument response and the need to consider periods that allow for mode separation, which results in an additional constraint of

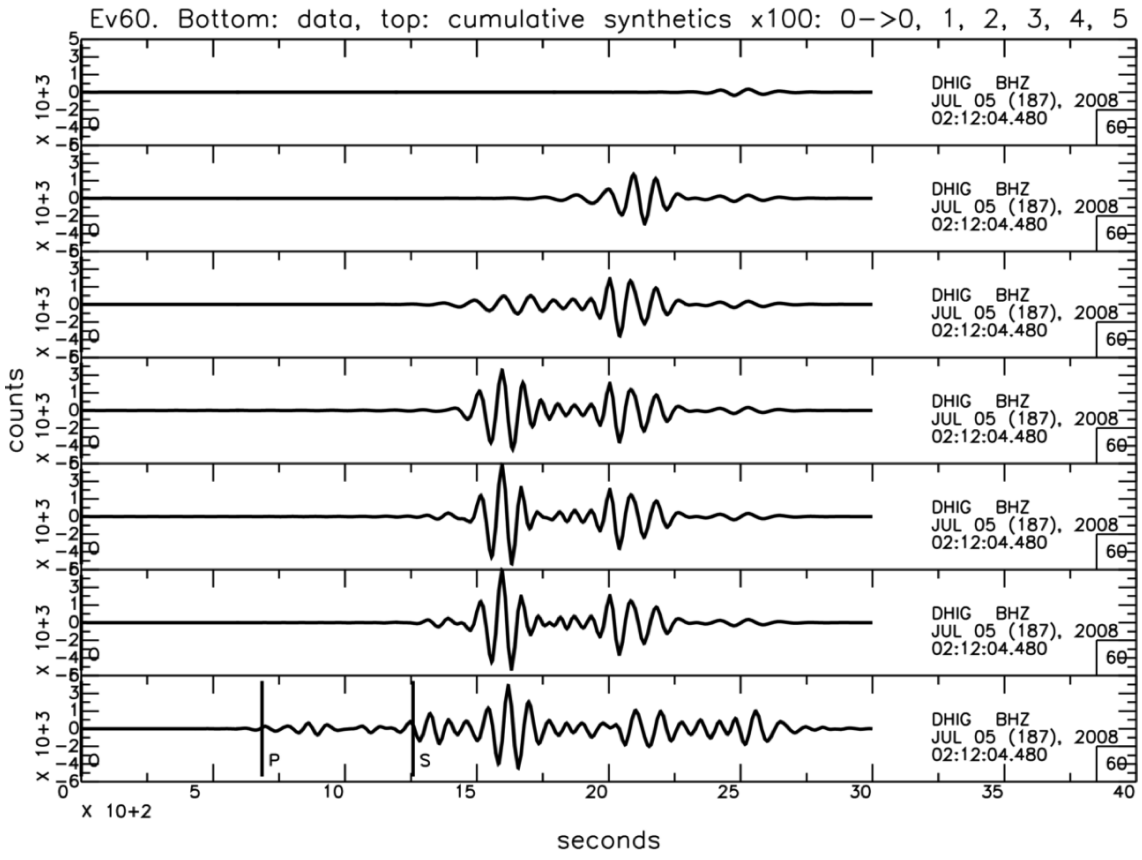

Figure 6.5: Cumulative effect of adding one mode at a time for the case of Fig. 6.4. The top trace shows only the fundamental mode ($n = 0$), the second trace shows the sum of the fundamental and first mode ($n = 0, n = 1$), etc.; the bottom trace gives the actual collected seismogram.

periods between 25 and 125 s, as already mentioned. Hence the range of periods we consider for the first overtone, for example, is 40 to 125 s. We divide this range into intervals of 10 s, i.e., we filter the data between 45 and 55 s, 55 and 65 s, etc, and assign the phase velocity computed for a given interval to the midpoint of that interval, i.e., to 50 s for the interval of 45 to 55 s. We find that significant energy is contained within similar period ranges for the events that occur in the same region and arrive from the same direction. Note that the higher overtones ($n = 4$, $n = 5$) have energy in the shorter period band and arrive sooner.

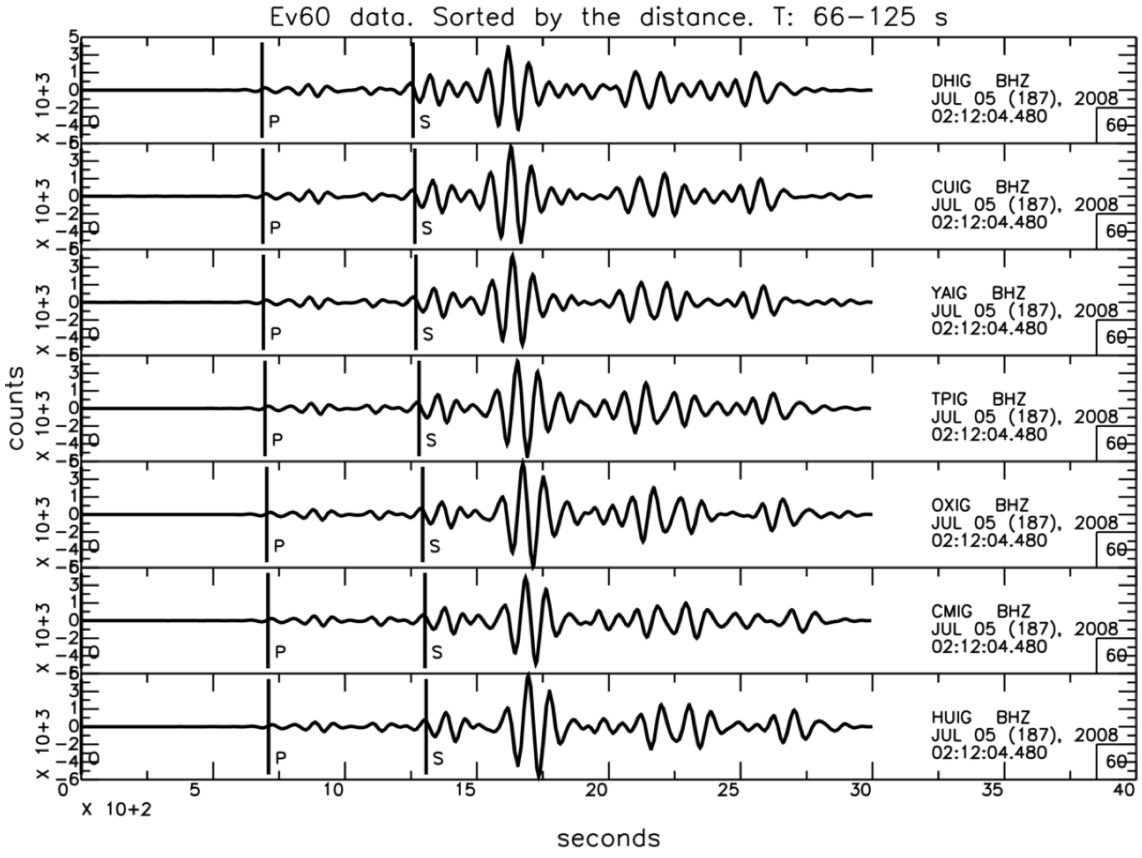

Figure 6.6: Comparison of seismograms for several sites for the event of Fig. 6.4 sorted by the distance from the earthquake. The traces are clearly similar, indicating similar contributions from various modes.

As in the shear wave splitting analysis, to obtain robust results, we stack (concatenate) all relevant data for each period interval and a given arrival direction. That is, we stack filtered waveforms for all events in a given cluster (and hence arriving from the same direction) and all stations. The resulting simultaneous analysis of all relevant data provides a convenient way of averaging between different events and stations as well as minimizes the effect of any potential outliers.

As mentioned earlier, our goal is to find how the PREM-based phase velocities v_n^{PREM} for modes $n = 0$, 1, ..., need to be modified for the cumulative synthetic seismogram to match

the data. The newly found phase velocities v_n can then be interpreted in terms of anisotropy and its depth. The fitting procedure is done iteratively using the nonlinear least-squares approach. That is, we minimize the least-squares difference ϕ between the filtered data and synthetic seismogram:

$$\phi = \sum_{i=1}^{N_s} (y_i - f_i)^2, \tag{6.1}$$

where y_i and f_i, $i = 1, 2, ..., N_s$, are the N_s points (or samples) along the actual and synthetic seismograms, respectively. The synthetic seismogram is computed as a sum of shifted waveforms M_n for modes $n = 0, 1, ..., N$:

$$f_i = A \sum_{n=0}^{N} M_{ni}(\Delta t + \delta x/v_n^{PREM} - \delta x/v_n), \tag{6.2}$$

where N is the number of the highest mode used ($N = 5$ in our study), M_{ni} is the ith sample of the synthetic waveform for mode n computed using PREM, Δt is a time offset, and δx is the distance from the reference station to the station under consideration. The time offset Δt is needed to account for the average phase difference between measurements at all stations and predictions by the PREM model. For example, if the ocean is slow relative to PREM, the offset will correct for that. Hence, for each direction (or event cluster), the fitting parameters are the phase velocities v_n for the fundamental and first five modes (e.g., $n = 0, 1, ..., 5$), amplitude A (the waveforms for all modes are scaled by the same amplitude), and time offset Δt. To solve the resulting non-linear least-squares problem, we use the Levenberg-Marquardt algorithm, also known as the damped least-squares method. Examples of the final fit between the data and sum of the shifted synthetic overtones for one station, event, and period range is given in Figure 6.9. One can see that the fit is quite good.

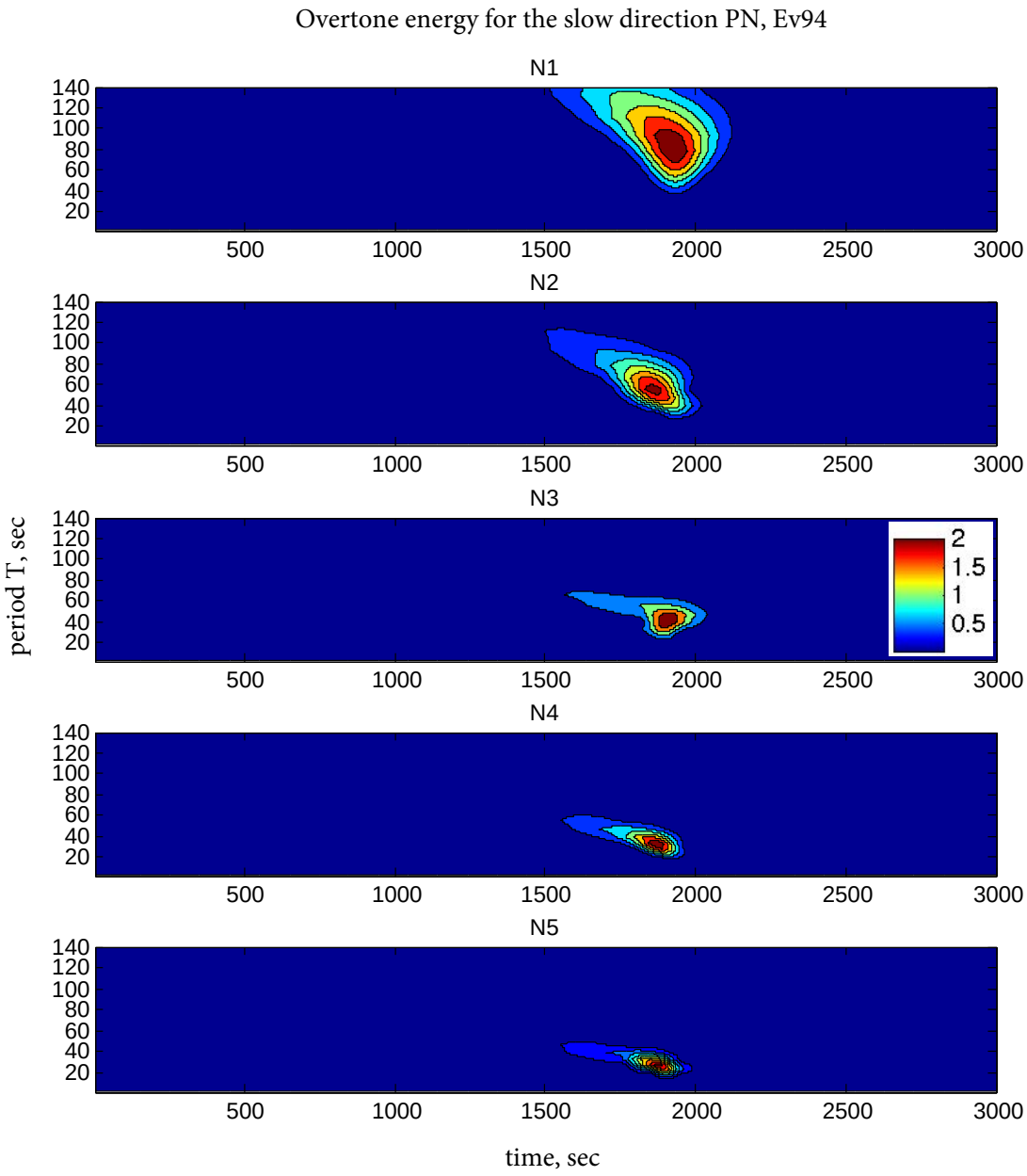

Figure 6.7: Example of the period dependence of the overtone energy, for the synthetic data computed for the first five overtones ($n = 1$ to $n = 5$) using event 94 as the source.

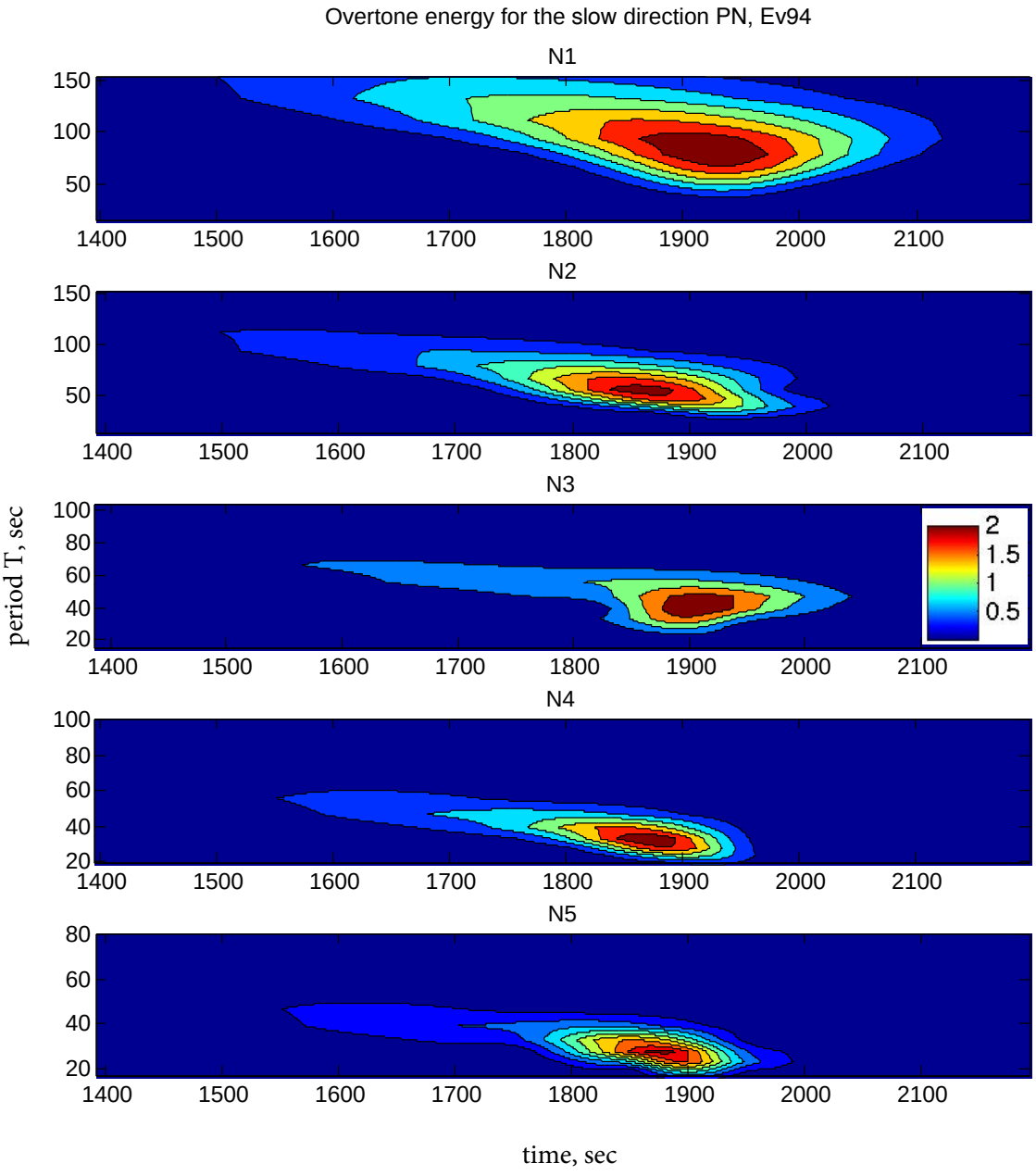

Figure 6.8: The regions of significant energy from Fig. 6.7 presented in more detail.

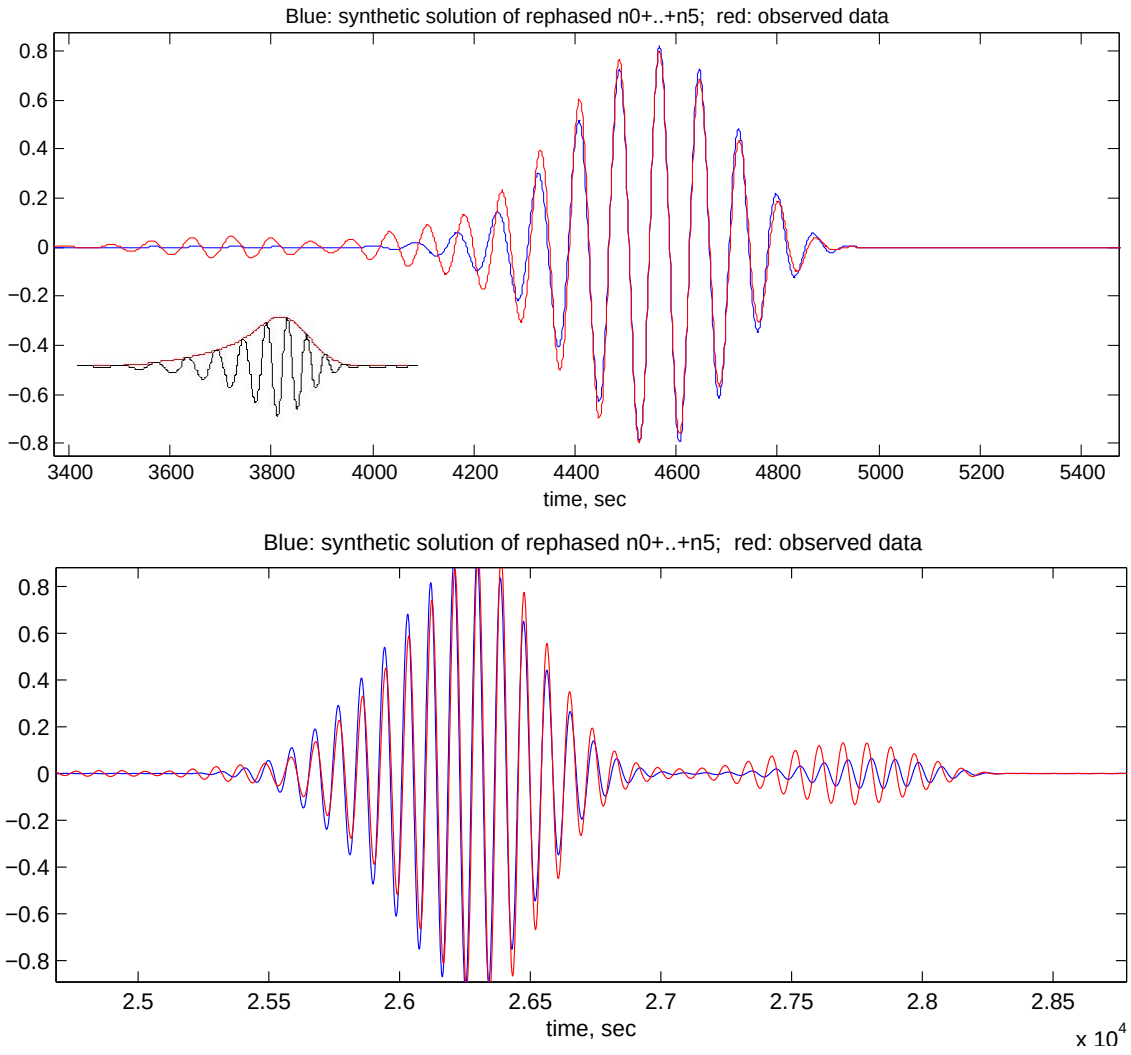

Figure 6.9: Comparison between data (red) and the final synthetic waveform (blue) obtained as summation of the first five shifted overtones (blue) for the period interval of 75 to 85 s (top panel) and 95 to 105 s (bottom panel) for one station and one event. Insert: A synthetic waveform with Hilbert transform envelope that is used to eliminate the cycle skipping problem around a phase arrival.

6.4 Computed phase velocities of the overtones

Our results in terms of phase velocities computed for the first five overtones for different periods are shown in Figs. 6.10-6.11. Each panel corresponds to a cluster of events, i.e., to an arrival direction (Fig. 6.1 and Table 6.1). The range of periods analyzed for each overtone is determined by the presence of significant overtone energy, as discussed in the previous section. The results can be compared to PREM predictions (solid lines). We see that the deviations are generally small, which is consistent with commonly found anisotropy effects of several percent; e.g., our shear wave splitting analysis indicates 1.5-3%. Interestingly, different overtones behave differently with respect to PREM. For example, for cluster PA (top panel of Fig. 6.10) which corresponds to the fast shear wave splitting direction, the first overtone is approximately on top of the PREM prediction, the next two overtones are slower than PREM in most periods, and the last overtone $n = 5$ is faster. There is also a dependence on the period, with some periods slower or faster than PREM for the same overtones. This complexity reflects the combination of non monotonic sensitivity kernels for different overtones at different periods (Fig. 1.3), as well as the potential complexity of the earth's structure at different depths.

Least-squares calculation errors for several period ranges and directions are shown in Fig. 6.12. The errors are generally less than 1% to 1.5%. This corresponds to the absolute phase velocity errors of the order of 0.05 to 0.11 km/s, depending on the period and overtone. Hence, on all plots that contain phase velocity results, the error is smaller than or similar to the size of the symbols used in the plot. That is why we do not plot error bars.

Based on our shear wave splitting analysis of section 5.4, cluster PA corresponds to the fast direction and clusters PN and D5 correspond to the slow direction (with opposite arrivals). Hence we are interested in comparison between results for different clusters. Fig. 6.13 compares the phase velocities for the first overtone for all directions. Indeed, we see systematic differences, with cluster PA corresponding to the largest phase velocities for a

number of periods. Interestingly, for this overtone, cluster D3 seems to correspond to the slowest direction. However, as we will see in the following, this is not true for all overtones and periods.

Let us compare the obtained results with azimuthal anisotropy assumed in our shear wave splitting analysis. To that end, we consider the phase velocities for two cases (Fig. 6.14): $n = 1$ (top panel) and $n = 2$ (bottom panel), both for the period range of 75-85 s, and compare their variation to the sine of twice the azimuth of the ray, $\sin(2\Theta)$ (Montagner and Nataf, 1986). We choose this period range because most of the directions have the results in that range for the first and second overtones.

We see that, for $n = 1$, the results for five out of six directions correspond to the $\sin(2\Theta)$ quite well, indicating that azimuthal anisotropy is a relevant assumption. Furthermore, for this case, direction PA appears to be not just faster that the other directions that we have considered, which we have already established, but indeed the fastest direction. Note that direction D3 (not plotted in Fig. 6.14, top panel) is an exception to the $\sin(2\Theta)$ fit. Its phase velocity, 5.1 km/s, is quite different from - and much lower than - the other directions. This may indicate either that some additional structural complexity exists along the corresponding path or that the parameters of the least squares inversion need to be further optimized. Understanding this deviation will be the subject of future research.

For the second overtone and periods of 75-85 s, the phase velocities no longer have a clear $\sin(2\Theta)$ dependence. This may be due to the fact that the second overtone has a more complex sensitivity kernel. Furthermore, the direction PA is no longer the fastest direction. This implies that, for the period range of 75-85 s, the first overtone is sensitive to the depths that dominate shear wave splitting results while the second overtone is not. This is exactly the kind of difference that could allow us to constrain the depth range of the anisotropy based on higher modes. Note that direction D2 does not appear on the plot because the second overtone does not have significant enough energy in this period range for direction

D2 to be included in the analysis.

Differences in the computed phase velocities between the fast shear-wave-splitting direction (cluster PA) and other directions are given in Figs. 6.15-6.18. Overall, we see that direction PA tends to have faster phase velocities for most periods for the first overtone, especially within periods of 55 to 95 s, and for the second overtone within periods of 35 to 65 s. The phase velocities for the second overtone within periods of 65 to 95 s tend to be slower for the PA direction than the other directions. The PA direction also tends to have slower phase velocities for the third overtone and higher phase velocities for the fourth and fifth overtone.

Note that these results may be sensitive to the choice of parameters in our approach. In particular, as already discussed, only overtones with significant enough energy for each period range and direction of interest are included in the analysis. Excluding overtones with low energy helps to obtain what looks like meaningful results, as it reduces the noise and the number of parameters involved. However, it is important to investigate the dependence of the results on the energy threshold; this will be the subject of future work.

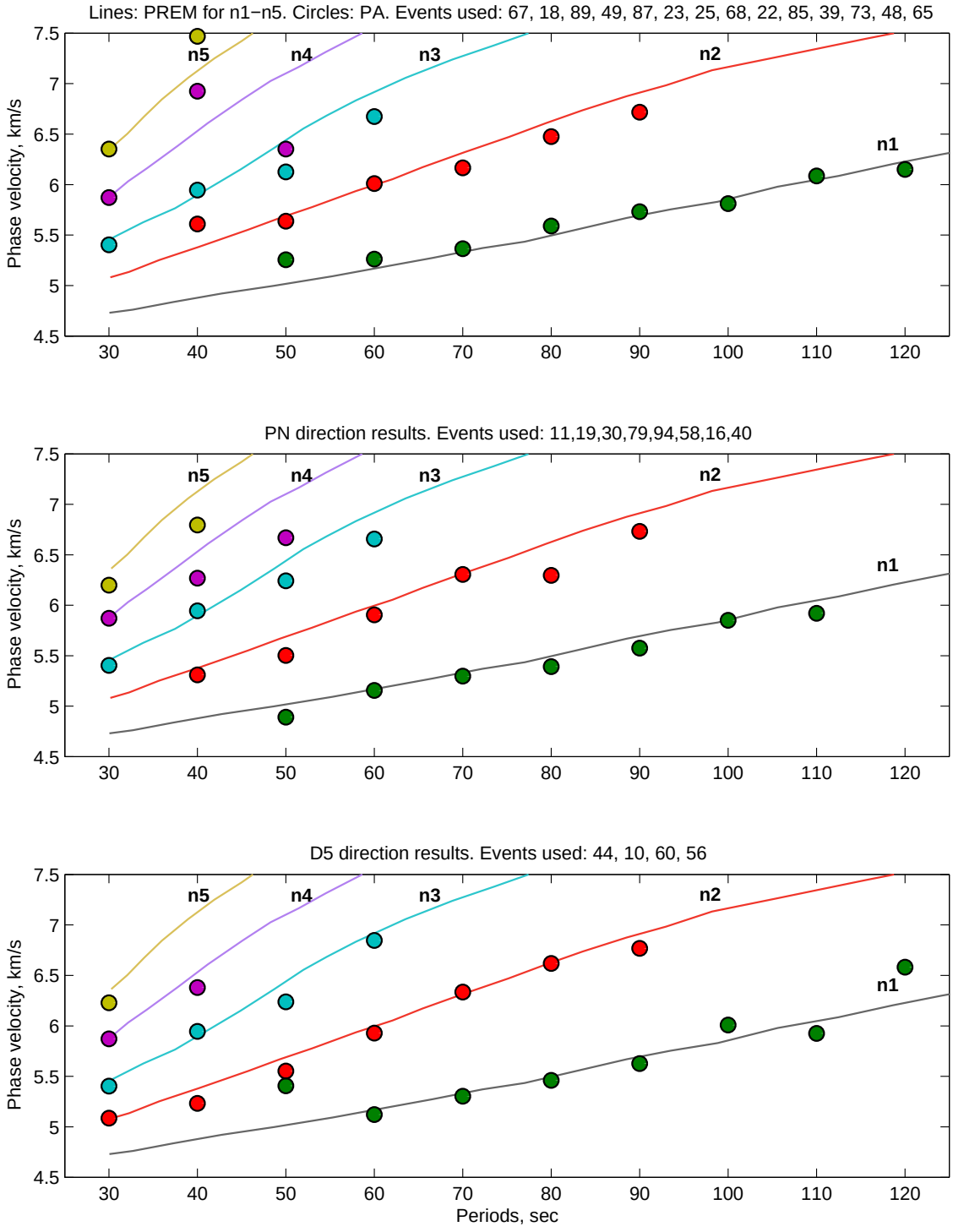

Figure 6.10: Computed phase velocities (circles) for the first five overtones and different periods. Different panels correspond to different events clusters and hence different directions: PA (top), PN (middle) and D5 (bottom). Phase velocities predicted by PREM (lines) are shown for comparison.

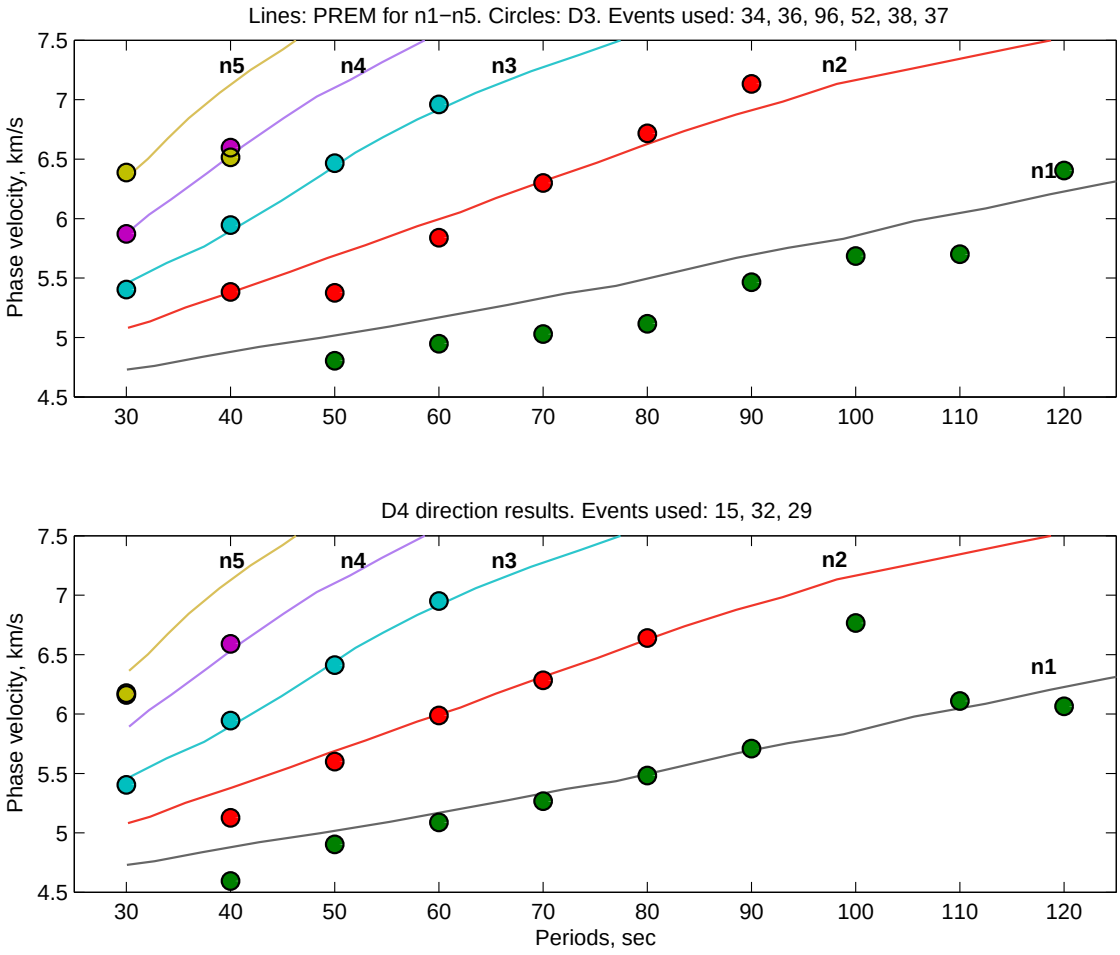

Figure 6.11: Continuation of Fig. 6.10 for directions D3 (top) and D4 (bottom).

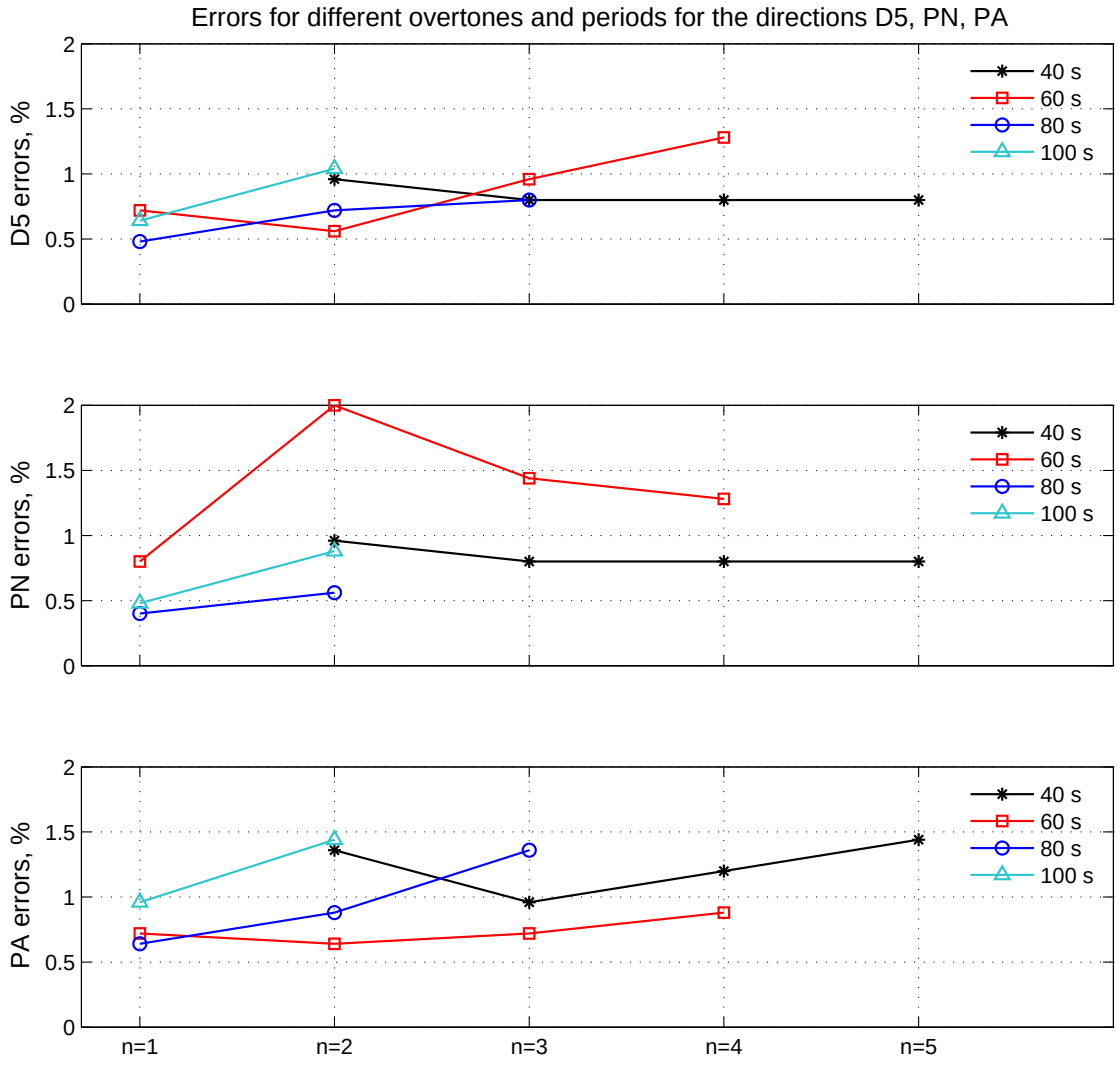

Figure 6.12: Least-squares calculation errors for three directions and representative ranges of periods (40 s refers to the range 35-45 s etc). For each period range, the error is shown for the overtones that have significant energy in that range.

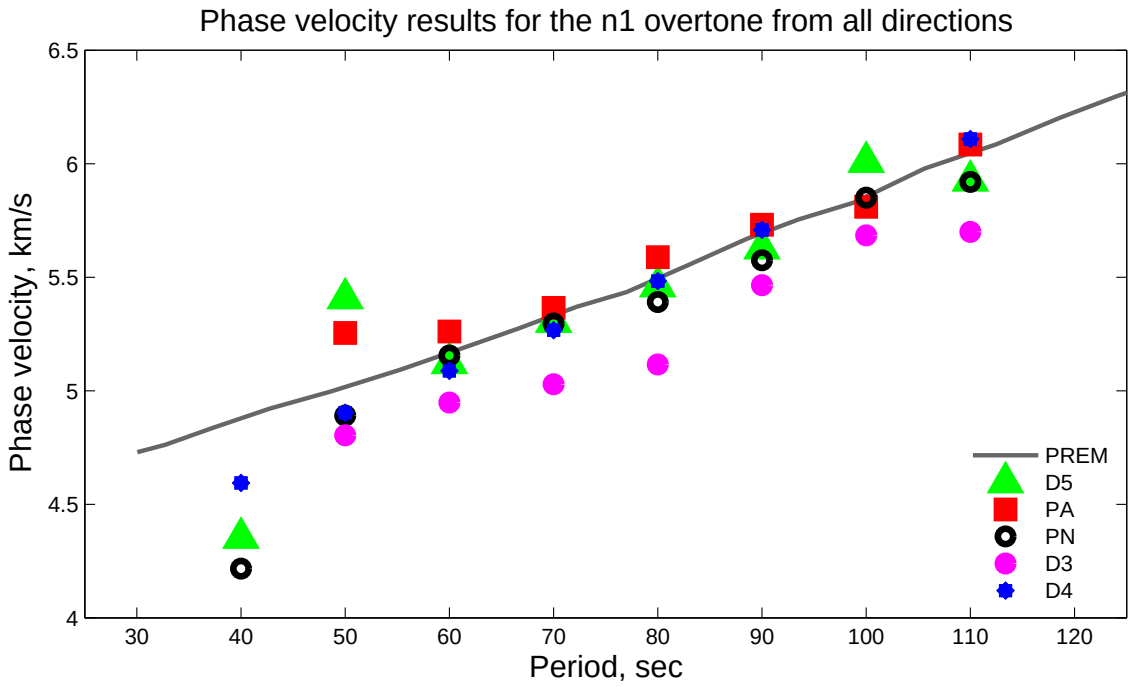

Figure 6.13: Comparison between phase velocities for the first overtone for different periods and directions.

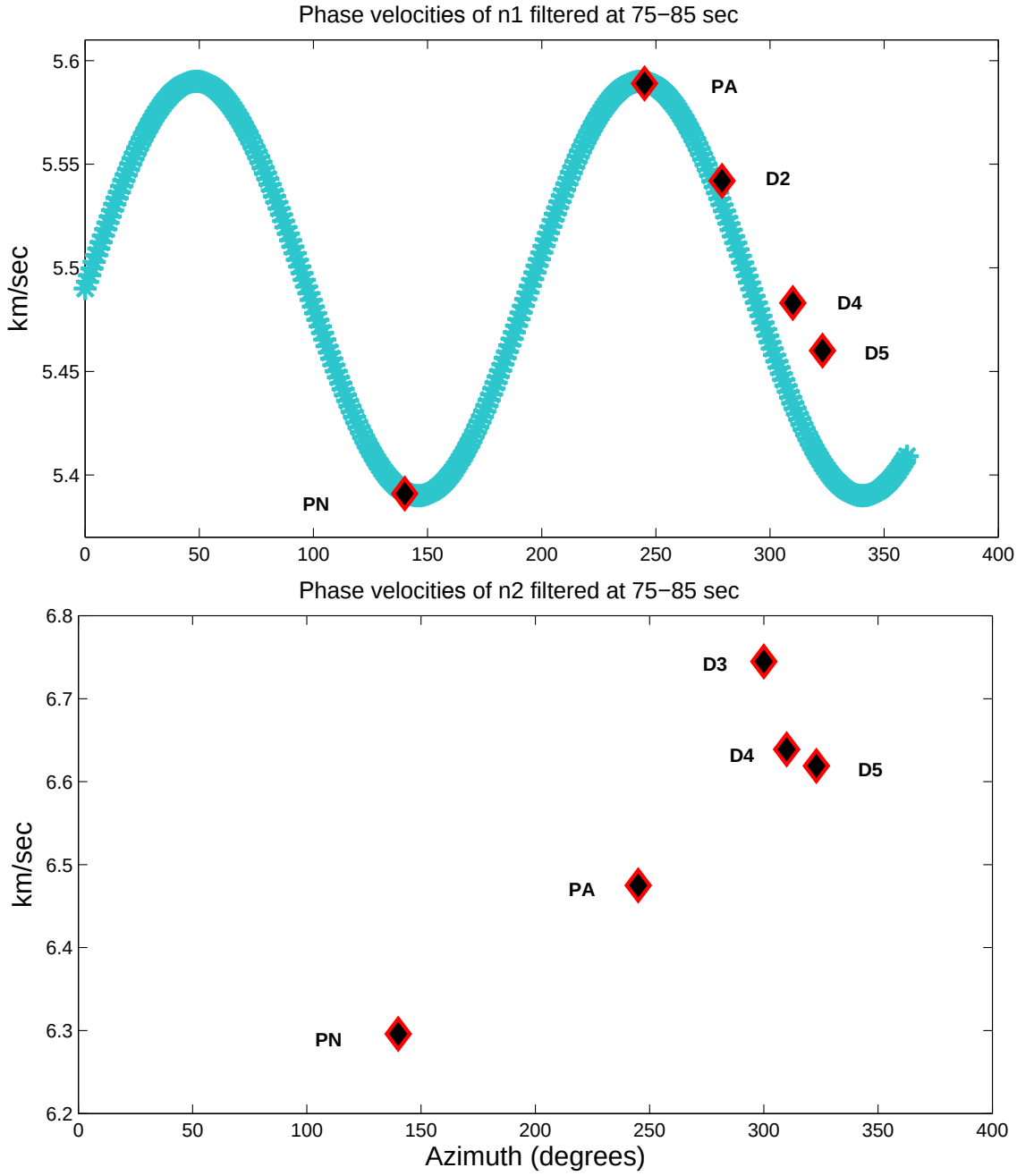

Figure 6.14: Comparison of the phase velocities for data filtered at $75-85$ s with the $sin(2\Theta)$ variation indicative of azimuthal anisotropy for (top panel) $n = 1$ and (bottom panel) $n = 2$. The velocities for $n = 1$ are fitted by $sin(2\Theta)$ quite well, except for direction D3 (not plotted) as discussed in the text, with direction PA being the fastest. The velocities for $n = 2$ do not have a clear $sin(2\Theta)$ dependence, and direction PA is no longer the fastest.

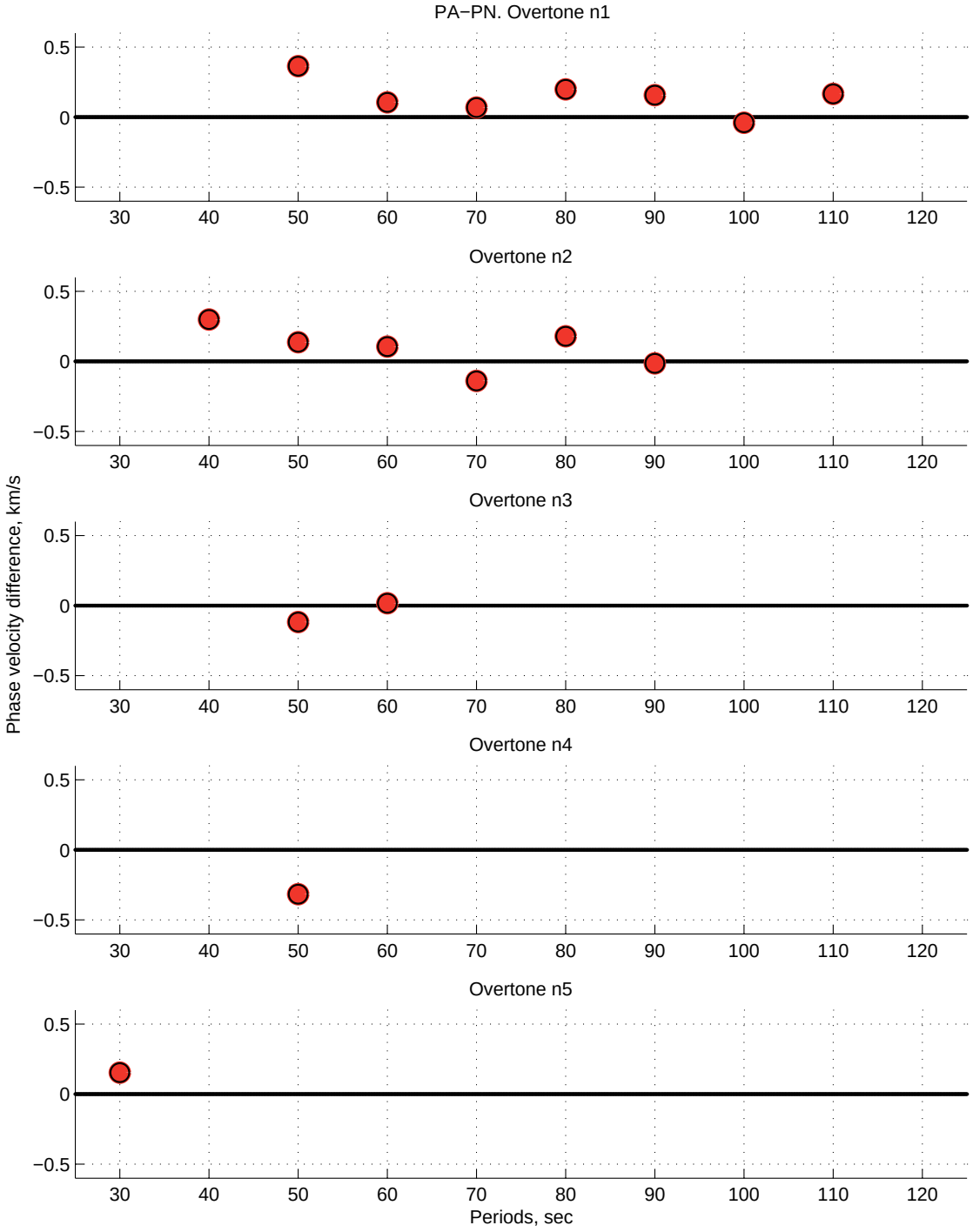

Figure 6.15: PA-PN difference of overtone phase velocities for different periods and modes.

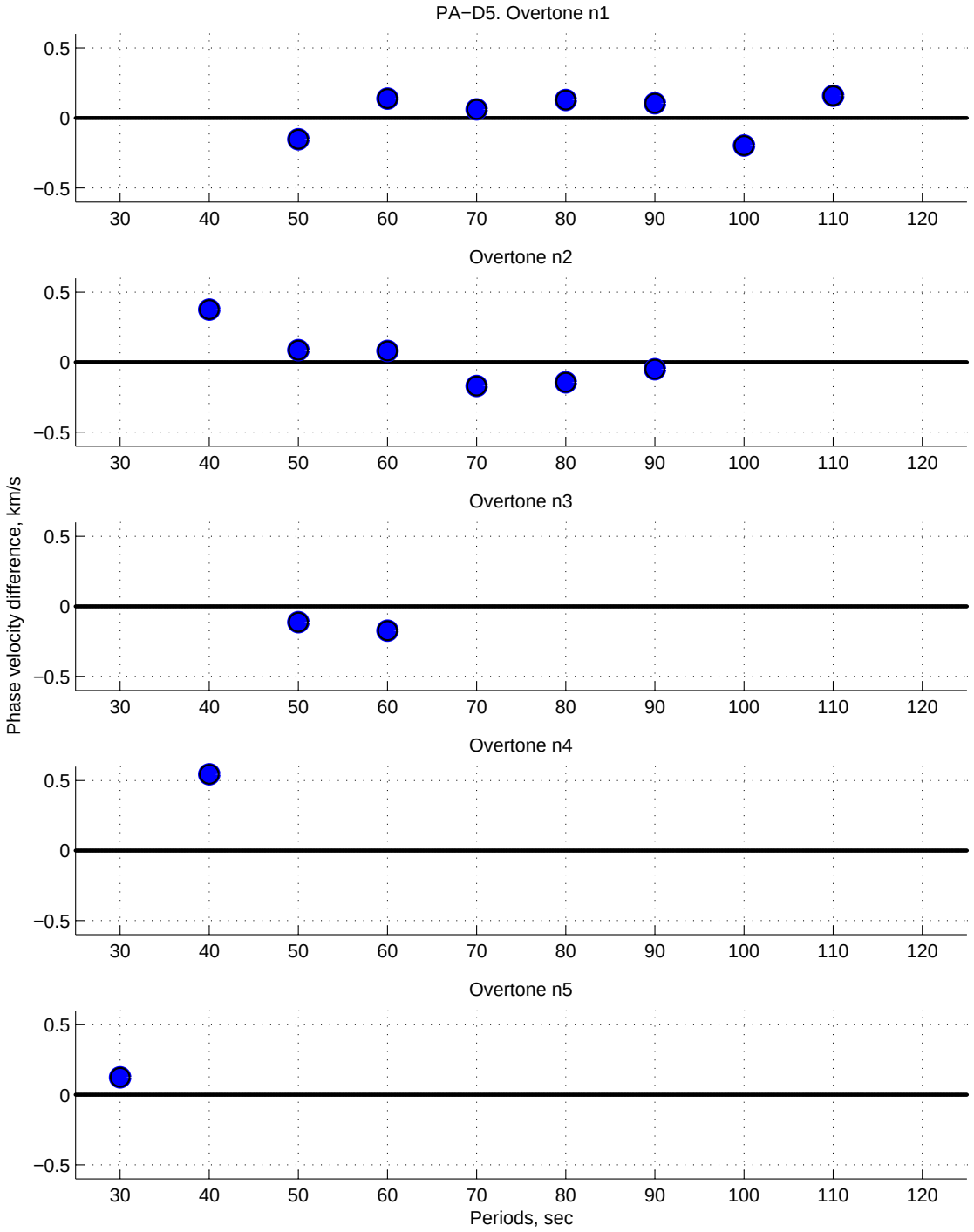

Figure 6.16: PA-D5 difference of overtone phase velocities for different periods and modes.

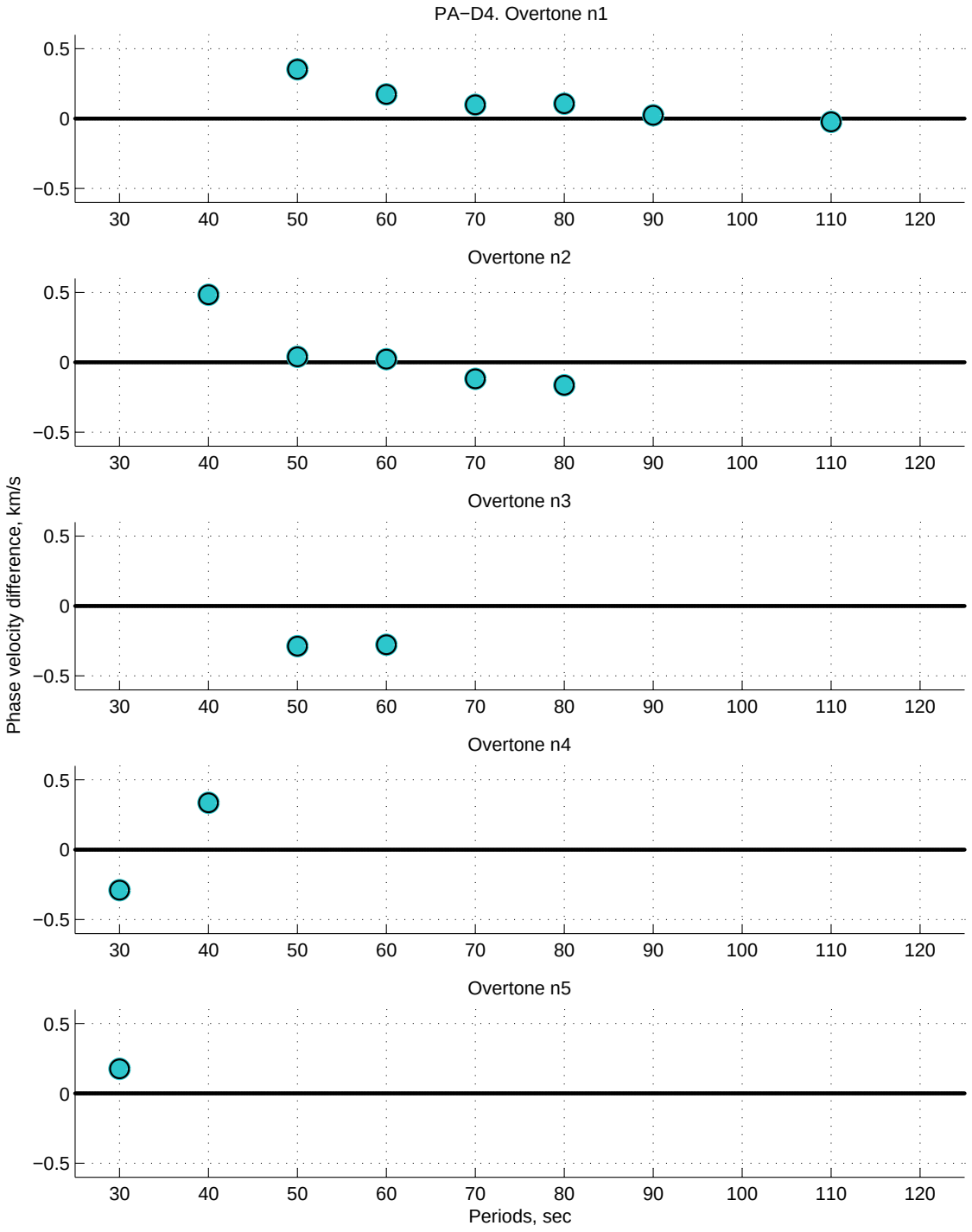

Figure 6.17: PA-D4 difference of overtone phase velocities for different periods and modes.

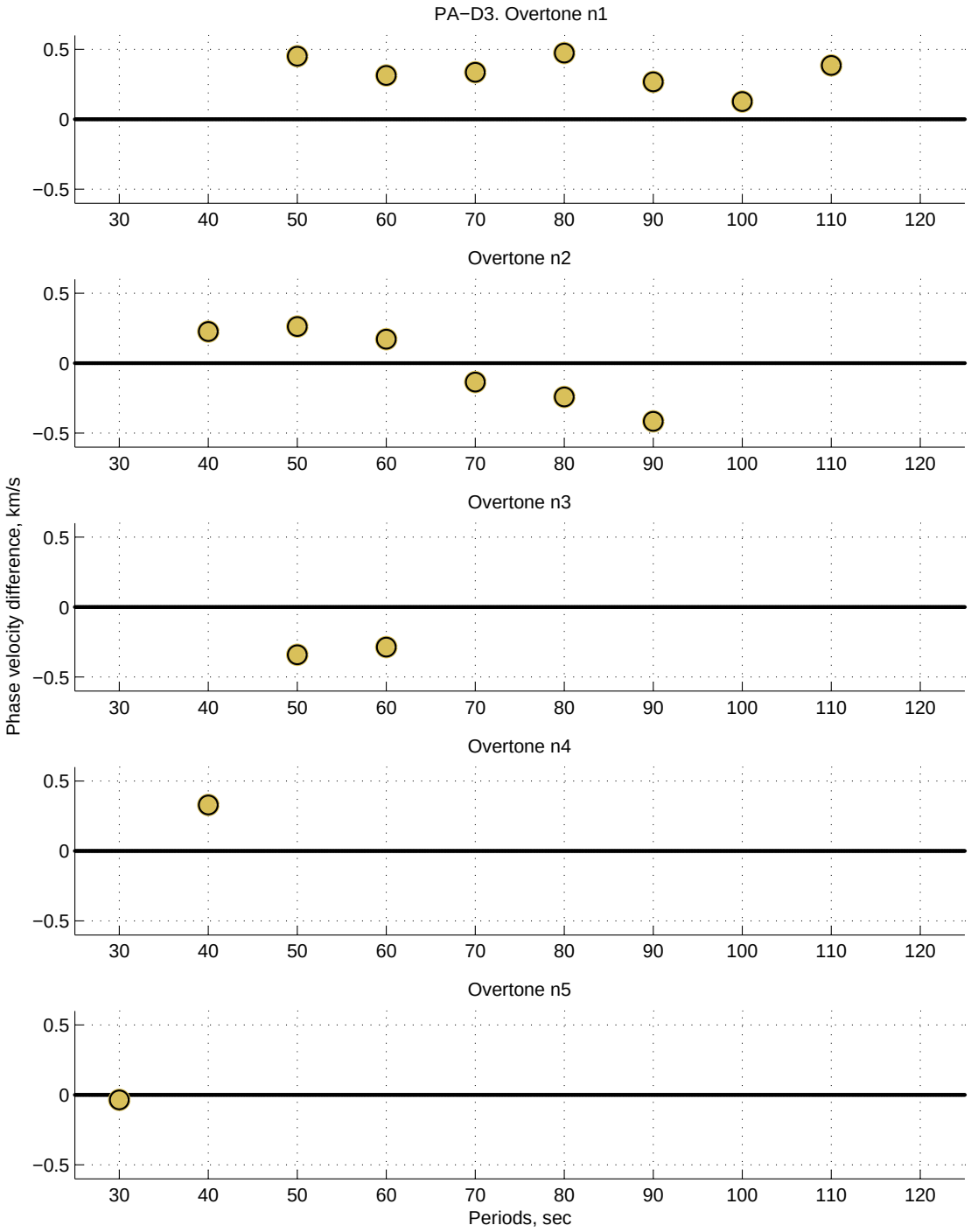

Figure 6.18: PA-D3 difference of overtone phase velocities for different periods and modes.

6.5 Interpretation in terms of the depth and strength of anisotropy

To interpret the differences in the computed phase velocities in terms of the depths that make PA the fast shear-splitting direction, let us focus on the first two overtones. We need to look for the depths for which (i) the second overtone is more sensitive within periods of 35 to 65 s than within periods 65 to 95 s. At the same time, (ii) the first overtone should also be sensitive to those same depths, to explain the faster phase velocities for that overtone. Looking at the corresponding sensitivity kernels (Fig. 6.19), we can make the following tentative conclusions. The first overtone at periods between 40 and 70 s is not sensitive to the depth below 600 km or so, and yet the corresponding phase velocities are faster for PA direction, making the depth between 600 km unlikely to dominate the anisotropy results. This conclusion is further supported by the fact that the second overtone is sensitive for the depths below 600 km for longer periods of 70 s and more, and yet the phase velocities for those periods are slower in PA direction. From our fundamental surface wave inversions (sections 3 and 4), we know that the top 200 km or so have different anisotropy from the shear wave splitting results. This is consistent with the higher mode results, since PA being the fast direction in the top 160 km would significantly affect the first and second overtone in all periods, yet some periods of the second overtone are not faster in that direction. Hence we are left with depths between 160 and 600 km. Examining the kernels within those depths, we note the region between about 200 and 300 km, or perhaps between 200 and 400 km. The shorter periods of the second overtone are more sensitive to this region than the longer periods, fulfilling condition (i). All periods for the first overtone are also sensitive to that region, fulfilling condition (ii).

Hence the depths between 200 and 300 km, or perhaps 200 and 400 km are likely candidates for the anisotropic layer that creates the shear wave splitting of Chapter 5. That depth range likely corresponds to the bottom of the asthenosphere, and it may be quite affected by the plate motion, explaining why the fast shear wave splitting direction is aligned with the

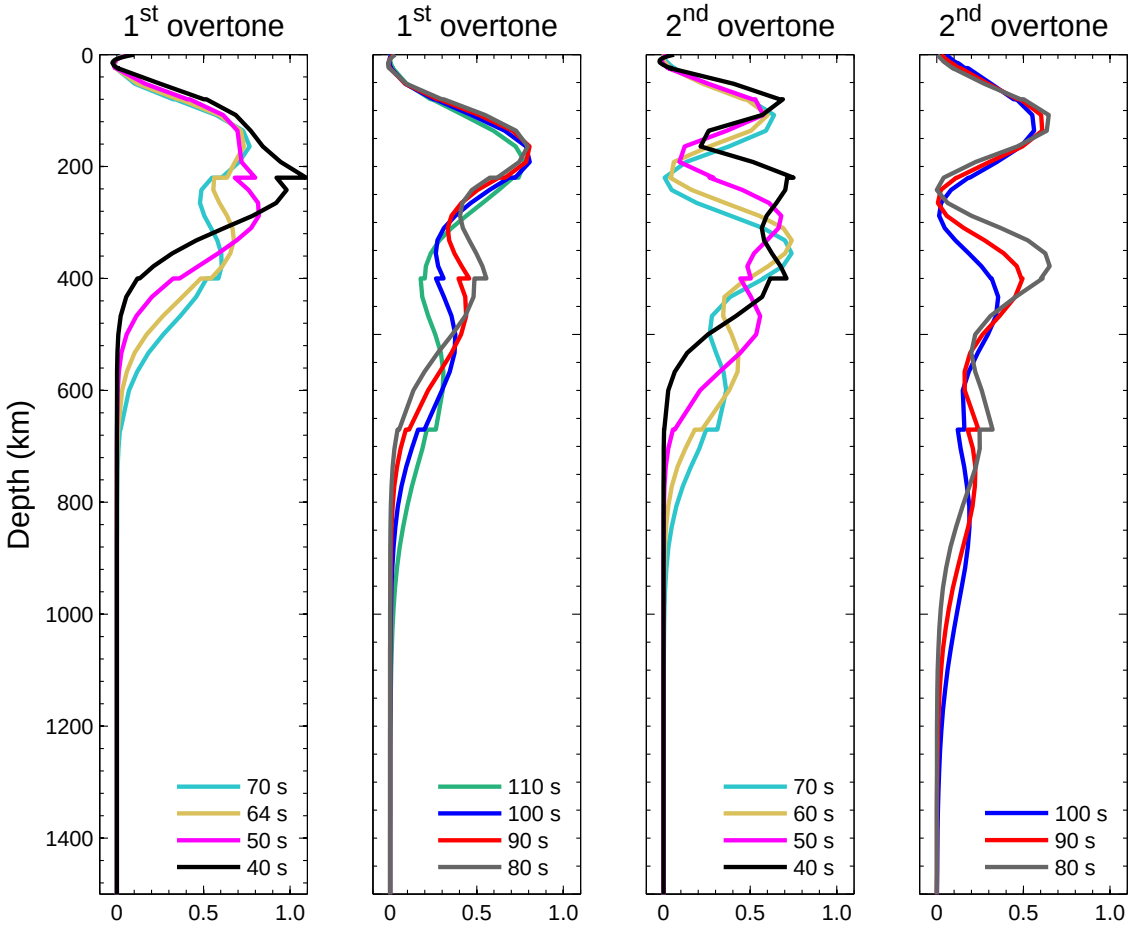

Figure 6.19: Normalized sensitivity kernels for modes $n = 1$ and $n = 2$.

plate motion. The anisotropy may be evidence of the plate's deep roots and their effect on mantle deformation. This anisotropy depth and the splitting times of 1-2 s that it creates are similar to the Northern Australia results presented by Tong et al., 1994 , who find that the most likely source region of the anisotropy in Australia is the asthenospheric zone between 210 and 410 km.

Two questions can be asked about this tentative estimate of the anisotropy depth. The first question is whether such layer can create the shear wave splitting time delays of 1-2 s obtained in Chapter 5. The depth d of the anisotropic layer, its anisotropy of a percent, the

shear wave splitting time delay Δt, and the shear wave speed V_s can be related as:

$$d = \frac{\Delta t}{1/[(1-a/200)V_s] - 1/[(1+a/200)V_s]} = \frac{1}{2}V_s\Delta t\left(\frac{200}{a} - \frac{a}{200}\right) \approx V_s\Delta t\frac{100}{a}, \tag{6.3}$$

and hence a can be estimated as:

$$a \approx 100\left(\frac{V_s\Delta t}{d}\right). \tag{6.4}$$

To cause the inferred Δt of 1 to 2 s, a 100-km layer around the depth of 250 km (with $V_s = 4.6$ km/s) would need to have 4.6% to 9.2% anisotropy, and a 200-km layer around the depth of 300 km (with $V_s = 4.7$ km/s) would need 2.35% to 4.7%. All of these values are reasonable (Baptiste and Tommasi, 2014; Crampin et al., 2014), although the anisotropy required for 2 s and 100-km layer is close to the maximum values cited in the literature.

The second question is whether such layers could sufficiently affect the phase velocities of the overtones which have broader sensitivity kernels. This should be possible to answer through forward modeling, which is beyond the scope of this work. However, for qualitative comparison, we can compute the percentage difference between phase velocities of the first two overtones in the fast direction PA and slow directions PN and D5. For example, for PA and PN, we compute:

$$\Delta\% = 100\frac{V_{PA} - V_{PN}}{V_{PA}}. \tag{6.5}$$

This calculation results in 1-3% difference for most periods for which the phase velocity of PA is indeed faster (Fig. 6.20), with the exception of the lowest period ranges, for which the difference is 4-6%. Importantly, the results for clusters PN and D5 are broadly similar, which is consistent with them both representing the slow direction. Note that these values of "higher-mode anisotropy" cannot be directly compared to the anisotropy estimates of 2.35-9.2% based on shear wave splitting, as given above. This is because differences $\Delta\%$ in phase velocities of higher modes reflect non-uniform averaging over a range of depths, while the shear-wave-splitting-based anisotropy percentage estimates refer to the actual anisotropy in

a relatively narrow layer. However, it would seem that the anisotropy of the narrow layer should be larger than the resulting effect $\Delta\%$ on the higher-mode phase velocities, since the phase velocities would also reflect the properties of other depths, potentially without - or with a different - anisotropy. This argument is broadly consistent with our estimates of 2.35% to 4.7% for a 200-km layer and 4.6% to 9.2% for a 100-km layer, since both of these ranges are larger than the 1-3% difference in the higher-mode phase velocities.

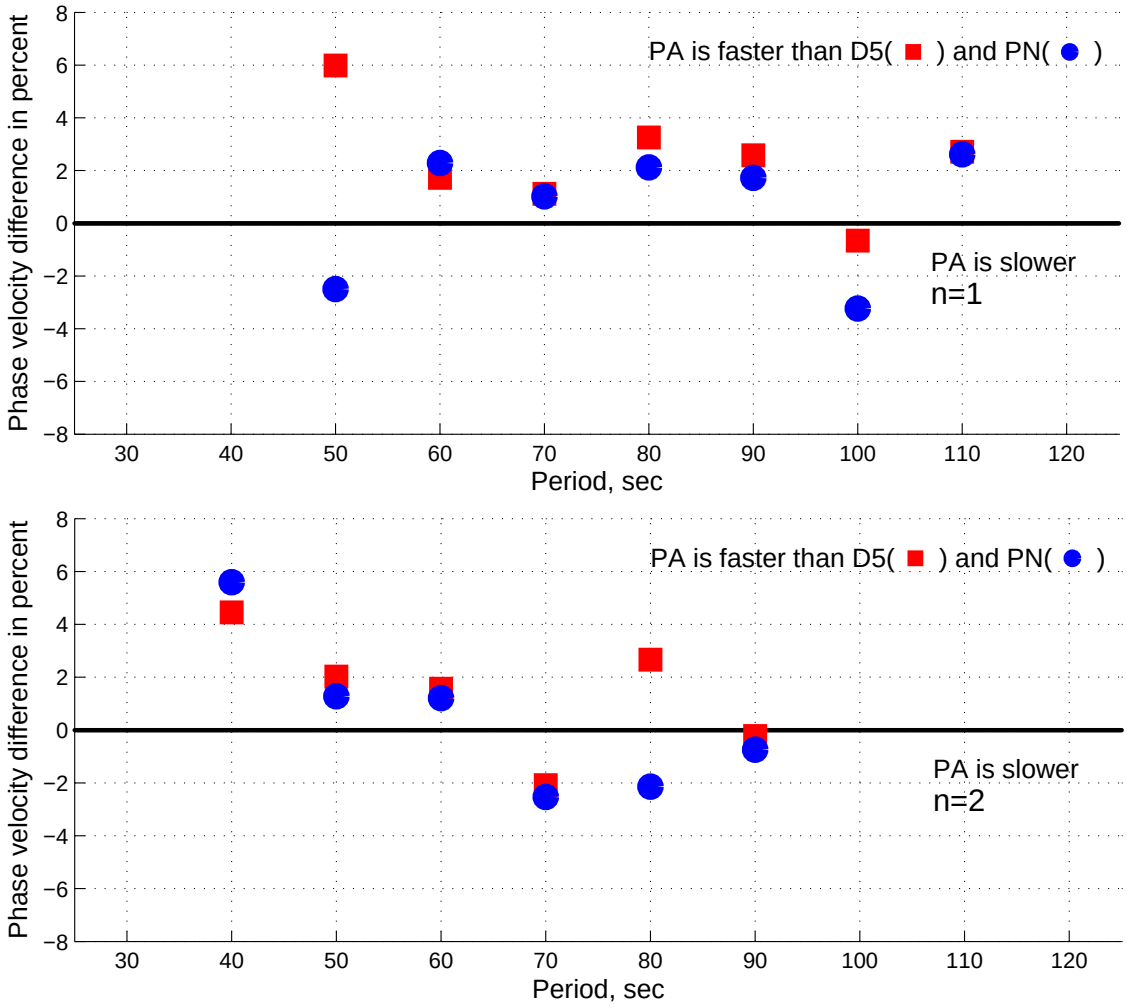

Figure 6.20: Anisotropy in percent between PA, PN, and D5 directions for different periods based on the phase velocity values.

CHAPTER 7

Conclusions

This work has examined the anisotropy below Mexico and its implications for the 3D structure in the region using multiple seismological techniques: phase velocities of the fundamental mode Rayleigh waves, shear wave splitting based on the SKS and SKKS phases, and phase velocities of higher mode Rayleigh waves. Our goal is to answer the following major geophysical questions: How does the subduction transition from flat to steep along the trench - is the subducting slab bent or torn? Why is the TransMexican Volcanic Belt oblique to the trench and what is the origin of the Tzitzio volcanic gap? Is there significant shear-wave splitting in the region? If so, at what depth is it generated, and how does it relate to mantle flow?

The main accomplishments of the presented thesis are as follows. We have:
– determined the anisotropy and 3D mantle dynamics within the top 200 km under Mexico, inferring the existence of two slab gaps and the resulting mantle flow;
– explained the obliqueness of the Trans Mexican Volcanic Belt and existence of the Tzitzio volcanic gap;
– found significant shear wave splitting in Mexico, with fast direction mostly aligned with the absolute plate motion, and established that its source must be deeper than 200 km;
– developed a technique for separating Rayleigh wave higher modes using their group energy identified with wavelets;
– used the higher-mode analysis to determine phase velocities for different overtones and periods and then constrained the depth of the shear-wave splitting anisotropy to a 200-400

km layer.

The study has been enabled by the unique data set collected by Meso American Seismic Experiment (Chapter 2). In MASE, a temporary seismic array of 100 seismometers spanned 500 km in Mexico, with half of the array being a wireless network that we helped to design, install, and maintain. Our involvement facilitated all aspects of the experiment, including instrument design and testing, software development, site selection, sensor installation, connections with local scientists, network maintenance, and data storage and management. In the future, the anisotropy and structure under Peru can be investigated using a similarly extensive dataset collected with our active participation.

Our examination of the anisotropy under Mexico points to quite a complex depth-variable structure.

To study the top 200 km, we have constructed Rayleigh wave phase velocity maps, including the effect of the anisotropy (Chapter 3), and inverted the results for the 3D structure of the zone in terms of shear wave velocities and their anisotropy (Chapter 4). The lateral variations in the isotropic part of the velocity structure in the mantle lithosphere point to the different styles of subduction on the two sides of the Orozco Fracture Zone (OFZ), with steep subduction to the northwest and nearly flat subduction to the southeast. This finding is consistent with previous studies of the structure using different methods (Husker, 2008; Perez-Campos et al., 2008; Iglesias et al., 2010; Orozco et al., 2007) as well as with the two parts of the slab having different ages and hence different densities (Blatter et al., 2007; Kanjorski, 2003; Manea et al., 2006). The deeper, asthenospheric layer reveals lower velocities below the TMVB, presumably due to dehydration effects.

The anisotropy pattern in the top 200 km is consistent with a tear along the OFZ, between the two styles of subduction, with another tear between the steep Cocos and Rivera slabs, and with the associated toroidal return flows through the tears and around the steeply dipping section of the Cocos slab. This conclusion is supported by the gradual variation

of the fast directions from trench-parallel near the trench to trench-perpendicular inland west of the OFZ. The flows could be caused by the slab rollback/retreat evidenced by GPS velocities and migration of the TransMexican Volcanic Belt (TMVB) (DeMets et al., 1994; Manea et al., 2005; Mori et al., 2007).

Our hypothesis that the slab is torn allows for a new insight into the structure of the TMVB. The TMVB can be interpreted as consisting of two segments associated with the two parts of the torn slab. Each segment is parallel to the trench, as commonly found in subduction zones. However, the two TMVB segments are located at different distances from the trench, consistent with the different angles of subduction. This creates an apparent oblique orientation of the TMVB. The segmented structure of the TMVB also provides a natural explanation for the Tzitzio gap in volcanism, which is located on top of the OFZ, where the two proposed TMVB segments are shifted with respect to each other.

Our shear wave splitting analysis (Chapter 5) points to a significant anisotropic structure deeper than 200 km. The analysis indicates delay times of 1-2 s and an average fast direction that coincides with the absolute plate motion for the MASE stations as well as stations east of the MASE array. The significant difference between the fast direction and magnitude of the anisotropy in the upper 200 km, as detected by the surface wave analysis, and the average anisotropy from the core-mantle boundary (CMB) to the surface, as resolved by the shear wave splitting, implies that the shear wave splitting results are dominated by a structure deeper than 200 km. Since the time delays are significantly longer for the shear wave splitting results, the deeper structure is either much larger than 200 km, or has stronger anisotropy than the top 200 km, or a combination of both. At the same time, several relatively subtle features in the shear wave splitting results reveal potential influences of the shallow structure and its deeper extensions. This includes a small change in the fast direction around the southern edge of the TMVB, which is located above the transition from the flat to steep subduction, as well as a different pattern of fast directions west of the MASE array, the

region on top of two smaller subducting slabs.

Finally, our higher-mode investigation (Chapter 6) shows that the phase velocities for a number of overtones and periods are fastest in the direction predicted by the shear wave splitting analysis, suggesting that the shear-wave splitting and higher modes are affected by the same deeper structure. Remarkably, the results for different directions are consistent with the presence of azimuthal anisotropy. Inspection of our results together with the sensitivity kernels tentatively indicates that the 200-400 km depths are likely candidates for the source of the anisotropy. Indeed, we find that the shear wave splitting delays of 1-2 s can be produced by such a layer for reasonable values of anisotropy, 2.35% to 4.7% for a 200-km layer and 4.6% to 9.2% for a 100-km layer. Furthermore, it is plausible that a 100-200 km layer with such anisotropy would be able to cause the 1-3% difference that we find between the higher-mode phase velocities for the fast and slow directions. The depths between 200 and 400 km likely correspond to the bottom of the asthenosphere, and they may be affected by the plate motion, explaining why the fast shear wave splitting direction is aligned with the plate motion. The anisotropy may reflect evidence of the plate's deep root and its effect on mantle deformation. This tentative estimate of the anisotropy depth, and the shear-wave splitting times of 1-2 s that it creates, are similar to Northern Australia, where an anisotropic source has been found in the asthenospheric zone between 210 and 410 km (Tong et al., 1994). To fully use the obtained phase velocities for different overtones and periods for characterizing the structure below Mexico, one needs to conduct an inversion for the three dimentional properties, similar to our efforts in Chapter 4 for the fundamental mode phase velocity maps. This will be a subject of future work.

Bibliography

Alsina, D. and Snieder, R. (1995). Small-scale sublithospheric continental mantle deformation: Constraints from SKS splitting observations. *Geophys. J. Int.*, 123:431448.

Astiz, L., Eakins, J. A., Martynov, V. G., Cox, T. A., Tytell, J., Reyes, J. C., Newman, R. L., Karasu, G. H., Mulder, T., White, M., Davis, G. A., Busby, R. W., Hafner, K., Meyer, J. C., and Vernon, F. L. (2014). The array network facility seismic bulletin: Products and an unbiased view of united states seismicity. *Seismological Research Letters*, 85(3):576–593.

Atwater, T. and Stock, J. (1998). Pacific North America plate tectonics of the Neogene southwestern United States: an update. *Int. Geol. Rev.*, 40:375–402.

Backus, G. (1970). A geometrical picture of anisotropic elastic tensors. *Reviews of geophysics*, 8(3):633–671.

Baptiste, V. and Tommasi, A. (2014). Petrophysical constraints on the seismic properties of the kaapvaal craton mantle root. *Solid Earth*, 5:1–19.

Bassin, C., Laske, G., and Masters, G. (2000). The current limits of resolution for surface wave tomography in North America. *EOS Trans. AG*, 81:F897.

Beghein, C., Snoke, J., and Fouch, M. (2010). Depth constraints on azimuthal anisotropy in the Great Basin from Rayleigh wave phase velocity maps. *EPSL*, 289:467–478.

Bevington, P. and Robinson, D. (1992). Data reduction and error analyses for the Physical Sciences. *McGrow-Hill, New-York*.

Blatter, D., Farmer, G., and Carmichael, I. (2007). A north-south transect across the Central Mexican volcanic belt at ∼100w: spatial distribution, petrological, geochemical, and isotopic characteristics of quaternary volcanism. *Journal of Petrology*, 48:901–950.

Brune, J. and Dorman, J. (1963). Seismic waves and earth structures in the Canadian

shield. *Bull. Seism. Soc. Am.*, 53:167–210.

Chen, T. and Clayton, R. W. (2009). Seismic attenuation structure in central Mexico: Image of a focused high-attenuation zone in the mantle wedge. *J. Geophys. Res.*, 114:B07304.

Crampin, S., Chesnokov, E. M., and Hipkin, R. (1984). Seismic anisotropy; the state of the art, II. *Geophysical Journal of the Royal Astronomical Society*, 76:.

Crampin, S., Chesnokov, E. M., and Hipkin, R. (2014). A review of the current understanding of seismic shear-wave splitting in the earths crust and common fallacies in interpretation. *Wave Motion*, 45:675–722.

Crotwell, H. P., Owens, T. J., and Ritsema, J. (1999). The taup toolkit: Flexible seismic travel-time and ray-path utilities. *Seismological Research Letters*, 70:154160.

Dahlen, F. A. and Tromp, J. (1998). Theoretical global seismology. *Princeton University Press*.

Darbyshire, F. A. and Lebedev, S. (2009). Rayleigh wave phase-velocity heterogeneity and multi-layered azimuthal anisotropy of the Superior Craton, Ontario. *Geophys. J. Int.*, 176:(1).

Davis, P. (2009). Azimuthal variation in seismic anisotropy of the southern California uppermost mantle. *J. Geophys. Res*, B1:637.

DeMets, C., Gordon, R. G., Argus, D. F., and Stein, S. (1994). Effect of recent revisions to the geomagnetic reversal time-scale on estimates of current plate motions. *Geophys. Res. Lett.*, 21:2191–2194.

Dougherty, S. L. and Clayton, R. W. (2014). Seismicity and structure in central Mexico: Evidence for a possible slab tear in the South Cocos plate. *J. Geophys. Res. Solid Earth*, 119:34243447.

Dziewonski, A., Bloch, S., and Landisman, N. (1969). A technique for the analysis of transient seismic signals. *Bull. Seism. Soc. Am.*, 59:427–444.

Earle, P. and Shearer, P. (1994). Characterization of global seismograms using an automatic picking algorithm. *Bull. Seismol. Soc. Am.*, 84:366–376.

Ferrari, L. (2004). Slab detachment control on mafic volcanic pulse and mantle heterogeneity in central Mexico. *Geology*, 32(1):77–80.

Goldstein, P., Dodge, D., Firpo, M., and Minner, L. (2003). Sac2000: Signal processing and analysis tools for seismologists and engineers, invited contribution to the iaspei international handbook of earthquake and engineering seismology. *Academic Press, London*, Edited by WHK Lee, H. Kanamori, P.C. Jennings, and C. Kisslinger.

Gorbatov, A. and Fukao, Y. (2005). Tomographic search for missing link between the ancient Farallon subduction and the present Cocos subduction. *Geophys. J. Int.*, 160:849–854.

Grand, S. P. and Helmberger, D. (1984). Upper mantle shear structure of North America. *Geophysical Journal of the Royal Astronomical Society*, 76:n.

Herrmann, R. (1987). Computer programs in seismology. *Tech. rep. St. Luis University.*

Herrmann, R. and Ammon, C. (2002). Computer programs in seismology. *Tech. rep. St. Luis University.*

Husker, A. and Davis, P. (2009). Tomography and thermal state of the Cocos plate subduction beneath Mexico City. *J. Geophys. Res.*, 114.

Husker, A., Stubailo, I., Lukac, M., Naik, V., Guy, R., Davis, P., and Estrin, D. (2008). Wilson: The Wirelessly Linked Seismological Network and its application in the Middle American Subduction Experiment. *SRL.*

Husker, A. L. (2008). Tomography of the subducting Cocos Plate in central Mexico using data from the installation of a prototype wireless seismic network: Images of a

truncated slab. *PhD thesis, University of California, Los Angeles*, 1.

Iglesias, A., Clayton, R., Perez-Campos, X., Singh, S. K., Pacheco, J., Garcia, D., and Valdes-Gonzalez, C. (2010). S-wave, velocity structure below Central Mexico using high resolution surface wave tomography. *J. Geophys. Res.*, 115:B06307.

Kanjorski, M. (2003). Cocos Plate structure along the Middle America subduction zone off Oaxaca and Guerrero, Mexico: influence of subducting plate morphology on tectonics and seismicity. *PhD thesis, University of California, San Diego.*

Karato, S. (1987). Seismic anisotropy due to lattice preferred orientation of minerals: Kinematic or dynamic? *High Pressure Research in Mineral Physics, Geophysical Monograph, American Geophysical Union*, 39:455–470.

Karato, S. (1998). Seismic anisotropy in the deep mantle, boundary layers, and the geometry of mantle convection. *Pageop*, 151:565–587.

Kennett, B. L. N., Engdahl, E. R., and Buland, R. (1995). Constraints on seismic velocities in the Earth from travel times. *Geophys. J. Int.*, 122.

Kim, Y., Greene, F., Espejo, L., Perez-Campos, X., and Clayton, R. (2006). Receiver function analysis of the Middle American subduction zone in central Mexico. *Eos Trans. AGU*, 87(52).

Knopoff, L., Berry, M. J., and Schwab, F. A. (1967). Tripartite phase velocity observations in laterally heterogeneous regions. *J. Geophys. Res.*, 72(10):2595–2601.

Landisman, N., Dziewonski, A., and Sato, Y. (1969). Recent improvements in the analysis of surface wave observations. *Geophysical Journal of the Royal Astronomical Society*, 4:369–403.

Lin, F., Ritzwoller, M. H., Yang, Y., Moschetti, M. P., and Fouch, M. J. (2010). Complex and variable crustal and uppermost mantle seismic anisotropy in the western United States. *Nature Geoscience*, 4:5.

Londsdale, P. (1991). Structural pattern of the pacific floor offshore peninsular California, in Dauphin, J.P., and Simoneit, B.R.T. eds., The Gulf and Peninsular Province of the Californias. *American Association of Petroleum Geologists*.

Long, M. D. and Silver, P. G. (2008). The subduction zone flow field from seismic anisotropy: a global view. *Science*, 319:315–318.

Lukac, M., Girod, L., and Estrin, D. (2006). Disruption tolerant shell. *Special Interest Group on Data Communication (ACM SIGCOMM), Pisa, Italy*.

Lukac, M., Naik, V., Stubailo, I., Husker, A., and Estrin, D. (2007). In vivo characterization of a wide area 802.11b wireless seismic array. *13th Annual International Conference on Mobile Computing and Networking (Mobicom 2007)*.

Manea, M., Manea, V., Ferrari, L., Kostoglodov, V., and Bandy, W. (2005). Tectonic evolution of the Tehuantepec Ridge. *EPSL*, 238:64–77.

Manea, V., Manea, M., and Ferrari, L. (2013). A geodynamical perspective on the subduction of Cocos and Rivera plates beneath Mexico and Central America. *Tectonophysics*, 609:56–81.

Manea, V., Manea, M., Kostoglodov, V., and Sewell, G. (2006). Intraslab seismicity and thermal stress in the subducted Cocos plate beneath central Mexico. *Tectonophysics*, 420:389–409.

Mann, P. (2007). Global catalogue, classification and tectonic origins of restraining- and releasing bends on active and ancient strike-slip fault systems. *Geol. Soc. London, Sp. Publ.*, 290.

Masters, G., Barmine, M., and Kientz, M. (2014). Mineos, computational structure for geodynamics. *www.geodynamics.org*.

Matsu'ura, M. and Hirata, N. (1982). Generalized least-squares solutions to quasi-linear inverse problems with a priori information. *J. Phys. Earth*, 30:451–468.

Maus, S., Macmillan, S., McLean, S., Hamilton, B., Thomson, A., Nair, M., and Rollins, C. (2010). The us/uk world magnetic model for 2010-2015. *NOAA Technical Report NESDIS/NGDC*.

Montagner, J.-P., Griot-Pommera, D.-A., and Lav, J. (2000). How to relate body wave and surface wave anisotropy? *J. Geophys. Res.: Solid Earth*, 105(B8):19015–19027.

Montagner, J.-P. and Nataf, H.-C. (1986). A simple method for inverting the azimuthal anisotropy of surface waves. *J. Geophys. Res.*, 91:511 520.

Montagner, J.-P. and Roult, G. (2008). Normal modes of the earth. *Journal of Physics. Proceedings of the Second HELAS International Conference.*, 118:118.

Mori, L., Gomez Yuena, A., Cai, Y., and Goldstein, S. (2007). Effects of prolonged flat subduction on the Miocene magmatic record of the central Trans-Mexican volcanic belt. *Chemical geology*, 244(3-4):452–473.

Orozco, E., Petrone, C. M., Ferrari, L., Tagami, T., and Manetti, P. (2007). Geochemical and isotopic variability in lavas from the eastern Trans-Mexican volcanic belt; slab detachment in a subduction zone with varying dip. *Lithos*, 93(1-2):149–174.

Osete, M. L., Ruiz-Martinez, V. C., Caballero, C., Galindo, C., Urrutia-Fucugauchi, J., and Tarling, D. H. (2000). Southward migration of continental volcanic activity in the Sierra de Las Cruces, Mexico: palaeomagnetic and radiometric evidence. *Tectonophysics*, 318:201–215.

Pardo, M. and Suarez, G. (1995). Shape of the subducted Rivera and Cocos plates in southern Mexico: seismic and tectonic implications. *J. Geophys.Res.*, 100:12.

Perez-Campos, X., Kim, Y., Husker, A., Davis, P. M., Clayton, R. W., Iglesias, A., Pacheco, J. F., Singh, S. K., Manea, V. C., and Gurnis, M. (2008). Horizontal subduction and and truncation of the Cocos Plate beneath Central Mexico. *Geophys. Res. Lett.*, 35:L18303.

Sato, Y. (1955). Analysis of dispersed surface waves by mean of Fourier transform: Part i. *Bull. Earthquake Res. Tokyo Univ.*, 33:33–47.

Silver, P. and Chan, W. W. (1991). Shear wave splitting and sub-continental mantle deformation. *J. Geophys. Res.*, 96:1642916454.

Silver, P. G. (1996). Seismic anisotropy beneath the continents: probing the depths of geology. *Annu. Rev. Earth Planet. Sci.*, 24:385–432.

Smith, M. L. and Dahlen, F. A. (1973). The azimuthal dependence of Love and Rayleigh wave propagation in a slightly anisotropic medium. *J. Geophys. Res.*, 78.

Stubailo, I., Beghein, C., and Davis, P. M. (2012). Structure and anisotropy of the Mexico subduction zone based on Rayleigh-wave analysis and implications for the geometry of the Trans-Mexican Volcanic Belt. *J. Geophys. Res.*, 117:B05303.

Tanimoto, T. and Prindle, K. (2007). Surface wave analysis with beamforming. *Earth, Planets and Space*.

Tong, C., Gudmundsson, O., and Kennett, B. L. N. (1994). Shear wave splitting in refracted waves ceturned froin the upper mantle transition zone beneath northern australia. *J. Geophys. Res.*, 99:15783–15797.

Trampert, J. and Woodhouse, J. (2003). Global anisotropic phase velocity maps for fundamental mode surface waves between 40 and 150 s. *Geoph. J. Int.*, 154:154–165.

Truchan, M. and Larson, R. (1973). Tectonic lineaments on the cocos plate. *EPSL*, 17:46–432.

van Benthem, S. A. C., Valenzuela, R. W., Obrebski, M., and Castro, R. R. (2008). Measurements of upper mantle shear wave anisotropy from stations around the southern Gulf of California. *Geofsica Internacional*, 47(2):127–144.

Vinnik, L. P., Makeyeva, L. I., Milev, A., and Usenko, A. Y. (1992). Global patterns of azimuthal anisotropy and deformations in the continental mantle. *Geophys. J. Int.*,

111.

Warren, L., Snoke, J., and James, D. (2008). S-wave velocity structure beneath the High Lava Plains, Oregon, from Rayleigh-wave dispersion inversion. *Earth Planet. Sci. Lett.*, 274:121–131.

Werner-Allen, G., Lorincz, K., Johnson, J., Lees, J., and Welsh, M. (2006). Fidelity and yield in a volcano monitoring sensor network. *OSDI '06 Proceedings of the 7th symposium on Operating systems design and implementation*, pages 381–396.

Wilson, D. (1996). Fastest known spreading on the Miocene Cocos-Pacific plate boundary. *Geophysical Research Letters*, 23:3003–3006.

Wolfe, C. and Silver, P. (1998). Seismic anisotropy of oceanic upper mantle: Shear wave splitting methodologies and observations. *J. Geophys. Res.*, 103(B1):749–771.

Wustefeld, A., Bokelmann, G., Zarolib, C., and Barruol, G. (2008). Splitlab: A shear-wave splitting environment in matlab. *Computers Geosciences*, 34:515–528.

Yang, T., Grand, S., Wilson, D., Guzman-Speziale, M., Gomez-Gonzalez, J., T., D.-R., and Ni, J. (2009). Seismic structure beneath the rivera subduction zone from finite-frequency seismic tomography. *J. Geophys. Res.*, 114:B01302.

Yang, Z., Sheehan, A., and Shearer, P. (2011). Stress-induced upper crustal anisotropy in southern California. *J. Geophys. Res.*, 116:B02302.

Yuan, K. and Beghein, C. (2013). Seismic anisotropy changes across upper mantle phase transitions. *Earth and Planet. Sci. Lett.*, 374:132–144.

Zandt, G. and Humphreys, E. (2008). Toroidal mantle flow through the Western U.S. slab window. *Geology*, 36(4):295–298.